2014

EVALUATION OF THE EVOLVING STRESS FIELD OF THE YELLOWSTONE VOLCANIC PLATEAU FROM 1988 TO 2010 FROM EARTHQUAKE FIRST MOTIONS INVERSION

Elena Russo
Michigan Technological University

EVALUATION OF THE EVOLVING STRESS FIELD OF THE YELLOWSTONE VOLCANIC PLATEAU FROM 1988 TO 2010 FROM EARTHQUAKE FIRST MOTIONS INVERSION

By

Elena Russo

A THESIS

Submitted in partial fulfillment of the requirements for the degree of

MASTER OF SCIENCE

In Geology

MICHIGAN TECHNOLOGICAL UNIVERSITY

2014

This thesis has been approved in partial fulfillment of the requirements for the Degree of MASTER OF SCIENCE in Geology.

Department of Geological/Mining Engineering and Sciences

Thesis Co-Advisor: *Gregory P. Waite*

Thesis Co-Advisor: *Alessandro Tibaldi*

Committee Member: *Thomas Oommen*

Department Chair: *John Gierke*

INDEX

ABSTRACT

Within the Yellowstone National Park, Wyoming, the silicic Yellowstone volcanic field is one of the most active volcanic systems all over the world. Although the last rhyolite eruption occurred around 70,000 years ago, Yellowstone is still believed to be volcanically active, due to high hydrothermal and seismic activity. The earthquake data used in this study cover the period of time between 1988 and 2010. Earthquake relocations and a set of 369 well-constrained, double-couple, focal mechanism solutions were computed. Events were grouped according to location and time to investigate trends in faulting. The majority of the events has oblique, normal-faulting solutions.

The overall direction of extension throughout the 0.64 Ma Yellowstone caldera looks nearly ENE, consistently with the direction of alignments of volcanic vents within the caldera, but detailed study revealed spatial and temporal variations. Stress-field solutions for different areas and time periods were calculated from earthquake focal mechanism inversion. A well-resolved rotation of σ_3 was found, from NNE-SSW near the Hebgen

Lake fault zone, to ENE-WSW near Norris Junction. In particular, the σ_3 direction changed throughout the years in the Norris Junction area, from being ENE-WSW, as calculated in the study by Waite and Smith (2004), to NNE-SSW, while the other σ_3 directions are mostly unchanged over time.

The Yellowstone caldera was subject to periods of net uplift and subsidence over the past century, explained in previous studies as caused by expanding or contracting sills, at different depths. Based on the models used to explain these deformation periods, we investigated the relationship between variability in aseismic deformation and seismic activity and faulting styles. Focal mechanisms and P and T axes were divided into temporal and depth intervals, in order to identify spatial or temporal trends in deformation.

The presence of “chocolate tablet” structures, with composite dilational faults, was identified in many stages of the deformation history both in the Norris Geyser Basin area and inside the caldera. Strike-slip component movement was found in a depth interval below a contracting sill, indicating the movement of magma towards the caldera.

CHAPTER 1

INTRODUCTION

While most part of volcanism on the Earth is associated with plate boundaries along subduction zones and mid ocean ridges, some volcanoes are located within continental and oceanic plates. Long-lived, deep-seated mantle plumes are thought to provide the source of heat for the long-term volcanic activity at intraplate hotspots. This is the case for Yellowstone, which is located 1600 km east of the western North American plate boundary.

Within the Yellowstone National Park, Wyoming, the silicic Yellowstone volcanic field is one of the most active volcanic systems all over the world. It is located in a tectonically active zone of extension at the eastern edge of the Basin and Range Province.

The Yellowstone Plateau volcanic field is a clear example of a compositionally bimodal rhyolite-basalt igneous field: the rhyolites comprise many lava flows and three major sheets of welded ash-flow tuff

separated by unconformities (Christiansen, 2001). The geologic history of the field defines cycles, all of which show a similar sequence of volcanic events: the climax has always been an eruption of a voluminous sheet of rhyolitic ash-flow tuff and the formation of a large caldera while, before and after the eruption, basalts were erupted around the margins of major rhyolitic volcanism (Christiansen, 2001).

During the past two million years there had been three caldera-forming eruptions, at 2.0, 1.3 and 0.64 Ma; the most recent eruption caused the formation of a 45 km by 70 km collapse caldera that subsided up to 500 m along normal faults on the caldera rim. Since then, the caldera has been covered by at least 30 rhyolitic and basaltic flows (Christiansen, 2001). This late Cenozoic volcanism of Yellowstone is known to have been of latest Pliocene and Pleistocene age, even though it was believed to have occurred in late Tertiary time.

Although the last rhyolite eruption occurred around 70,000 years ago, Yellowstone is still believed to be volcanically active, due to a high hydrothermal and seismic activity and to episodes of deformation inside the caldera. Many studies have shown that the caldera was subject to a

period of net uplift of up to 1 m, at 15 mm/yr, from 1923 through 1984, followed by a 20 mm/yr subsidence that exceeded 190 mm through 1995, and a 5-year return to a minor uplift starting from early 1996 (Pelton and Smith, 1979; Dzurisin et al., 1994; Wicks et al., 1998). This period of uplifting was followed by renewed subsidence (0.9 cm/yr) until 2004, when the caldera started to experience an accelerated uplift, at the incredible rate of 7 cm/yr (Chang et al., 2007). These data refer in particular to the area inside the caldera near the Sour Creek resurgent dome.

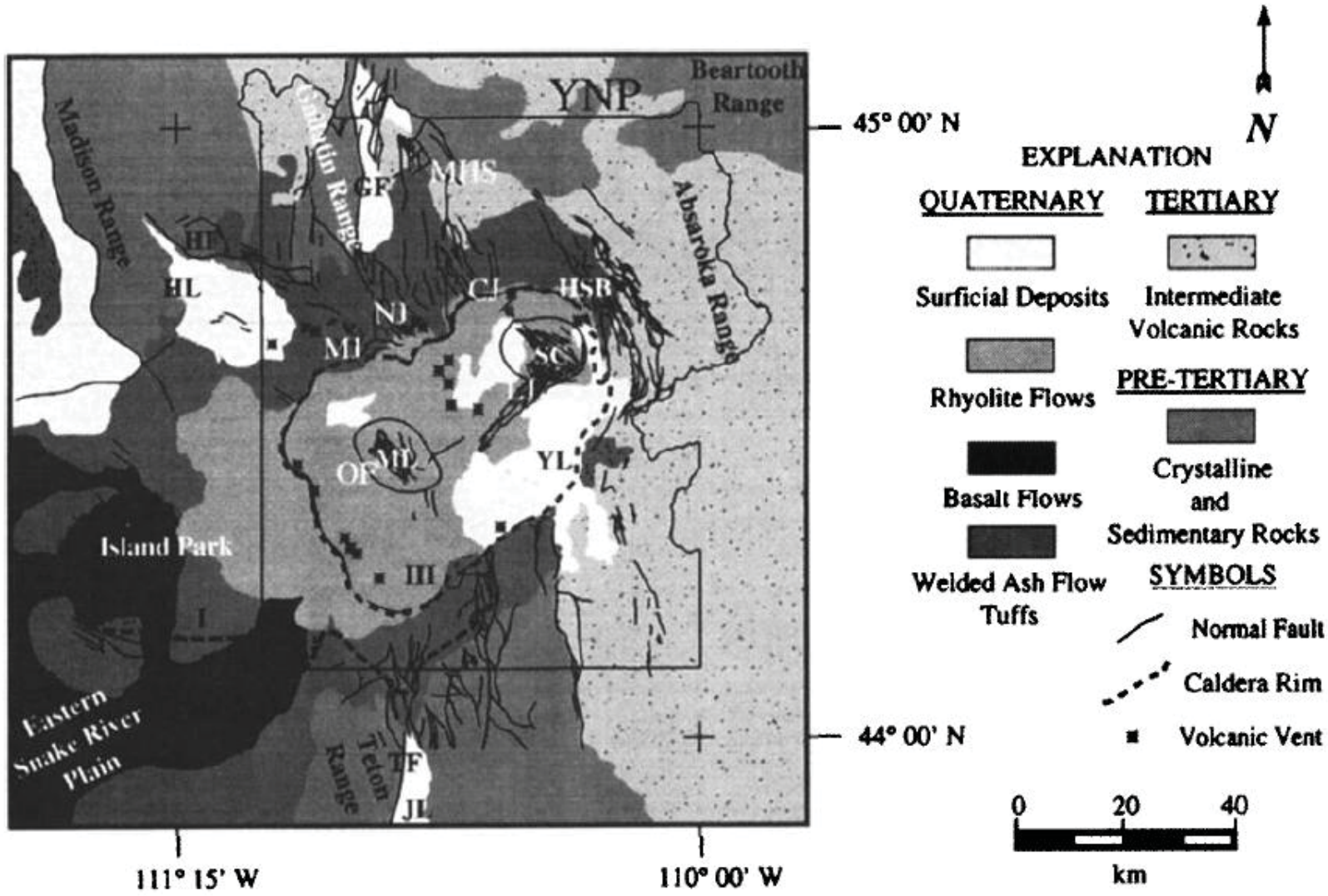
YNP
Beartooth Range
Madison Range
Gallatin Range
Absaroka Range
Island Park
Eastern Snake River Plain
Teton Range
HF
HL
GF
MHS
CL
HSB
NJ
MJ
SC
OP
MT
YL
III
I
TF
JL
45° 00' N
44° 00' N
111° 15' W
110° 00' W
N
EXPLANATION
QUATERNARY
TERTIARY
Surficial Deposits
Intermediate Volcanic Rocks
Rhyolite Flows
PRE-TERTIARY
Basalt Flows
Crystalline and Sedimentary Rocks
Welded Ash Flow Tuffs
SYMBOLS
Normal Fault
Caldera Rim
Volcanic Vent
0
20
40
km

Figure 1.1: General geologic map of the Yellowstone volcanic field and surrounding region. Major surface rock types, caldera boundaries, Quaternary normal faults, Pleistocene volcanic vents, resurgent domes and major lakes are shown. Number and letter symbols denote: I, Huckleberry Ridge caldera (2.0 Ma); II, Henry's Fork caldera (1.3 Ma), III, Yellowstone caldera (0.64 Ma); ML, Mallard Lake resurgent dome; SC, Sour Creek resurgent dome; HSB, Hot Springs Basin; HF, Hebgen Lake Fault; GF, Gallatin Fault; TF, Teton Fault; JL, Jackson Lake; HL, Hebgen Lake; YL, Yellowstone Lake; CJ, Canyon Junction; LJ, Lake Junction; MJ, Madison Junction; MHS, Mammoth Hot Springs; NJ, Norris Junction; OF, Old Faithful and YNP, Yellowstone National Park boundary (Christiansen, 2001).

Seismic activity in the Yellowstone area varies somewhat according to the changes in the deformation pattern. For instance, the change from uplift to subsidence in 1984-1985 coincided with one of Yellowstone's largest swarms (Waite and Smith, 2002). Waite and Smith, in 2002, showed that seismicity of the 1985 earthquake swarm could have been related to hydrothermal or magmatic fluids originating beneath the Mallard Lake resurgent dome and moving towards the northwest. The volume loss after those fluids moved beneath the caldera may have caused the change in movement from uplift to subsidence. In January 2010 the Yellowstone caldera experienced another large earthquake swarm at its northwestern boundary close to the location of the 1985 swarm. In the following five months the caldera started the first overall subsidence since the beginning of its uplift in 2004.

Yellowstone is best known as an area of abundant and spectacular hydrothermal activity: no other area of the world is comparable in the variety and intensity of such activity. It consists of tens of thousands of geysers, fumaroles and hot springs. Although most of it occurs within the ring-fracture zones, this activity extends locally across the caldera rim into

adjacent faulted areas (Christiansen, 2001). The most active hydrothermal systems are those within and immediately adjacent to the caldera ring-fracture zones. These features are the result of the meteoric water circulation along fractures in the upper crust, which is heated from below by crystallizing magma. The hydrothermal activity in the area is driven by the convective and conductive heat flux, which is even more than 30 times higher than the average heat flux of the North American continent (Fournier, 1989). This high heat flux, estimated to be around 1800 mW/m^2, is interpreted to be caused by the crystallization of partial melt of basaltic or rhyolitic magma in a midcrustal magma body that underlies the caldera (Fournier, 1989; Miller and Smith, 1999; Husen et al., 2004; Farrell et al., 2014).

Yellowstone has also been the most seismically active region of the 1300-km-long Intermountain Seismic Belt. One of the largest recorded events to occurr within the 3000 km^2 caldera is the M_L 6.1 (M_S 5.9) 1975 Norris Junction earthquake (Pitt et al., 1979). The largest historic earthquake of the area was the M_S 7.5 Hebgen Lake, Montana earthquake that occurred in 1959 with an epicenter 25 km northwest of the Yellowstone caldera

(Doser, 1985). A significant proportion of Yellowstone seismic activity is concentrated in the east-west trending zone north of the caldera. Numerous other earthquakes, including many within the Yellowstone caldera, are scattered widely in the area of Yellowstone National Park. The caldera itself is characterized by frequent but smaller earthquakes, often occurring in swarms. Seismicity is relatively sparse in the area immediately south of the Yellowstone caldera to Jackson Hole (Smith and Arabasz, 1991).

The earthquake data used in this study are from University of Utah Seismograph Stations (UUSS). The earthquake relocations were computed by using the NonLinLoc package, created by Anthony Lomax. A set of 331 well-constrained, double-couple, focal mechanism solutions was computed, first by using HASH (v 1.2, Hardebeck and Shearer, 2008), then with MOTSI (Abers and Gephart, 2001). The Abers and Gephart (2001) method was then used to calculate stress-field solutions for different areas and time periods from earthquake focal mechanism inversion. The focal mechanism inversion has shown variations both through space and time: the object of this study is to evaluate the evolving stress field of the Yellowstone volcanic

plateau in order to find a mechanism which may have triggered this pattern of variation.

CHAPTER 2

GEOLOGICAL AND GEOPHYSICAL CHARACTERISTICS OF THE YELLOWSTONE VOLCANIC PLATEAU

2.1 Geologic setting

The Yellowstone Plateau, with an average elevation of about 2,400 m, is surrounded to the north, east and south by the middle and southern Rocky Mountains, which were built during the latest Cretaceous and early Tertiary with the Laramide orogeny, a period of great thrusting and folding which created expansive valleys and ranges (Christiansen, 2001). The Laramide orogenic episode was a direct precursor of the predominantly andesitic Absaroka volcanism of Eocene age in Yellowstone region, but neither the Laramide tectonism nor the Absaroka volcanism seems to have had a primary functional relation to the Yellowstone Plateau volcanism. To the southwest, the Yellowstone Plateau stands above Island Park and the Snake River Plain, a northeast trending structural depression about 300 km long with elevations of about 1600-1900 m. The Snake River Plain volcanic field extends 800 km to the west-southwest across part of Idaho, Oregon and

Nevada and it consists of deeply buried rhyolite and surface basalt flows erupted while the North American Plate moved over the hotspot that now is located below Yellowstone (Smith and Braile, 1994). Silicic volcanic centers decrease in age from 16 Ma at the southwestern end of the Snake River Plain to 0.63 Ma in Yellowstone (Armstrong et al., 1975; Christiansen and Blank, 1972; Pierce and Morgan 1992).

Before the plateau volcanism occurred, the Yellowstone region looked like an elevated mountainous terrain formed by differential uplift and tilting of blocks surrounded by normal faults (Christiansen, 2001). Aligned subsequent rhyolitic vents and minor younger faults suggest an old connection between the Teton and Madison Ranges even if the two blocks have opposite major tilts. Even the Red Mountains were probably structurally continuous with the Gallatin Range before the formation of the rhyolite plateau. In 1972, Ruppel proposed that the Gallatin and Teton Ranges were joined beneath the plateau (Ruppel, 1972). These reconstructions suggest a pattern of subparallel but locally branching or intersecting fault-bounded blocks as is typical in the Basin and Range region in the western United States.

The stratigraphy of the Yellowstone Plateau volcanic field was first described by Christiansen (1982). The oldest recognized products of the plateau volcanism are between 2.2 and 2.1 Ma. Those rocks, exposed in the northeastern part of Yellowstone National Park, are called Junction Butte Basalt, and the rhyolitic lava flow of Snake River Butte, in southern Island Park at the margin of what was going to become the first-cycle caldera. Erupting at 2.1 Ma, the first ash-flow sheet of the Yellowstone Group was the Huckleberry Ridge Tuff, which buried an area of 15,500 km^2 in a short time, so that no erosion and no appreciable cooling of the deposit occurred before the end of the eruption. The volume of magma erupted was huge, about 2,500 km^3. This resulted in the collapse of the magma chamber roof to form the first-cycle caldera, between 75 and 95 km long. This caldera extended from Big Bend Ridge, west of Island Park, to the Central Plateau. Postcollapse rhyolitic lava flows erupted at this point.

The second volcanic cycle at 1.3 Ma consists of rocks exposed within a few kilometers of Yellowstone National Park west boundary. During or just after the eruption of more than 280 km^3 of the Mesa Falls Tuff from the Island Park area, the source area collapsed and formed the second-cycle caldera

with a diameter of about 16 km. The west and the north rim of this second caldera are nested against the north-west rim of the first-cycle caldera. This is the reason why the Mesa Falls Tuff is distributed north of Island Park and disappears beneath basalts of the Snake River Plain to the west, but most Mesa Falls ash flows that swept southward and eastward were confined within the older, larger caldera and subsequently were buried. Postcaldera rhyolitic domes are exposed within and near the second-cycle caldera (Christiansen, 2001).

Tectonism, erosion and burial have attenuated the geologic record of the first two volcanic cycles, while the third cycle is much better-preserved. By the time this cycle happened, two major calderas and their related ash-flow plateaus had formed, and the calderas had been partly filled by rhyolitic lavas. The third volcanic cycle started about 1.2 Ma when rhyolitic lavas were erupted from a growing fissure system over a period of about 60,000 years around what was going to become the ring-fracture zone of the Yellowstone Caldera. The highest activity of this cycle came with eruption of the voluminous Lava Creek Tuff 640,000 years ago.

2.2 The Yellowstone caldera

The third-cycle eruption, amassing more than 1000 km^3, formed an ash-flow plateau, called Lava Creek Tuff, that buried more than 7500 km^2 within few hours or days. At the end of this eruption, the Yellowstone caldera formed by collapse of the magma-chamber roof, producing an elliptical basin 85 km long and 45 km wide. Even though the Yellowstone caldera is a single topographic basin, it is made of two structural features as it is shown by the two resurgent domes bounded by steeply inclined ring-fracture zones, formed by a postcollapse uplift within the caldera. The Mallard Lake dome and the Sour Creek dome lie near the centers of two approximately circular segments of the caldera: the compound caldera has a definite elliptical shape. The Sour Creek dome, the eastern structure, became resurgent soon after collapse, as is typical of resurgent calderas. Even if by structural analogy it was originally presumed that also the uplift of the Mallard Lake dome happened early, the age and history of this dome was reexamined and it was shown that the Mallard Lake dome must be about 160,000 years old. The faults within both the resurgent domes form a

complex graben along the northwest-trending structural axis (Christiansen, 2001).

The youngest known rhyolite flows on the Yellowstone Plateau are about 70,000 years old: no magmatic eruptions are known to have occurred within or near the Yellowstone caldera after that time.

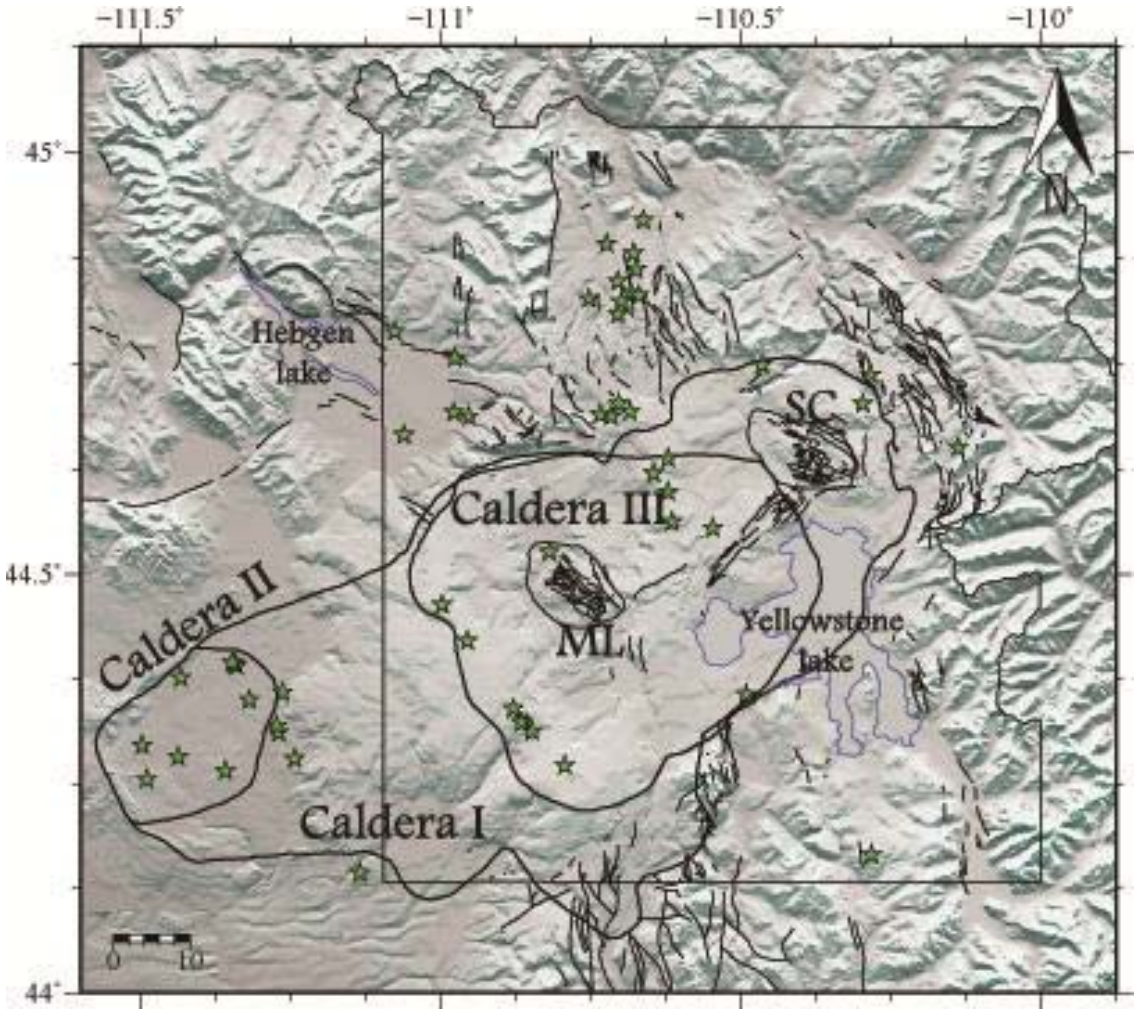

Figure 2.1: A topographic map of the Yellowstone volcanic field, showing the three calderas and Cenozoic faults as mapped by Christiansen (1984). Caldera I: 2.0 Ma. Caldera II: 1.3 Ma. Caldera III: 0.63 Ma. The northern boundary of the region is characterized by a topographic contrast that may have been the result of the 2.0 Ma eruption. ML and SC, outlined with a dashed line, represent the Mallard Lake resurgent dome and the Sour Creek resurgent dome. Volcanic vents are highlighted by green stars and Yellowstone and Hebgen lakes are outlined with a blue line. The topographic data is provided by the USGS National Elevation Dataset.

The magmatic history of the Yellowstone Plateau volcanic field must be interpreted in relation to the late Cenozoic volcanism and tectonics of the Snake River Plain and to the contemporaneous tectonics of part of the Northern and Middle Rocky Mountains and the northern part of the Basin and Range province. The Yellowstone Plateau volcanic field and the eastern Snake River Plain are flanked by linear mountain ranges separated by parallel valleys. The ranges and valleys generally trend northward in the southern and eastern parts of the region, but farther north and west they are toward the northwest. These parallel linear topographic features are fault blocks, most of them tilted. The bounding faults are normal and they are characterized by mainly dip-slip displacements, even if some of them present a minor strike-slip component. Although the initial time of extensional faulting was during the middle Miocene in the Northern and Middle Rocky Mountains region, such movement clearly has continued in the Yellowstone region without break to the present. Faulting inside and around the Yellowstone Plateau has continued since the formation of the

Yellowstone caldera 640,000 years ago and its filling, up to 70,000 years ago, by rhyolitic lavas.

2.3 Previous work on the Yellowstone volcanic plateau

Recordings made with the permanent seismic network at Yellowstone have been used for a large number of studies, including several studies of earthquake focal mechanisms and stresses.

The first detailed study (Peyton, 1991), used data from 1973 to 1989. Interpretation was limited to the area NW of the caldera, because of the sparse seismicity within the caldera. The study revealed NNE-SSW extension in that area. Geodetic studies have confirmed NNE-SSW extension across the Hebgen Lake fault zone interpreted as post-seismic deformation following the 1959 earthquake (Dzurisin et al., 1990; Savage et al., 1993; Puskas et al., 2002). Results from permanent and campaign GPS deployments show a rotation of extension from NNE-SSW in the Hebgen Lake area to ENE-WSW south of the Yellowstone caldera (Puskas et al., 2002).

Waite and Smith (2004) examined for the first time the spatially varying stress field at Yellowstone using the catalog of network-recorded earthquakes. A rotation of extensional stress indicators was observed north of the Yellowstone caldera, where the seismicity was the densest according to the available data. It was impossible to resolve the state of stress within and south of the caldera because those areas were characterized by a shallow seismicity and unreliable focal mechanisms. It has been suggested that Yellowstone volcanism interrupted continuous N-S striking normal faults to the north and south of the Yellowstone caldera and that the alignment of postcaldera volcanic vents within the caldera may represent zones of weakness that link those features. In their study (2004), Waite and Smith showed that the N-S striking faults to the north of the caldera may not be active anymore, according to the minimum principal stress directions. They showed that the N-S extension might be related to a viscoelastic relaxation in the upper mantle and lower crust after the 1959 Hebgen Lake earthquake and to the migration towards northeast of the Yellowstone hotspot. The overall N-S to E-W extension was consistent with

the crustal deformation at Yellowstone dominated by NE-SW Basin and Range extension in this area.

The study by White et al. (2009) focused on seismic activity of the Teton region, which is located south of the Yellowstone caldera. The earthquake catalogues determined from three-dimensional seismic velocity models revealed a seismically quiescent Teton fault with diffuse seismicity in the southern Jackson Hole Valley area and notable seismicity eastward into the Gros Ventre Range. Relocated Yellowstone earthquakes have shown a dominant E-W zone of seismicity that extends from the aftershock area of the 1959 M_S 7.5 Hebgen Lake, Montana, earthquake along the north side of the 0.64 Ma Yellowstone caldera (White et al., 2009). Stress field orientations derived from inversion of focal mechanism data revealed dominant E-W extension across the Teton fault with NE-SW extension along the northern Teton fault area and southern Yellowstone. The minimum stress axes directions then rotate to E-W extension across the Yellowstone caldera to N-S extension northwest of the caldera and along the Hebgen Lake fault zone (White et al., 2009).

2.4 Geophysical characteristics

Density models for the Yellowstone volcanic field incorporates results from a major seismic refraction study by Smith et al. (1982) and Schilly et al. (1982), three-dimensional P-wave tomographic imaging of Yellowstone by Husen et al. (2004) and the tomographic analysis of the Intermountain Seismic Belt by Lynch et al. (1997). The velocity structure of Yellowstone reveals a P-wave low-velocity anomaly (4.0 to 4.8 km/s), at depths of about 3 to 9 km beneath the caldera that is inferred to be a zone of partial melt Schilly et al., 1982. The more detailed and higher resolution tomography of Husen et al. (2004) indicates that the anomaly has a P-wave velocity as low as 4.6 km/s and is shallower near the Mallard Lake and Sour Creek resurgent domes (DeNosaquo et al., 2009).

Gravity modeling assumed a granitic upper crust, a mafic granulite lower crust and predominantly dunite mantle: the low velocity body corresponds to a zone of presumed partial melt with density equal to 2470 kg/m^3. The density model suggests that this partial melt is relatively shallow (10 km)

over the entire length of the caldera and shallower (7 km) about 10 to 20 km beyond the northeastern boundary of the Yellowstone caldera: tomographic images of Husen et al. (2004) are poorly resolved in this area because of a lack of seismic sources there. The density model by DeNosaquo suggests also a variation in density within this body of partial melting material, even though the gravity anomaly may also reflect changing thickness or deeper thermal variations. The density is at its minimum, which is 2470 kg/m^3 just beyond the northeastern border of the caldera, where it is also the shallowest. Beneath the rest of the caldera the partial melt has a density of 2520 kg/m^3.

Yellowstone caldera is characterized by a very weak crust, due to a high geothermal gradient: the strength models by DeNosaquo predict the brittle-ductile transition in the Yellowstone caldera to occur at about 4 km and a ductile behavior of the lower crust and mantle.

CHAPTER 3

SEISMIC NETWORK

In this study, I used the data between 1988 through the beginning of 2010, comprising 31,522 events, to determine earthquake focal mechanisms and regional stress-field solutions. The University of Utah Seismograph Stations (UUSS) operates the Yellowstone seismic network, that has consisted of up to 47 short-period, vertical and three-component seismic stations, to record and document earthquakes, locate epicenters and provide public information and data for scientific research. The Yellowstone earthquake catalog is based mainly on data from a telemetered seismic network in the Yellowstone region. The U.S. Geological Survey operated this network from 1972 through 1981 and from 1984 until 1991 (Pitt, 1987). The USGS ceased operation of the network in November 1981 and no data were recorded for 1982 or 1983. Until 1981, the data from this network were recorded at Yellowstone Park Headquarters at Mammoth, Wyoming, and at the USGS office in Menlo Park, California. The number of stations in the Yellowstone

seismic network varied from 1972 through 1981, varying from 12 to 26 stations in October 1974 (Husen and Smith, 2004). From 1984 through 1991, the network consisted of 16 vertical-component stations; three-component stations were added in 1993 and broadband digital telemetry stations in 1995. On September 2006, the network consisted of 26 stations: six broadband 3-component digital telemetry stations, three 3-component short-period stations and 17 vertical-component short-period stations. Furthermore, another upgrade to the network was introduced in the time period between 2009 and 2011 from the ARRA (American Recovery and Reinvestments Act) by USGS and NPS funding that included installation of two vertical short-period, seven three-component short period, 11 broadband seismometers and seven accelerometers. I used the seismic analyst's manually picked P-wave and S-wave arrival and the earthquake waveforms produced by the UUSS. I reviewed all the waveforms to check whether it was necessary to correct the first motions already picked by the analyst, to make the data more accurate.

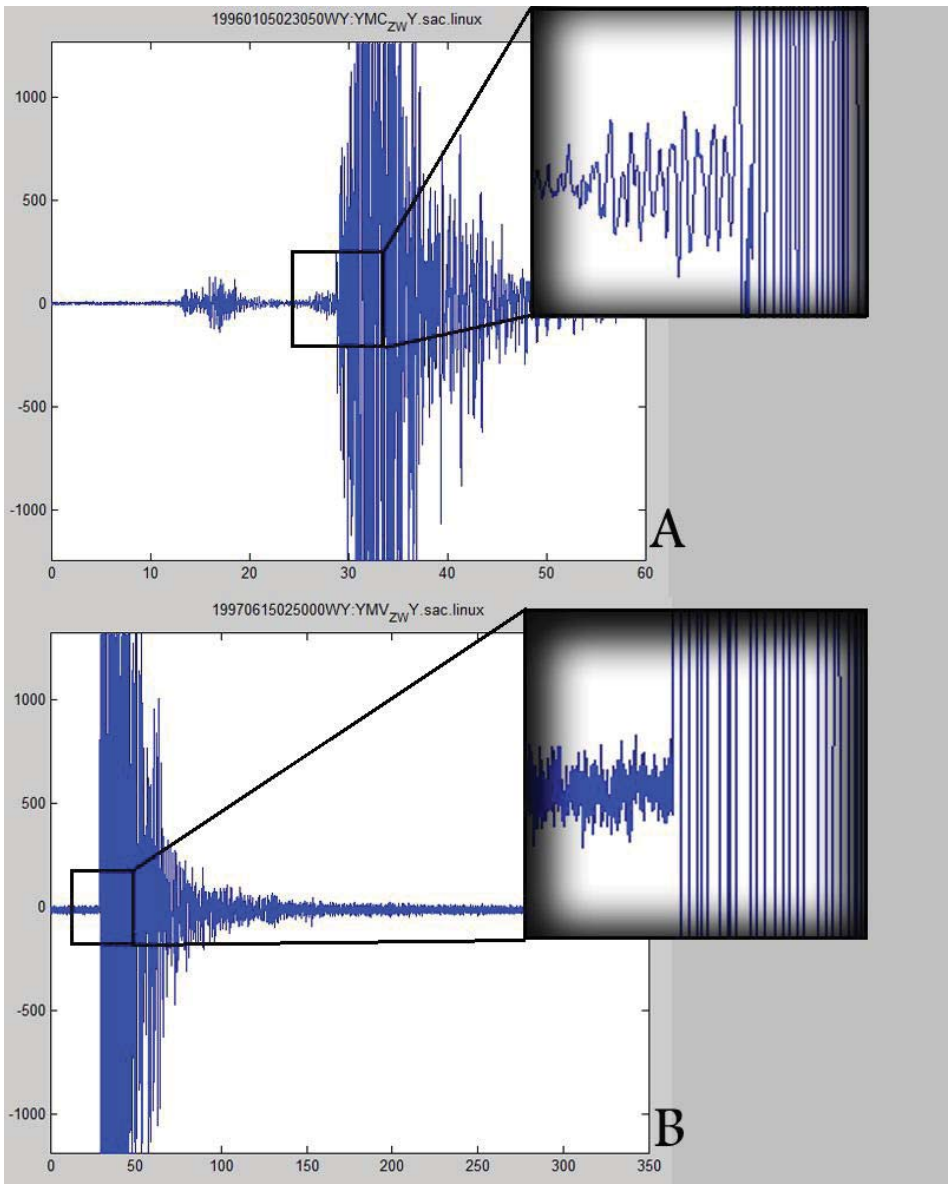

Figure 3.1: Example of reviewed and corrected P-wave polarities. (a) 1996/01/05, station YMC, the analyst was not able to value the first arrival and he interpreted it as a question mark "?", I changed it into a compressional (C) first- arrival. (b) 1997/06/15, station YMV, this was changed from "?" to "C" as well.

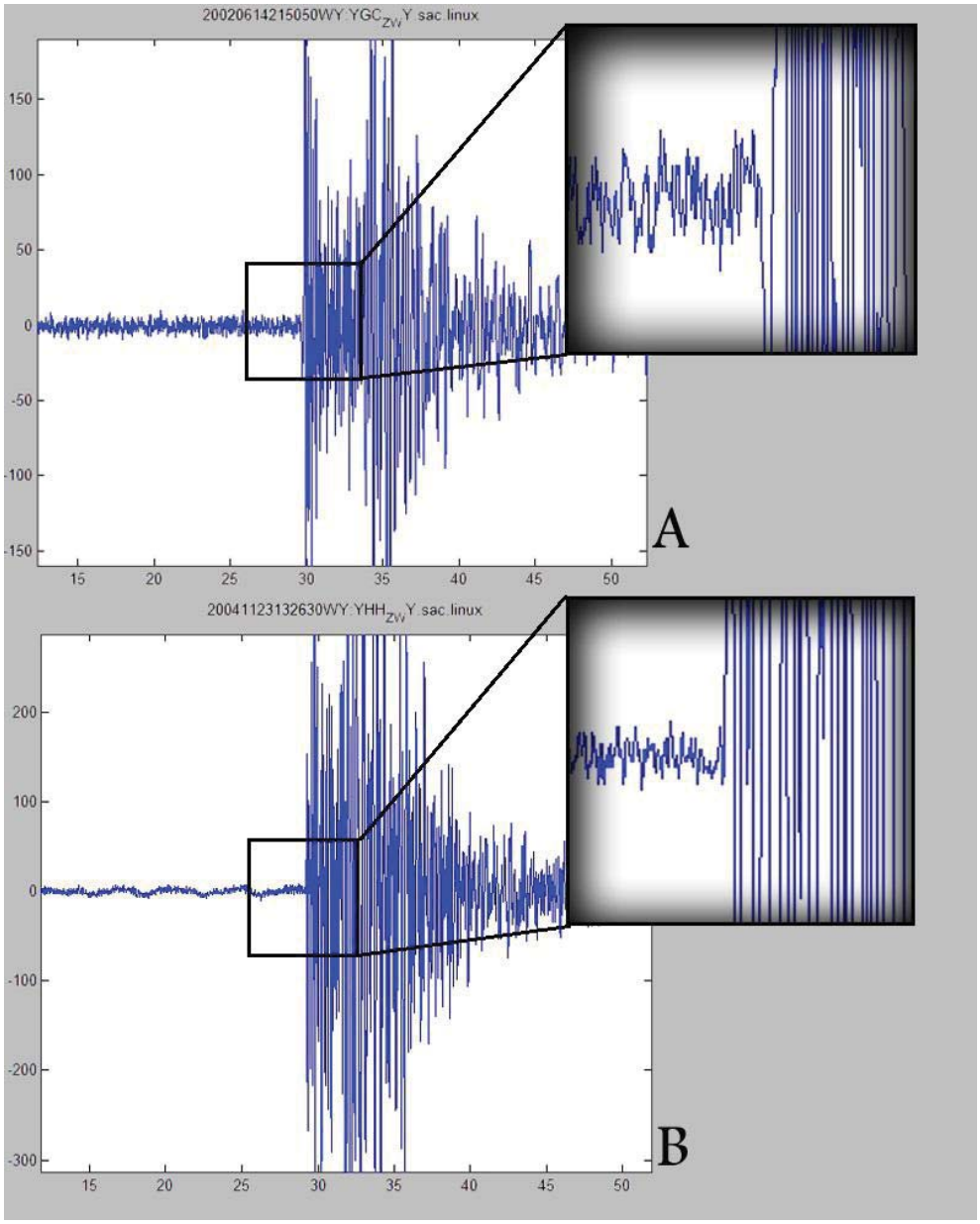

Figure 3.2: Example of reviewed and corrected P-wave polarities. (a) 2002/06/14, station YGC, the analyst was not able to value the first arrival and he interpreted it as a question mark "?", I changed it into a dilatational (D) first- arrival. (b) 2004/11/23, station YHH, this was changed from "?" to "C", compressional.

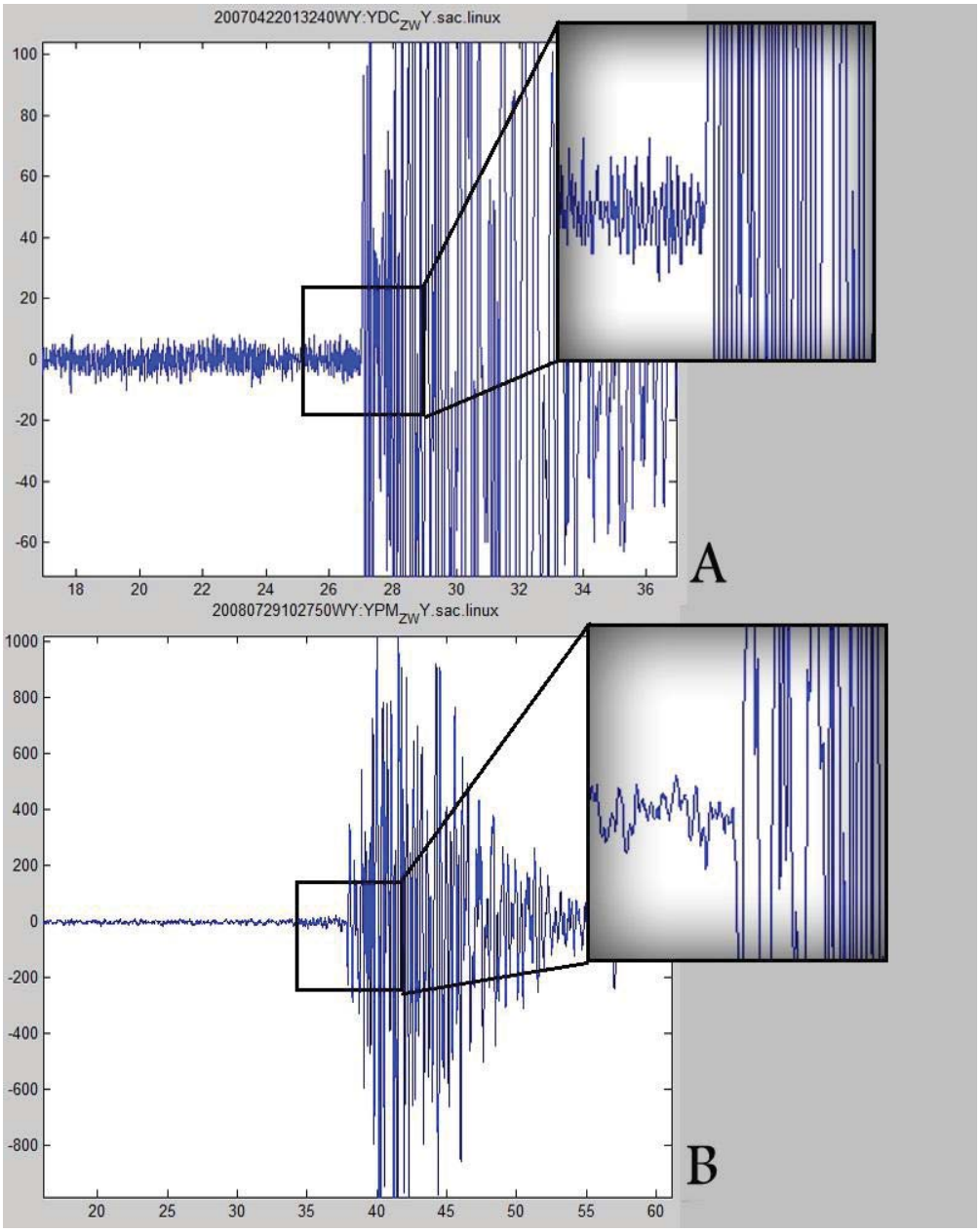

Figure 3.3: Example of reviewed and corrected P-wave polarities. (a) 2007/04/22, station YDC, the analyst interpreted the first arrival as a question mark "?", I changed it into a compressional (C) first arrival. (b) 2008/07/29, station YPM, this was changed from "?" to a dilatational (D) first arrival.

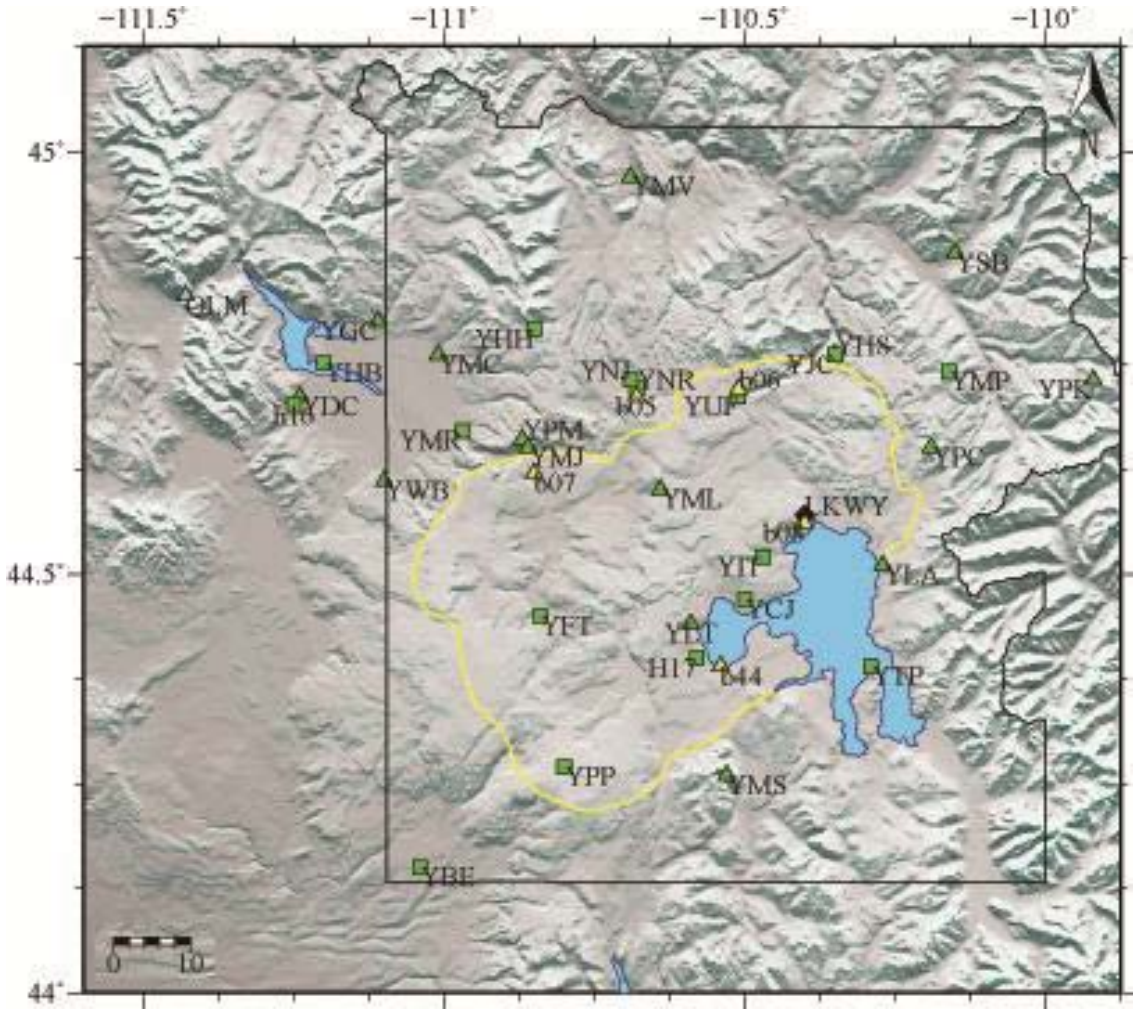

Figure 3.4: Yellowstone seismic network, belonging to the University of Utah Seismic Stations (UUSS), that have been used in this study. The green squares are the UUSS broadband stations, while the green triangles represent the location of the short-period stations. The yellow triangles are stations belonging to the EarthScope Plate Boundary observatory. The black diamond (LKWY) is a station belonging to the U.S. Geological Survey Network. The light blue triangle (QLM) station belongs to the Montana Regional Seismic Network. The 0.64 Ma Yellowstone caldera is outlined in yellow. The topographic data is provided by the USGS National Elevation Dataset.

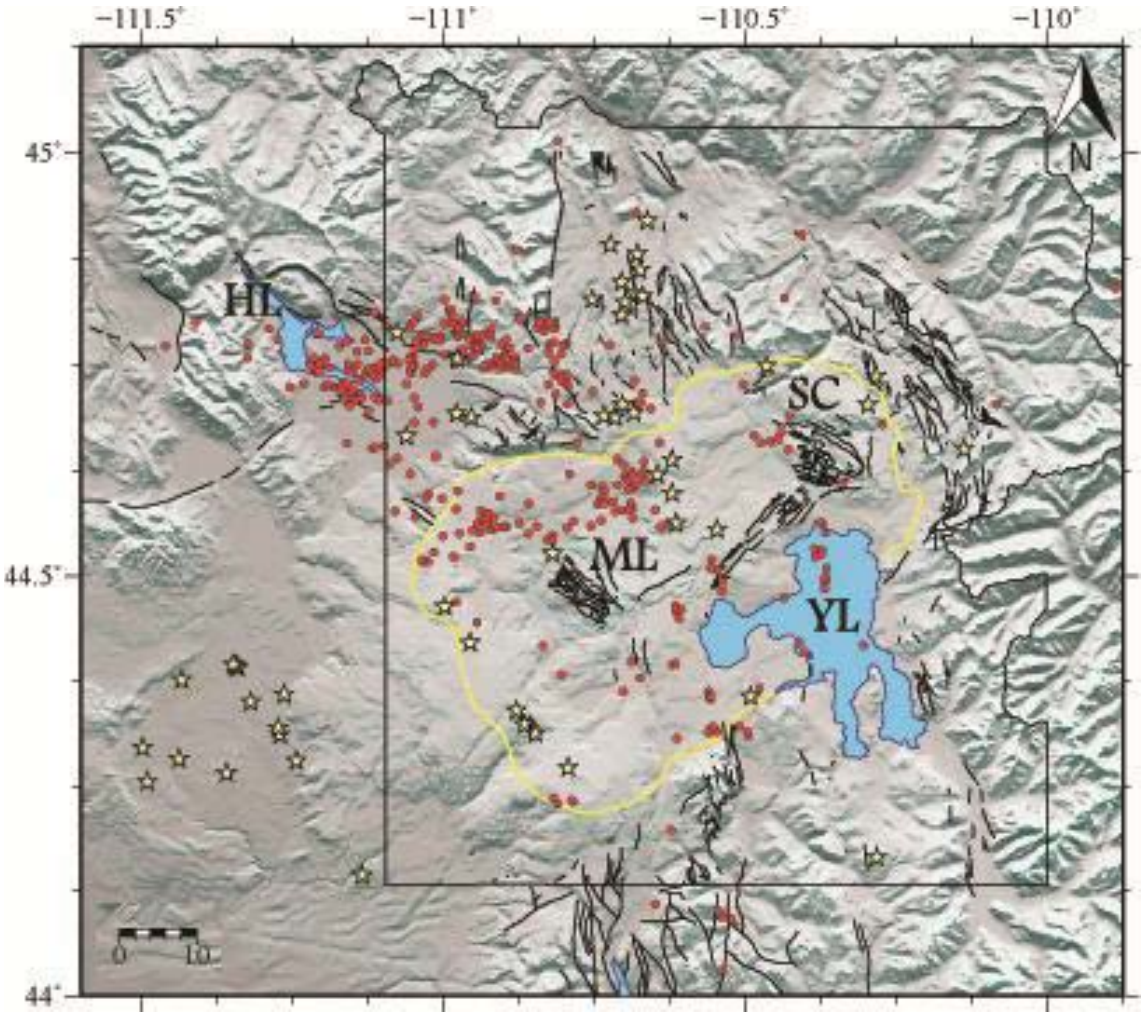

Figure 3.5: Relocated earthquakes in Yellowstone from 1988 to early 2010. Earthquake epicenters are shown as red dots, post-caldera vents are shown as yellow stars and quaternary faults are shown as black lines. The two resurgent domes are outlined with a light blue line. The caldera is outlined in yellow. YL=Yellowstone Lake, HL=Hebgen Lake, ML=Mallard Lake resurgent dome, SC=Sour Creek resurgent dome. The topographic data is provided by the USGS National Elevation Dataset.

3.1 Earthquake relocation

In this study, the software package NonLinLoc (Lomax et al., 2000) was used to relocate the 31,522 events belonging to the Yellowstone earthquake catalog from 1988 to 2010. NonLinLoc follows the probabilistic formulation of nonlinear inverse problems by Tarantola and Valette (1982). The formulation relies on the use of normalized and unnormalized probability density functions to express knowledge about the values of parameters. If the probability density functions giving a priori information on the model parameters and on observations are independent, and the theoretical relationship relating a vector of observed data and unknown parameters can be expressed as a conditional density function, then a complete, probabilistic solution can be expressed as a posteriori probability density function (Tarantola and Valette, 1982).

In earthquake location, the unknown parameters are the hypocentral coordinates and the origin time, T. The observed data are arrival times measured at seismograph stations and the theoretical relation gives predicted or theoretical travel times. In NonLinLoc, the probability density function can be computed in different ways (Lomax et al., 2000): using a

grid-search algorithm with successively finer, nested grids, with a Metropolis-Gibbs sampling algorithm performing a directed random walk within a special volume to obtain a set of samples that follow the probability density function, and with an Oct-Tree Importance sampling algorithm, which gives accurate, efficient and complete mapping of the probability density function of the earthquake location problem (Lomax and Curtis, 2001). It uses recursive subdivision and sampling of cells in three dimensions to generate a cascade of sampled cells, where the number of sampled cells follows the values of the probability density function at the cell center, leading to a higher density of cells in areas of higher probability density function. Multiple minima in the function are reliably detected by the grid-search algorithm and the Oct-Tree algorithm but are missed by a factor of 100 in computing time. This algorithm may not detect narrow, local minima in the density function.

3.2 Best data selection

After the relocation, earthquake data were selected by applying some selection criteria, in order to increase the data accuracy. Many of the earthquakes in Yellowstone are of small magnitude, causing the number of

recording stations to be low. We decided to take into account just the earthquakes with a minimum number of observations equal to 10. Increasing numbers of arrival-time observations generally result in improved earthquake locations. The maximum ratio of distance and depth was imposed to be 1.50:1. Another parameter that proved to be important was the difference between the maximum likelihood and expectation hypocenter locations. Large differences between the maximum likelihood and the expectation hypocenter locations can result from an ill-conditioned location problem Lomax et al, 2000. In this case, Gaussian location estimates, for example the confidence ellipsoid, are not adequate uncertainty estimates anymore because location uncertainties can be irregular or show multiple minima. In this study, the higher difference was imposed to be equal to 500 meters. The azimuthal gap, which is the largest distance between azimuthally adjacent stations, was imposed to be lower than 180 degrees. In general, the smaller this number, the more reliable is the calculated horizontal position of the earthquake.

The average error, which is the average length of the three axes of the 68% ellipsoid, had to be lower than 2000 m. The root-mean-square (RMS) travel

time residual, measured in seconds, provides a measure of the fit of the observed arrival times to the predicted arrival times for this location. Smaller numbers reflect a better fit of the data. This value depends on the accuracy of the velocity model used to compute the earthquake location, the quality weights assigned to the arrival time data and the procedure used to locate the earthquake. In this study, RMS was imposed to be less than 0.5 seconds.

Some earthquakes may show a well defined epicenter location but a poorly-constrained focal depth, because of the lack of a station within the critical focal depth distance. This is critical for shallower earthquakes, especially inside the caldera, where most of the earthquakes are shallow and the station distribution is more sparse because of logistical issues. We observed a remarkable increase of quality of data in the more recent events if they are compared with the earlier events, probably because of improvements to denser station coverage and in network operation in general since 1995.

3.3 Station polarities correction

The data record in the Yellowstone network is managed by FM radios and telephone lines to the University of Utah. These data transfer methods can sometimes cause a reverse in polarity of the waveform data from a particular station or from many stations at the same time, because phone companies may change the signal polarities of the lines used by seismic stations during maintenance periods. P wave arrivals are continuously reviewed to determine whether this has occurred. Because the distance between these earthquakes and the Yellowstone network is large, all the stations in the network are assumed to record waves with the same polarity. If the polarity at one station appears to be the opposite of the polarities of the other stations, that station is considered to have reversed polarity. Founded in 1984, IRIS is a consortium of over 100 US universities dedicated to the operation of science facilities for the acquisition, management and distribution of seismological data. For each station, I checked on the IRIS website the stages of reversed polarity and the results of this search were used to correct the first motion data where it was necessary (table 3.1).

In some cases, the polarity of a particular station could not be determined because of a lack of data and the first arrival data from stations with this problem was denoted by a question mark; those first arrivals were removed from the data set.

	1988	1989	1990	1991	1992	1993	1994	1995	1996	1997	1998	1999	2000	2001	2002	2003	2004	2005	2006	2007	2008	2009
YBE	N	N	N	N	N	N	N	N														
YCJ	?	n	N	N	N	N	N	N	N	N	N	N	N	N	N	N	N	N				
YDC	N	N	N	N	N	N	N	N	N	N	N	N	N	N	N	N	N	N	N	N	N	N
YFT					R	N	N	N	N	N	N	N	N	N	N	N	N	N	N	N	N	N
YGC	N	n	N	N	N	N	N	N	N	N	N	N	N	N	N	N	N	N	N	N	N	N
YHB								N	N	N	N	N	N	N	N	N	N	N	N	N	N	N
YHH						N	N	N	N	N	N	N	N	N	N	N	N	N	N	N	N	N
YHS	N	N	N	N	N	N																
YIT			N	N	N	N	N	N	N	N	N	N	R	N	N	N	N	N	N	N	N	N
YJC						R	N	N	N	N	N											
YLA		N	N	N	N	N	N	N	N	N	N	N	N	N	N	R	N	N	N	N	N	N
YLT												N	N	N	N	N	N	N	N	N	N	N
YMC	N	N	N	N	N	N	N	N	N	N	N	N	N	N	N	N	N	N	N	N	N	N
YMJ	N	N	N	N	N	N																
YML						R	N	N	N	N	N	N	N	N	N	N	N	N	N	N	N	N
YMP															N	R	N	N	N	N	N	N
YMR								N	N	N	N	N	N	N	N	N	N	N	N	N	N	N
YMS								N	N	N	N	N	N	N	N	N	N	N	N	N	N	N
YMV					R	R	N	N	N	N	N	N	N	N	N	N	N	N	N	N	N	N
YNU	/	n	N	n	N	N																
YNR						R	R	N	N	N	N	N	N	N	N	N	N	N	N	N	N	N
YPC	N	N	N	N	N	N	N	N	N	N	R	N	N	N	N	N	N	N	N	N	N	N
YPK																		N	N	N	N	N
YPM						N	N	N	N	N	N	N	N	N	N	N	N	N	N	N	N	N
YPP									N	N	N	N	N	N	N	N	N	N	N	N	N	N
YTC	N	N	N	N	N	N	N															
YSB	n	N	N	N	N	N	N	N	N	N	N	N	N	N	N	N	N	N	N	N	N	N
YTP							N	N	N	R	R	N	N	N	N	N	N	N	N	N	N	N
YUF																		N	N	N	N	N
YWB	N	N	N	N	N	N	N	N	N	N	N	N	N	N	N	N	N	N	N	N	N	N

N=Normal polarity

R= Reversed polarity

? = Contradictory information

n=probably normal

= Station inactive

Table 3.1 UUSS Yellowstone Station Polarities

CHAPTER 4

FOCAL MECHANISMS

The focal mechanism of an earthquake sums up the slip motion of the rocks underground and the orientation of the fault that the slip occurred on. Focal mechanisms are important in particular for determining fault orientation and slip direction for an earthquake magnitude less than 5 or 6, when the ground surface is not ruptured to produce a visible fault scarp.

4.1 Focal mechanism determination

Focal mechanism solutions for the selected events were determined using the FORTRAN program HASH (v 1.2, J. Hardebeck et P. Shearer, 2008), which fits P-wave first motion data to the double-couple focal mechanisms. Generally, for small events, or events in strongly scattering media, the P-wave first motion polarities may be too difficult to determine or sensitive to various sources of errors, including imperfect knowledge of the seismic velocity structure. This method was developed to address this problem and

it has been shown to produce more accurate and stable focal mechanisms than prior methods.

The HASH method uses a grid-search over possible combinations of nodal planes, generates a set of acceptable mechanisms for each event given the sources of uncertainty, and returns the most likely mechanism. Mechanism quality is assigned based on the solution stability with respect to model uncertainty, represented by the spread of the acceptable mechanisms, which take into account the uncertainty in polarity measurements, event location and take-off angle.

The most probable solution is computed together with some estimates of the quality of the solution. The preferred solution is the average of the acceptable fault plane solutions after outliers have been removed. The RMS (Root Mean Square) difference between the acceptable nodal planes and the preferred planes is computed.

The final step is to find the data misfit for the preferred mechanism. The inputs for both the subroutines are the set of polarity (and amplitude ratio) observations for the stations, the azimuth, the takeoff angle to each station

and the preferred mechanism. The outputs are the weighted fraction of misfit polarities and the station distribution ratio. A mechanism quality criterion was developed: the best single-parameter indicator of mechanism quality seems to be the average RMS fault plane uncertainty, with values less than 35 degrees indicating the best mechanisms.

Table 4.1: Focal mechanism quality determination

quality (qual)	average misfit (mfrac)	RMS fault plane uncertainty	station distribution ratio (stdr)	mechanism probability (prob)
A	≤ 0.15	≤ 25°	≥ 0.5	≥ 0.8
B	≤ 0.20	≤ 35°	≥ 0.4	≥ 0.6
C	≤ 0.30	≤ 45°	≥ 0.3	≥ 0.7
D	maximum azimuthal gap ≤ 90°, maximum takeoff angle gap ≤ 60°			
E	maximum azimuthal gap > 90°, maximum takeoff angle gap > 60°			
F	fewer than 8 polarities			

4.2 Double-couple focal mechanism results

We determined 510 focal mechanisms in the study area from 569 events. As seen in table 4.1, the quality of solutions determined by using HASH is defined by four parameters: average misfit, RMS fault plane uncertainty, station distribution ratio, and mechanism probability (Hardebeck and Shearer, 2002). Unfortunately, no solutions were high quality A or B events.

The number of solutions with qualities C and D was 8 and 125, respectively. The all 133 focal mechanism solutions with the best qualities are listed in table 4.2. The quality F events are characterized by less than 8 picked polarities. All 477 solutions with E or F quality were discarded.

The lack of high quality solutions could be due to the fact that the HASH method and the solution quality scheme have been developed for Southern California, where the density of the station network is higher than in the Yellowstone volcanic field.

Table 4.2: Double-couple focal mechanism results

Yr	Mo	d	Hr	Mn	Sec	Lat	Long	Dep	Str	di	rk	E1	E2	NP	Q
94	3	26	20	41	2.59	44.781	-110.941	7.17	342	50	-152	44	47	14	D
94	9	24	15	4	40.45	44.657	-110.473	6.63	7	47	-128	44	46	15	D
94	9	30	8	40	25.95	44.725	-110.826	5.83	79	86	167	46	49	10	D
94	9	30	8	40	25.95	44.725	-110.826	5.83	94	38	-122	47	49	10	D
94	10	26	11	54	44.08	44.727	-111.061	7.08	228	71	156	46	47	10	D
95	11	30	15	7	48.42	44.754	-110.909	6.29	247	84	176	44	47	10	D
95	12	3	1	19	23.86	44.757	-110.901	5.23	292	69	-126	41	44	16	D
95	12	3	1	19	23.86	44.757	-110.901	5.23	104	42	-154	49	52	16	D
96	10	11	17	46	36.58	44.723	-110.793	7.98	277	85	-144	30	37	16	C
96	10	16	11	48	28.92	44.727	-110.794	5.78	273	87	-175	37	44	16	D
96	10	16	11	48	28.92	44.727	-110.794	5.78	314	46	-94	44	44	16	D
96	12	15	17	4	48.34	44.747	-110.922	4.07	10	73	-119	57	56	15	D
97	3	4	7	21	9.52	44.792	-110.919	7.89	76	88	136	42	43	12	D
97	6	15	2	50	24.17	44.729	-110.803	8.42	139	77	172	51	53	13	D
00	7	28	7	46	58.59	44.799	-110.786	4.83	249	72	-175	44	49	11	D
00	7	28	7	46	58.59	44.799	-110.786	4.83	302	40	-84	48	46	11	D
00	7	29	5	16	59.40	44.786	-110.773	13.32	225	71	-156	41	40	13	D
00	7	29	5	16	59.40	44.786	-110.773	13.32	282	50	-71	48	49	13	D
00	8	7	9	7	41.22	44.795	-110.844	5.54	267	90	-169	37	40	21	D
00	8	10	22	31	19.40	44.771	-111.054	9.26	97	70	-172	49	48	13	D
00	10	3	8	7	51.50	44.708	-110.738	9.87	86	81	-179	43	46	19	D
00	10	3	8	7	51.50	44.708	-110.738	9.87	144	41	-65	48	44	19	D
00	11	24	4	20	5.90	44.745	-110.707	6.56	306	45	-100	35	36	21	C
00	12	24	14	37	25.45	44.755	-110.851	6.25	306	79	-143	49	46	11	D
00	12	24	14	37	25.45	44.755	-110.851	6.25	360	53	-69	48	49	11	D
01	3	12	11	36	12.59	44.785	-110.970	6.34	8	36	-100	34	41	17	C
01	3	25	10	22	53.69	44.807	-110.986	4.03	130	38	-52	44	45	11	D
01	5	21	9	47	56.53	44.718	-110.752	15.29	35	72	-114	44	39	20	D
01	5	21	9	47	56.53	44.718	-110.752	15.29	100	28	-137	45	44	20	D
01	5	24	17	27	48.71	44.634	-110.667	4.68	340	44	-98	40	41	20	D
01	5	24	17	27	48.71	44.634	-110.667	4.68	267	57	-85	46	41	20	D
01	12	16	1	34	39.75	44.807	-111.043	3.00	83	89	149	55	56	9	D
02	1	15	18	4	0.28	44.584	-110.744	0.74	10	44	-124	41	39	14	D
02	1	15	18	4	0.28	44.584	-110.744	0.74	347	83	-178	42	42	14	D
02	1	15	18	37	56.75	44.559	-110.756	14.25	172	37	-120	40	41	19	D
02	1	15	18	37	56.75	44.559	-110.756	14.25	272	29	-85	45	45	19	D
02	4	14	6	36	2.50	44.757	-110.956	7.85	297	73	-97	39	38	14	C
02	4	19	13	55	38.36	44.378	-110.674	7.97	279	77	173	42	42	14	D
02	4	19	13	55	38.36	44.378	-110.674	7.97	87	64	127	44	46	14	D
02	8	6	22	36	5.66	44.631	-111.089	17.18	280	59	169	38	38	15	D
02	11	3	23	51	7.29	44.382	-110.804	5.59	215	43	-88	41	41	13	D
02	11	3	23	51	7.29	44.382	-110.804	5.59	104	44	-93	41	43	13	D
02	11	4	9	42	18.82	44.606	-110.710	2.65	229	52	-84	45	49	15	D
02	11	11	10	43	14.32	44.457	-110.614	3.29	72	29	-96	36	41	16	D
03	1	29	20	53	50.29	44.515	-111.032	8.66	115	54	-125	51	50	15	D
03	1	29	20	53	50.29	44.515	-111.032	8.66	255	72	175	48	45	15	D
03	1	31	16	35	25.52	44.527	-111.015	9.34	95	70	-168	44	42	14	D

Yr	Mo	d	Hr	Mn	Sec	Lat	Long	Dep	Str	di	rk	E1	E2	NP	Q
03	1	31	16	35	25.52	44.527	-111.015	9.34	287	51	-129	48	46	14	D
03	11	10	2	25	23.94	44.797	-110.967	3.21	226	80	-166	44	45	11	D
03	11	27	13	31	8.92	44.707	-111.093	10.31	35	82	-116	50	54	9	D
03	12	17	2	31	2.53	44.705	-110.671	9.93	19	47	-91	38	40	18	D
03	12	17	2	31	2.53	44.705	-110.671	9.93	131	46	-100	46	39	18	D
04	1	26	7	11	4.71	44.749	-111.018	4.70	93	37	-117	45	44	17	D
04	3	16	17	18	37.62	44.772	-110.826	4.78	67	90	172	45	48	11	D
04	3	25	14	21	56.06	44.608	-110.339	-0.00	81	36	-74	48	42	10	D
04	3	25	14	21	56.06	44.608	-110.339	-0.00	284	35	-140	48	48	10	D
04	5	14	0	41	19.24	44.778	-111.129	7.72	351	51	-136	40	40	18	D
04	5	14	0	41	19.24	44.778	-111.129	7.72	168	56	-139	45	45	18	D
04	7	20	11	5	23.84	44.569	-111.046	7.00	43	24	-134	41	45	20	D
04	7	20	11	5	23.84	44.569	-111.046	7.00	25	86	141	46	47	20	D
04	8	27	0	48	55.89	44.753	-110.817	4.00	262	84	-168	47	49	16	D
04	8	27	0	48	55.89	44.753	-110.817	4.00	311	50	-84	47	47	16	D
04	10	21	22	30	12.94	44.587	-110.719	5.23	68	45	-110	49	50	10	D
04	11	23	13	27	5.67	44.739	-111.053	5.10	247	63	163	44	47	10	D
04	11	23	13	27	5.67	44.739	-111.053	5.10	171	45	32	51	50	10	D
05	1	12	9	55	32.46	44.613	-110.695	5.99	257	63	142	52	54	16	D
05	2	21	1	49	22.96	44.769	-110.889	4.00	281	85	177	41	48	16	D
05	2	21	1	49	22.96	44.769	-110.889	4.00	135	42	-88	45	43	16	D
05	3	28	10	54	29.58	44.651	-111.118	3.00	267	62	145	43	49	14	D
05	3	28	10	54	29.58	44.651	-111.118	3.00	96	86	145	45	50	14	D
05	4	28	1	21	54.39	44.732	-111.112	9.67	217	74	-56	51	52	14	D
05	5	10	5	30	39.76	44.714	-111.141	5.97	26	63	-72	45	42	17	D
05	5	10	5	30	39.76	44.714	-111.141	5.97	299	40	-66	46	45	17	D
05	5	10	8	19	2.84	44.714	-111.143	5.79	179	30	-93	45	45	17	D
05	5	10	8	19	2.84	44.714	-111.143	5.79	283	39	-84	52	50	17	D
05	6	6	20	30	35.97	44.829	-110.948	4.99	246	82	-160	46	49	12	D
05	6	6	20	30	35.97	44.829	-110.948	4.99	79	56	-122	50	51	12	D
05	8	8	9	36	11.14	44.579	-110.979	10.13	268	82	164	41	40	11	D
05	8	8	9	36	11.14	44.579	-110.979	10.13	125	69	-102	48	49	11	D
05	8	14	20	7	30.76	44.641	-111.012	8.77	317	44	165	54	52	15	D
06	7	10	22	16	51.25	44.556	-110.794	7.57	285	76	175	48	49	14	D
06	7	10	23	30	42.63	44.548	-110.819	8.69	287	76	178	52	52	13	D
06	10	21	4	2	11.39	44.560	-110.945	7.01	120	71	178	46	44	12	D
07	2	17	18	59	18.49	44.780	-111.018	2.68	202	46	-88	57	56	12	D
07	2	20	22	15	54.60	44.782	-111.004	3.62	332	50	-99	41	44	14	D
07	2	20	22	15	54.60	44.782	-111.004	3.62	117	83	167	47	49	14	D
07	2	22	9	58	39.61	44.780	-111.003	2.51	65	87	157	40	43	10	D
07	3	1	12	17	51.88	44.578	-110.648	5.88	244	40	-93	43	45	20	D
07	3	9	13	44	49.96	44.773	-110.902	2.95	342	46	-104	39	39	13	D
07	9	22	10	7	42.04	44.657	-110.641	15.24	258	89	131	38	38	13	C
07	11	5	6	21	28.19	44.396	-110.616	4.58	355	40	-85	45	46	11	D
07	11	5	6	21	28.19	44.396	-110.616	4.58	266	37	-94	41	45	11	D
07	11	9	9	18	50.57	44.574	-110.924	8.74	252	87	141	42	37	15	D
07	11	25	0	31	27.17	44.745	-111.115	8.39	170	83	-125	49	49	9	D
07	12	25	16	20	4.41	44.743	-111.124	7.44	221	71	166	49	47	16	D
07	12	25	16	20	4.41	44.743	-111.124	7.44	242	22	-120	51	51	16	D

Yr	Mo	d	Hr	Mn	Sec	Lat	Long	Dep	Str	di	rk	E1	E2	NP	Q
07	12	25	17	55	1.64	44.750	-111.141	9.93	199	45	-174	56	56	8	D
07	12	31	3	29	21.25	44.770	-110.950	6.68	56	82	162	41	41	21	D
07	12	31	3	29	21.25	44.770	-110.950	6.68	231	66	138	43	49	21	D
07	12	31	20	38	45.33	44.758	-110.951	3.00	267	56	-176	47	48	13	D
08	1	9	21	37	37.43	44.771	-110.944	6.34	114	38	-83	41	38	22	D
08	1	9	21	37	37.43	44.771	-110.944	6.34	360	26	-113	31	48	22	D
08	1	9	21	43	53.66	44.737	-110.803	20.00	286	74	-112	40	46	25	D
08	1	10	1	35	17.31	44.767	-110.942	6.20	314	40	-125	34	41	16	D
08	1	10	1	35	17.31	44.767	-110.942	6.20	36	24	-110	46	50	16	D
08	1	26	1	43	43.58	44.541	-110.828	9.56	94	84	-137	46	46	16	D
08	3	11	10	57	22.69	44.557	-110.905	7.38	99	84	178	34	38	20	D
08	3	11	17	8	31.25	44.557	-110.897	8.10	82	84	143	60	60	14	D
08	3	12	9	9	36.58	44.577	-110.938	8.67	97	86	-174	34	36	19	C
08	3	25	11	59	37.86	44.701	-110.083	0.07	108	88	161	36	42	22	C
08	4	14	4	29	40.82	44.713	-110.814	10.94	83	40	-78	52	50	19	D
08	6	15	12	0	30.06	44.618	-110.672	3.44	1	38	-93	40	40	15	C
08	6	15	12	0	30.06	44.618	-110.672	3.44	255	46	-91	45	47	15	D
08	11	14	15	36	58.64	44.761	-110.804	4.68	67	88	-176	39	42	14	D
08	11	25	0	4	45.73	44.774	-110.794	4.40	70	75	-167	46	47	9	D
08	11	25	0	39	57.08	44.772	-110.799	4.46	349	47	-111	46	46	10	D
08	11	27	6	39	35.99	44.710	-111.048	20.00	249	22	-157	46	42	17	D
08	11	27	6	39	35.99	44.710	-111.048	20.00	210	72	-126	52	46	17	D
09	1	2	1	13	5.28	44.561	-110.373	1.70	319	37	-121	48	48	18	D
09	1	2	1	13	5.28	44.561	-110.373	1.70	102	24	-51	49	50	18	D
09	3	7	3	48	41.47	44.750	-111.091	9.56	55	88	174	45	44	11	D
09	6	30	15	52	5.90	44.733	-110.802	6.75	321	54	-113	39	41	18	D
09	6	30	16	52	33.02	44.737	-110.795	5.21	102	53	-128	52	52	19	D
09	8	19	0	41	43.08	44.620	-111.054	7.89	256	87	143	56	57	13	D
09	9	12	19	47	34.27	44.745	-111.105	7.47	247	81	-173	46	48	11	D
09	9	13	0	27	24.77	44.576	-111.079	11.29	286	63	138	52	51	14	D
09	9	16	4	54	56.15	44.680	-111.049	4.71	236	75	149	48	48	16	D
09	9	17	12	13	30.19	44.738	-111.116	7.35	51	73	161	45	41	12	D
09	9	17	12	13	30.19	44.738	-111.116	7.35	87	19	-126	48	44	12	D
09	12	6	17	49	1.24	44.716	-110.670	20.00	84	79	150	57	60	14	D
09	12	18	20	38	15.23	44.744	-111.027	7.82	123	61	-171	43	47	12	D
08	1	9	21	37	37.43	44.771	-110.944	6.34	329	35	-110	32	44	20	D
08	1	9	21	37	37.43	44.771	-110.944	6.34	54	27	-101	37	43	20	D

E1=Fault plane uncertainty

E2=Auxiliar plane uncertainty

NP=Number of P-wave polarity data

Q=Quality of solutions

Table 4.3: Classification of the faulting type basing on rake values

Faulting type	***Rake values***
Normal	-60< rake <-120
Reverse	60< rake <120
Normal-oblique	-30 < rake < -60 -120 < rake < -150
Reverse-oblique	30 < rake < 60 120 < rake < 150
Strike-slip	-150 < rake < -180 150 < rake < 180

According to the classification described in table 4.3, the 133 C and D quality solutions were distinguished basing on the faulting type: 55 focal mechanisms show a normal-faulting style, 1 is a reverse-faulting mechanism, 27 are normal-oblique mechanisms, 1 is a reverse-oblique mechanism and 49 are strike-slip mechanisms. The fact that most mechanisms are typical of an area interested by tectonic extension, characterized by normal faults, is not surprising, because Yellowstone volcanic field belongs to the deformation field of the Basin and Range province, whose unique topographic expression is the result of extension and thinning of the lithosphere, shown by many listric normal faults and opposing normal faults that produce a “horst and graben” geometry. The

extension direction of the Basin and Range area is NE-SW and it dominates the crustal deformation at Yellowstone (Christiansen, 2001).

CHAPTER 5

FOCAL MECHANISM INVERSION AND MODEL STRESS-FIELD SOLUTIONS FROM P-WAVE POLARITY DATA AND FOCAL MECHANISMS

5.1 Stress-field determination: theory

Many procedures for resolving the stress field from individually determined focal mechanisms have been developed throughout the years (Angelier, 1984; Gephart and Forsyth, 1984; Michael, 1987): earthquakes can be considered as passive markers of stress and they can be used to estimate the best uniform stress field within limited space-time windows.

Other authors have used P wave polarity data and takeoff angles to calculate focal mechanisms and solve for the stress field (Rivera and Cisternas, 1990; Horiuchi et al., 1995; Robinson and McGinty, 2000; Abers and Gephart, 2001; Hardebeck and Shearer, 2003; Hardebeck, 2006; Waite and Smith, 2004). Using the polarity and takeoff angle data directly prevents any possible error in the fault plane solutions from being introduced into the stress field computations.

The inversions constrain a dimensionless, deviatoric stress tensor, made up by four independent parameters, three defining the orientations of principal stress axes ($\sigma_1 \geq \sigma_2 \geq \sigma_3$) and a fourth which determines the magnitude of σ_2 relative to σ_1 and σ_3.

$$R = \frac{\sigma_2 - \sigma_1}{\sigma_3 - \sigma_1}$$

In order to invert for these four stress parameters, the information among several earthquake focal mechanisms, which indicate the direction of slip on either of two possible fault planes (and are assumed to record directions of shear stress within a uniform stress field), are combined.

One of the drawbacks of these stress inversion techniques is that the analysis is based on earthquake focal mechanisms, which are characterized by complex uncertainties. There is rarely a full accounting of the real uncertainty in the determination of the focal mechanisms, while it is possible to assess the uncertainty of the stress inversion procedure on the basis of known focal mechanisms. For most small events, focal mechanisms are determined from P-wave first motions by fitting orthogonal nodal

planes, a nonlinear process subject to a variety of errors. Compounding these uncertainties, the ray takeoff angles used to compare P waves with nodal planes depend on an imperfectly known seismic velocity structure, leading to additional error (Abers and Gephart, 2001).

Some diversity of focal mechanisms is required to limit the range of acceptable stresses, but if the inferred diversity is not real because it is due to the scatter caused by noisy data and not by a real diversity of fault plane orientations, then the use of the data might become misleading (Abers and Gephart, 2001).

The MOTSI inverse scheme (Abers and Gephart, 2001) gives the possibility of resolving the four-parameter stress tensor directly from first motions, thus circumventing the reliance on the intermediate step of independently compiling focal mechanisms. It uses P wave polarity data and takeoff angles directly, instead of focal mechanisms as input.

This method follows the focal mechanism stress inversion (FMSI) algorithm of Gephart (1990) in exploring a four-parameter stress space on a grid in search of a best fitting stress model and confidence estimates. In MOTSI,

two nested grid searches are computed, in order to identify the best stresses and focal mechanisms. The first, outer search is conducted over a wide range of the four stress parameters, testing independent stress models one after the other. Specifically, the algorithm tests orientations of a “primary” principal stress axis over a uniform spherical grid of directions. This primary principal stress may be either σ_1 or σ_3 and, for each primary stress orientation, it tests secondary stress axes at even increments of angle Φ in the orthogonal plane, and searches over even increments of R (Gephart, 1990). Each unique combination of four parameters represents a stress model that has to be tested. In this study, the trial grid was imposed to have a density of 10° node spacing in both primary and secondary stresses, and R varies from 0 to 1 at increments of 0.1. The second, inner search is conducted once for each stress model over a finer grid of fault planes and identifies for each event the focal mechanisms that best fit the first motions.

Among the focal mechanisms identified with the second, inner search, the program finds the one that is most in agreement with first motions for each event. Starting with raw first-motion data is an attempt to avoid that

incorrectly assigned focal mechanisms (from limited or conflicting first motions) might bias the results favoring heterogeneous stresses.

This procedure assumes that the earthquake generating stress is homogeneous and no a priori fault orientation information is assumed. The fault slip direction is defined to be parallel to the direction where the shear stress is at a maximum. With this method, the first-motion data are weighted basing on the probability of the pick being correct. The highest weights are given to data farthest from the nodal planes, where the P wave radiation pattern predicts the amplitude is largest and the probability of an incorrect pick lowest.

Two parameters describe the probability that the P-wave pick is correct. The first, α, is approximately the theoretical P wave amplitude below which pick reliability drops off considerably (near nodal planes). The second, γ, is the overall estimate of mispicked data and it is based on the fraction of inconsistent first motions in the entire data set. When α and γ are imposed to be equal to 0.01, a data set is assumed to be near perfect, while if those values increase up to α=0.1 and γ=0.2, we would assume that the data set is unusually noisy. Confidence limits grow with increasing γ (Abers and

Gephart, 2001). In this study, both α and γ were set equal to 0.05. Another parameter, called pgoofN, was set equal to 1.0 to disregard nodal picks.

Because of the assumption of stress homogeneity, it is necessary to assess whether the stress field in a volume is homogeneous. An approach described by Abers and Gephart (2001) compares the fit of focal mechanisms determined without regard to the stress field, called S, with those constrained by the best fitting stress field, S'. Formally, the MOTSI method tests the null hypothesis, H_0, that the focal mechanisms fit first motions equally well as ones determined without regard to stress with MOTSI-FP which generates an aggregate score S_0. Rejecting H_0 is a strong indicator of stress heterogeneity because it indicates that the stress constraint significantly degrades fits.

The heterogeneity hypothesis H_0 can be rejected at the confidence level 1-β when

$$dS=(S_0-S_{max}) > Z_\beta\sqrt{2}$$

where Z_β is the standard normal deviate at confidence level β. For each inversion the statistic dS is estimated as is the confidence limit β at which dS is significant. The test is one because $S_0 \geq S_{max}$ always; the $\sqrt{2}$ accounts

for the pooled variance of the difference of two random variables based upon equal numbers of binomial observations (Larson and Marx, 1981). Thus this method rejects the hypothesis H_0 and infer heterogeneous stress at the 95% confidence level when $dS > 2.32$ ($Z_{0.95}$=1.64).

Two separate routines can be used to fit best fitting focal mechanisms to the first motion data, both with and without constraining the stress field to that which was found in the inversion. This makes possible to determine the effects of the stress constraint on suites of focal mechanisms. Focal mechanisms are constrained by forcing the slip direction to be parallel to the maximum resolved shear-stress direction.

5.2 Model stress-field: results

A stress model computed starting from all 369 focal mechanisms has σ_1 plunging 79° and trending 176°, σ_3 nearly horizontal and trending 49° and R=0.5 (figure 5.3). An iterative trial-and-error approach was used to subdivide the Yellowstone region into smaller areas of approximately homogeneous stress. The selection of these areas was based on earlier

work (e.g., Waite and Smith, 2004) and on the general trends in T-axis orientations. In this study, ten different areas have been defined.

The focal mechanism data were initially divided into smaller areas and stress model solutions were computed in each area and examined for homogeneity. If the stress model computed resulted in significant differences in the fit scores between the constrained and unconstrained focal mechanisms for that area (i.e., $dS > 2.32$), smaller or slightly different areas were tested for the stress computation. Sometimes, merging areas was useful while in some other cases, reducing the size of an area so that it was homogeneous caused an increase in the solution uncertainty so further subdivision was not done. Some diversity in the focal mechanisms had to be preserved to achieve a well constrained solution (Abers and Gephart, 2001).

In this study, ten different areas were defined (figure 5.9). The 95% confidence regions for both σ_1 and σ_3 are relatively small, especially in the areas with more earthquakes. The data density looks heterogeneous and the T axes orientations show an apparent rotation of horizontal extension

across the Yellowstone region, suggesting that the deviatoric stress at Yellowstone varies spatially.

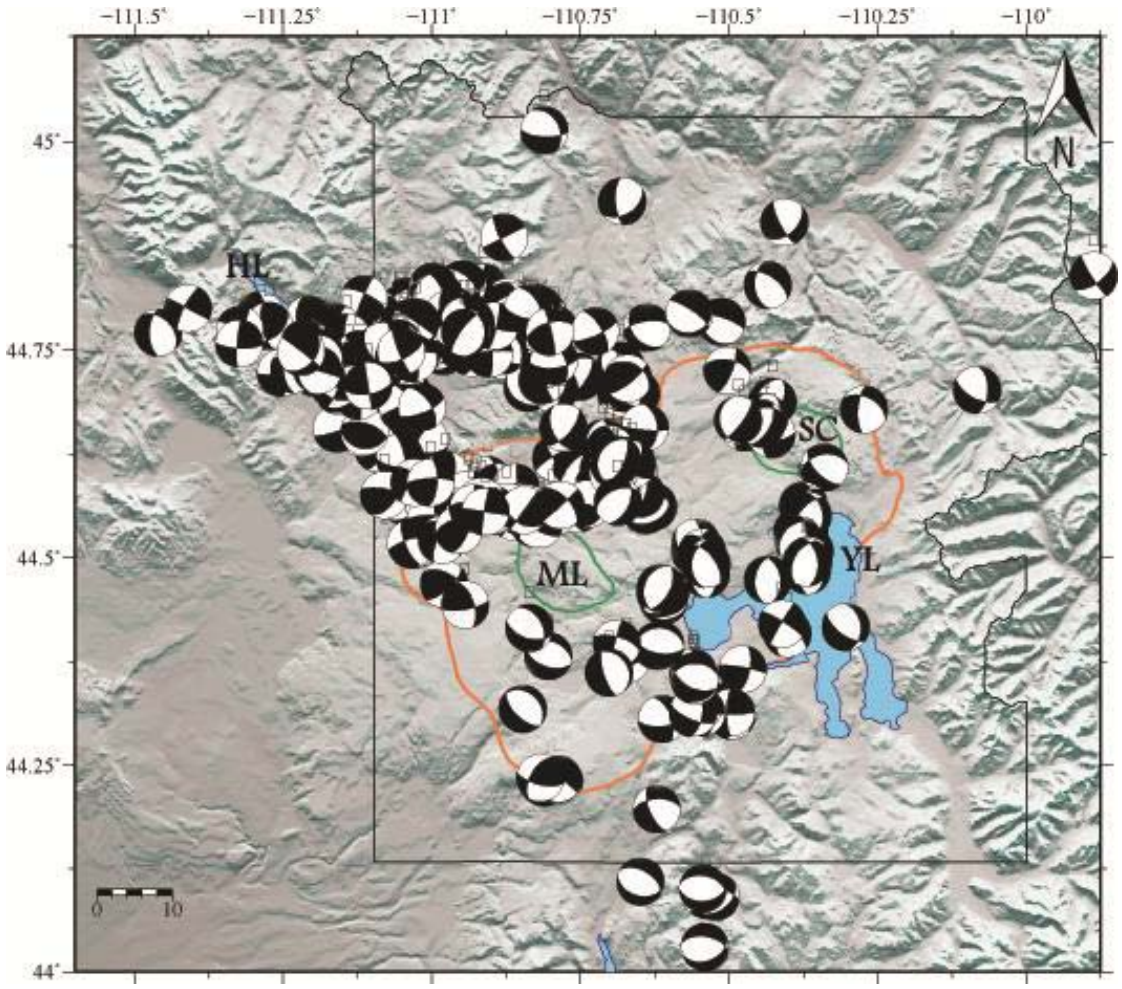

Figure 5.1: Complete set of 369 double-couple focal mechanism solutions computed by Motsi (Abers and Gephart, 2001) for the period of time between 1988 and 2010. The orange line represents the 0.64 Ma Yellowstone caldera boundary, the green lines represent Mallard Lake resurgent dome (ML) and Sour Creek resurgent dome (SC). YL= Yellowstone Lake; HL=Hebgen Lake. The topographic data is provided by the USGS National Elevation Dataset.

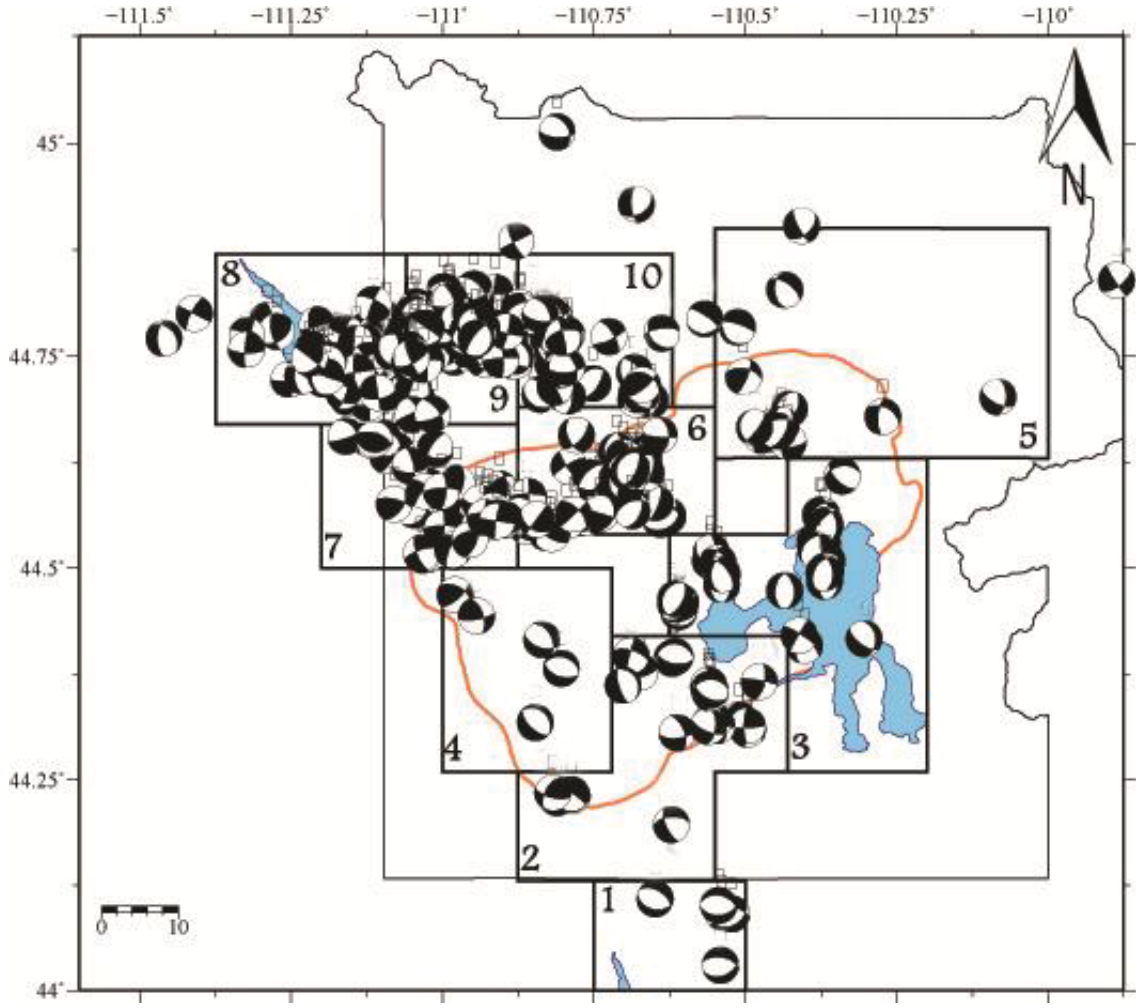

Figure 5.2: Focal mechanism data in this study were divided into ten smaller areas, based on regions with a relatively homogeneous stress. The ten boxes are outlined in black. The orange line represents the 0.64 Ma Yellowstone caldera boundary. Yellowstone Lake and Hebgen Lake are shown.

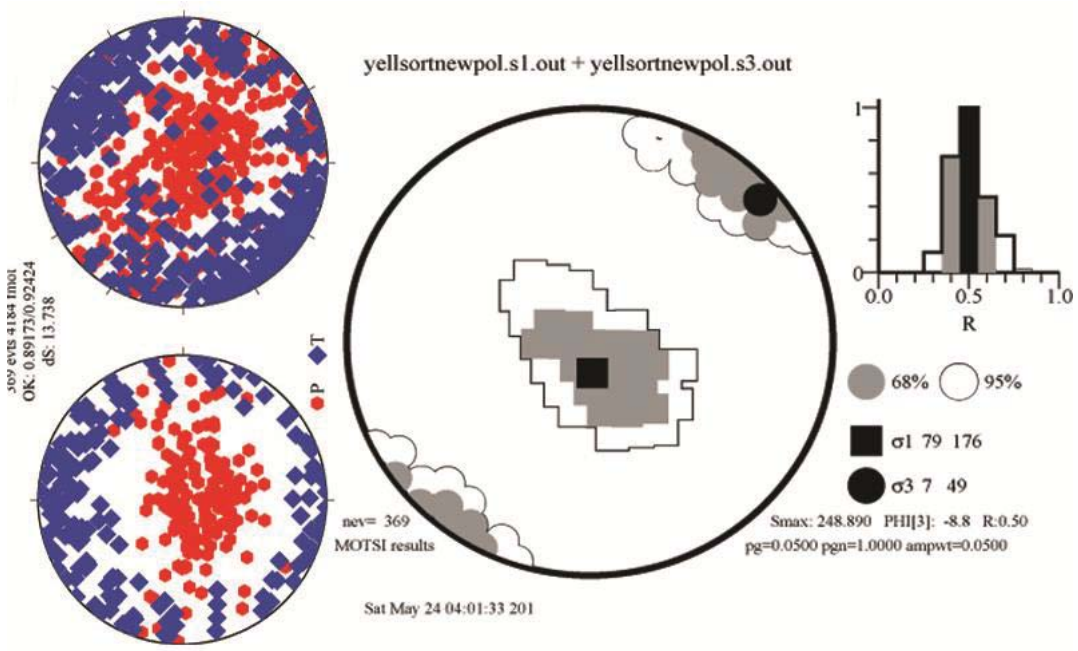

Figure 5.3: Stress model computed from all 369 focal mechanisms. P and T axes for all earthquakes in each area are shown for focal mechanisms unconstrained and constrained by the stress solution. Best fitting σ_1 and σ_3 are plotted with black square and circle, respectively. The 68% confidence region is shown in gray and the 95% confidence region is white.

The final areas and the corresponding focal mechanisms of each area are shown in figures 5.1 and 5.2. The corresponding solutions as well as the P and T axes for the stress-constrained and unconstrained focal mechanisms are plotted in figures 5.4-5.8. Some areas, such as the southern and north-eastern inside part of the caldera and the area south of the caldera, are too sparsely populated to compute a reliable stress tensor inversion so not all of the focal mechanisms data can be considered to elaborate an interpretation. The seismic activity considered in this study is concentrated especially close to the north-western caldera boundary, but it was also possible to compute stress inversions inside the caldera because the activity looks less sparse than in previous studies (Waite and Smith, 2004).

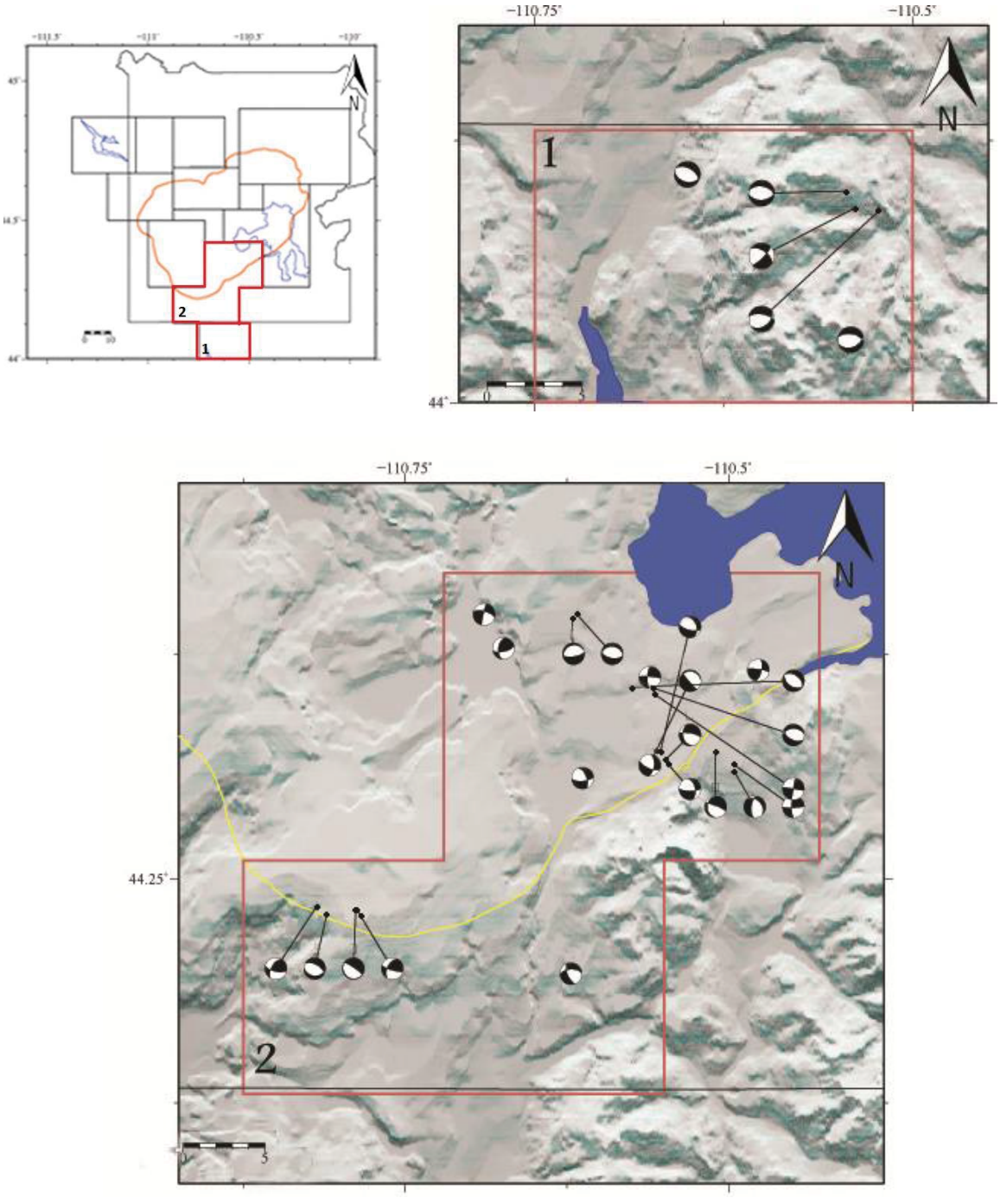

Figure 5.4: Area 1 and 2 shown in details. The yellow line represents the boundary of the 0.64 Ma Yellowstone caldera. The red line is the box border. The topographic data is provided by the USGS National Elevation Dataset.

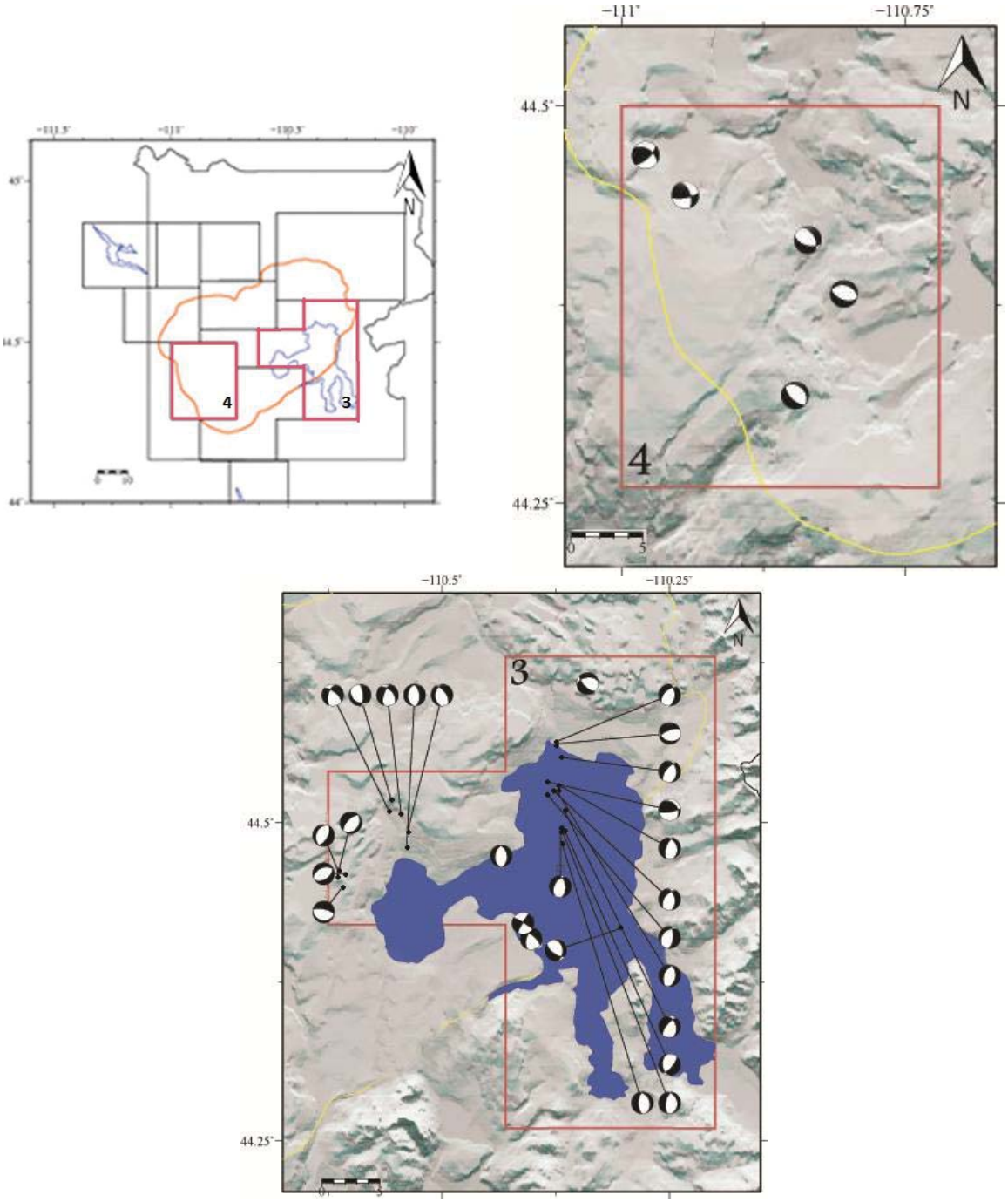

Figure 5.5: Area 3 and 4 shown in details. The yellow line represents the boundary of the 0.64 Ma Yellowstone caldera. The red line is the box border. The topographic data is provided by the USGS National Elevation Dataset.

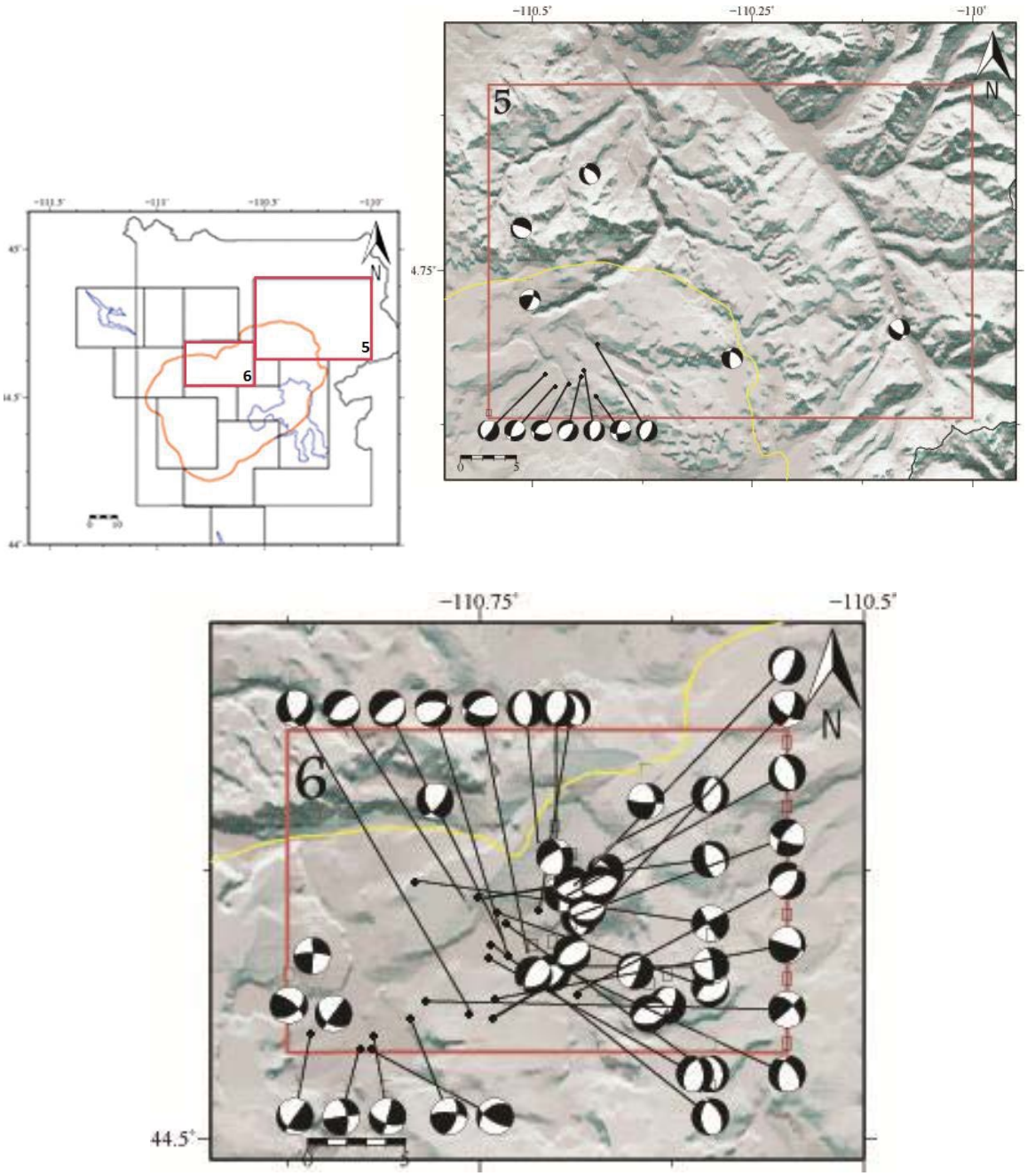

Figure 5.6: Area 5 and 6 shown in details. The yellow line represents the boundary of the 0.64 Ma Yellowstone caldera. The red line is the box border. The topographic data is provided by the USGS National Elevation Dataset.

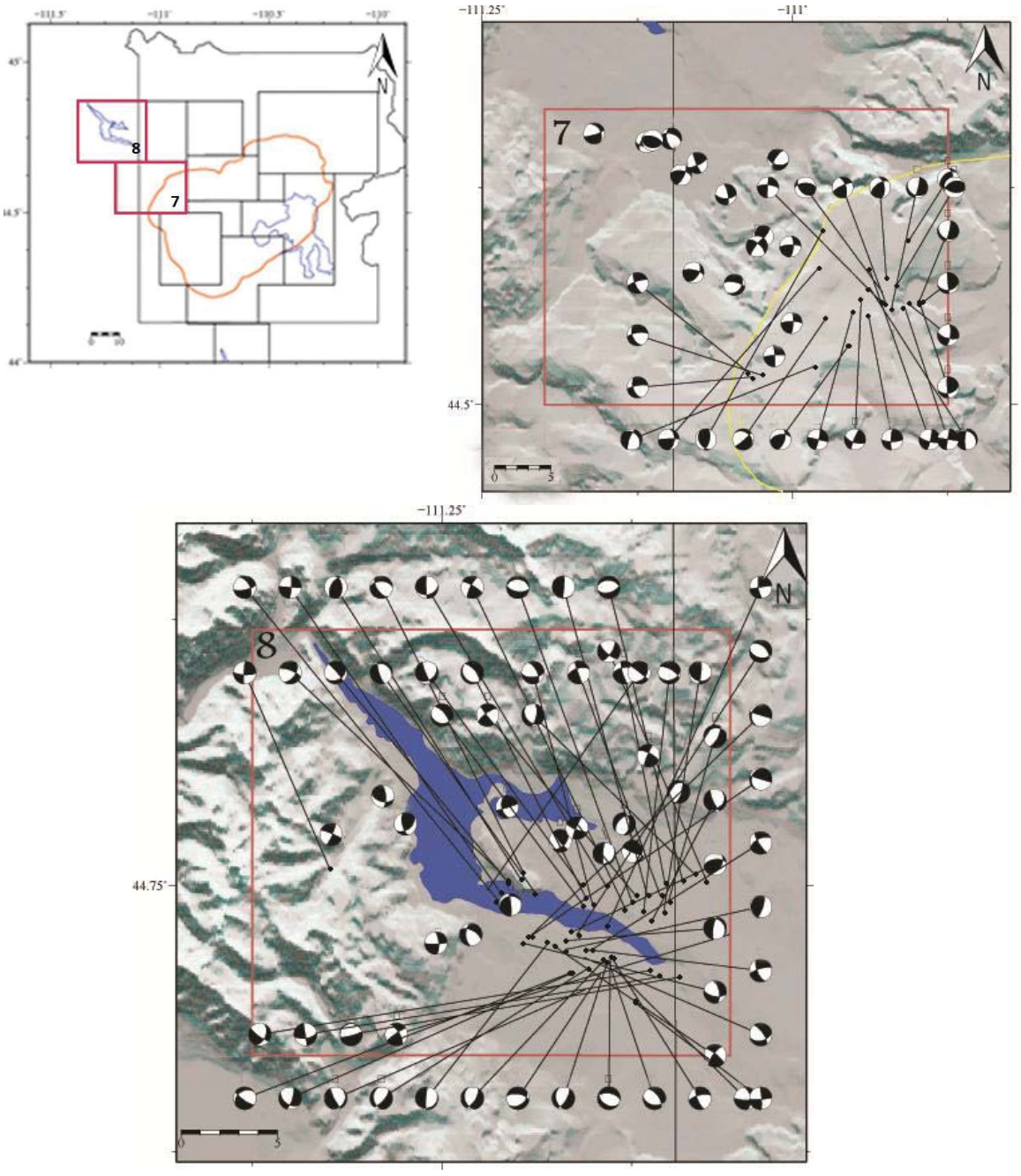

Figure 5.7: Area 7 and 8 shown in details. The yellow line represents the boundary of the 0.64 Ma Yellowstone caldera. The red line is the box border. The topographic data is provided by the USGS National Elevation Dataset.

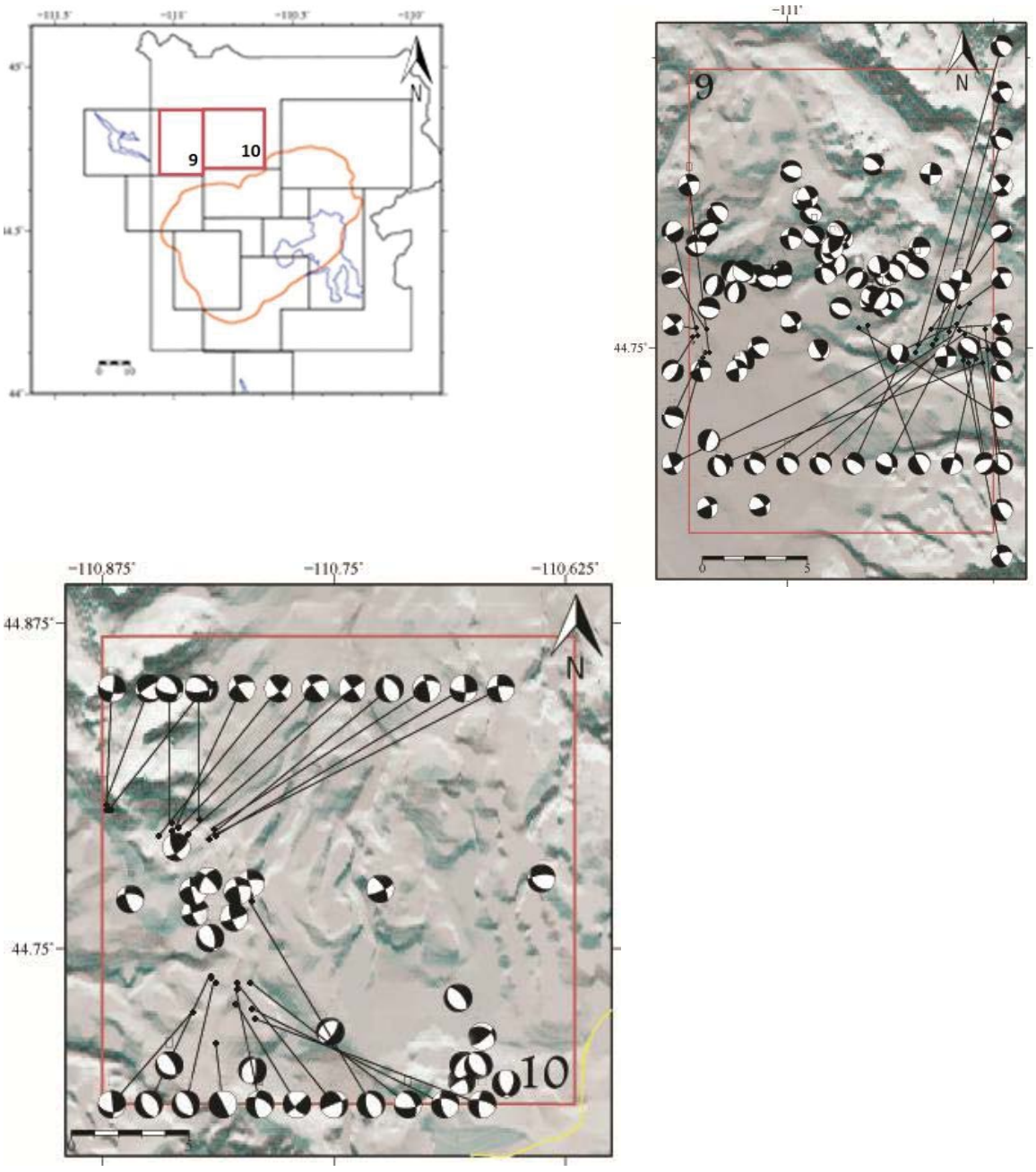

Figure 5.8: Area 9 and 10 shown in details. The yellow line represents the boundary of the 0.64 Ma Yellowstone caldera. The red line is the box border. The topographic data is provided by the USGS National Elevation Dataset.

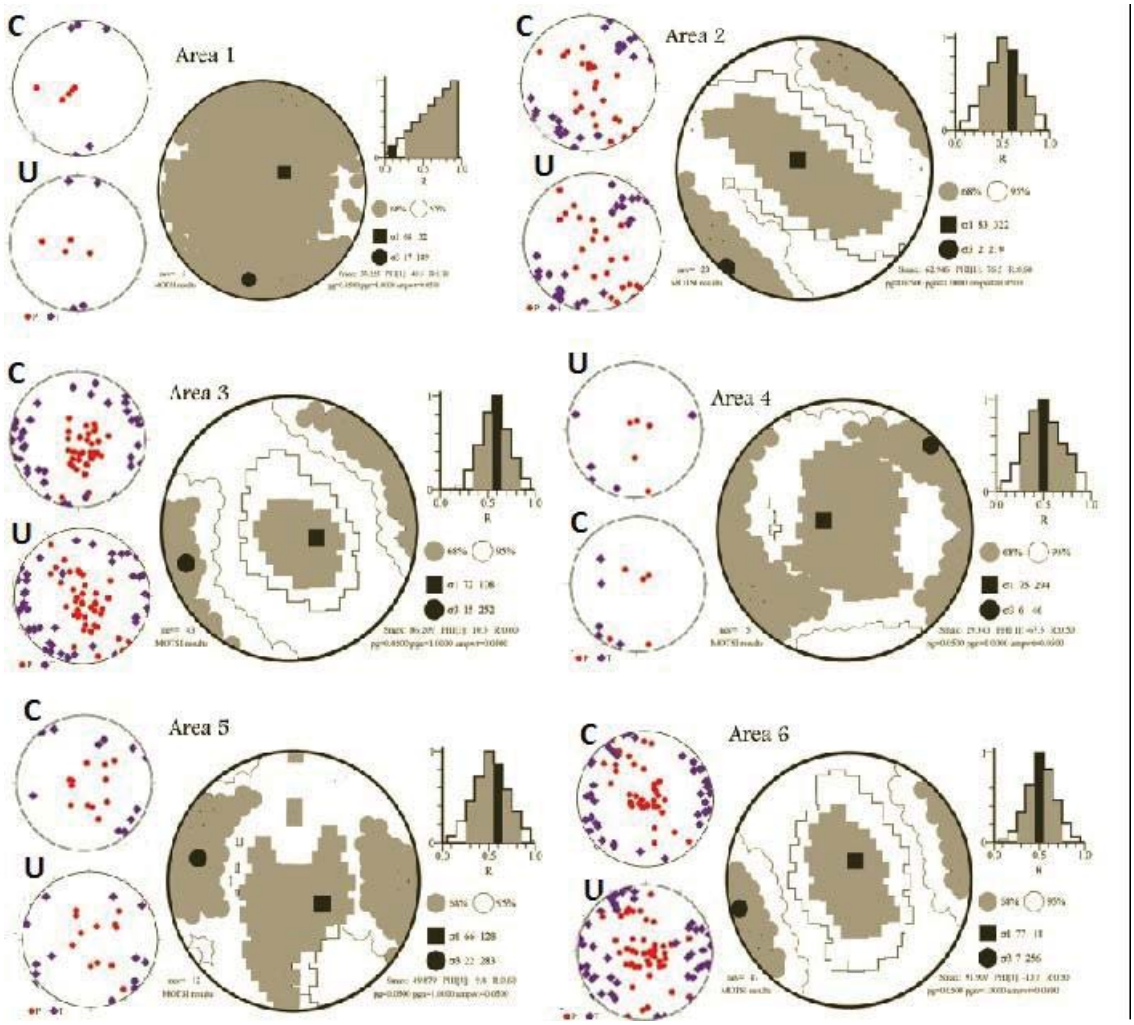

Figure 5.9A: Stresses for the ten areas within Yellowstone volcanic field. P and T axes for all earthquakes in each area are shown for focal mechanisms unconstrained (u) and constrained (c) by the stress solution. Best fitting σ_1 and σ_3 are plotted with black square and circle, respectively. The plunge and trend of each is written. The 68% confidence regions are shown in gray, while the 95% confidence regions are white. Subdivisions were decided according to the principle of minimizing heterogeneities in the stress field of the overall region. Areas 1 and 4 have only 4 and 5 respectively, so the stress inversions are not very meaningful.

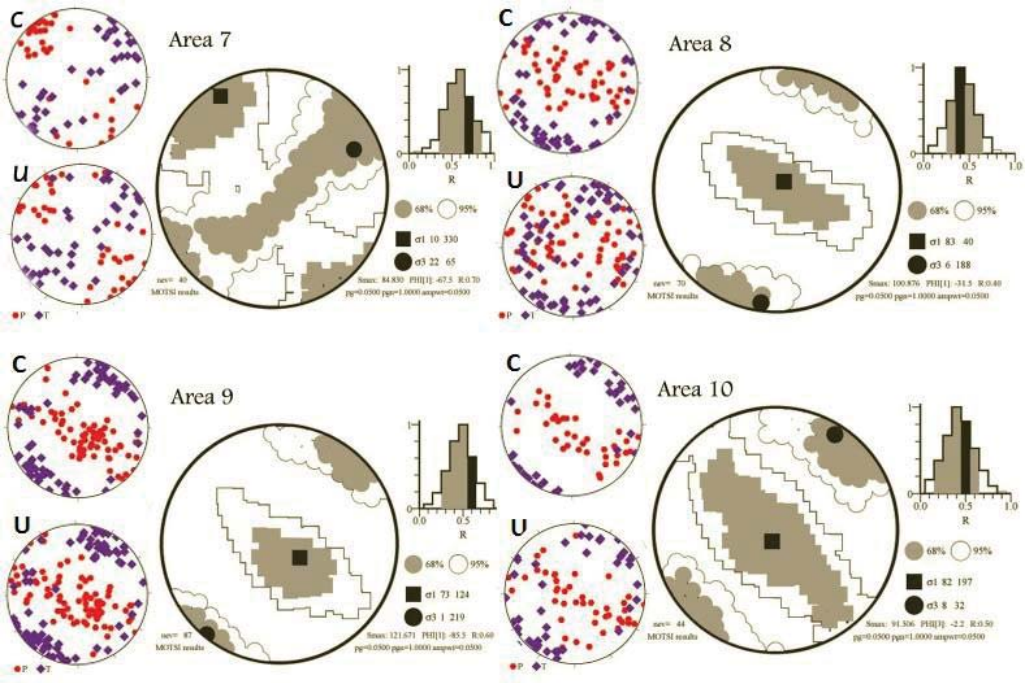

Figure 5.9B: Stresses for the ten areas within Yellowstone volcanic field. P and T axes for all earthquakes in each area are shown for focal mechanisms unconstrained (u) and constrained (c) by the stress solution. Best fitting σ_1 and σ_3 are plotted with black square and circle, respectively. The plunge and trend of each is written. The 68% confidence regions are shown in gray, while the 95% confidence regions are white. Subdivisions were decided according to the principle of minimizing heterogeneities in the stress field of the overall region. Areas 1 and 4 have only 4 and 5 respectively, so the stress inversions are not very meaningful.

5.3 Model stress-field: interpretation of the results

The regional extension direction, inferred from fault scarp striations and in situ measurements (Zoback, 1992), is consistently E-W through central Utah, perpendicular to the eastern boundary of the Basin and Range region. This direction is also indicated by north striking en echelon normal faults to the south of the Yellowstone caldera, including the Teton fault, and the north striking Gallatin fault between Norris Junction and Mammoth Hot Springs (Christiansen, 2001). These extension structures located north and south of the caldera were thought to be linked by two alignments of postcaldera volcanic vents within the caldera (Ruppel, 1972; Christiansen, 2001).

East to south-east striking faults to the W and NW of Yellowstone, including the Hebgen Lake and Red Canyon faults, indicated that extension is approximately N-S in that region (Doser, 1985). To the N and W of Yellowstone, geologically and seismically determined extension directions were generally NE-SW with locally more N-S extension in the area of the 1959 Hebgen Lake earthquake (Doser, 1985; Eddington et al., 1987; Zoback, 1992; Nabelek and Xia, 1995). The direction of extension in the Hebgen

Lake area from GPS data was NNE-SSW (Puskas et al., 2002; Nishimura and Thatcher, 2003; Waite and Smith, 2004; Puskas et al., 2007).

The stress-field inversion results in this study seem to confirm what was previously discovered, except the supposed E-W extension direction south of the caldera, where the seismicity looks too sparse to consider the results reliable enough. Moreover, we did not have adequate data to constrain the stress direction west of the caldera; the seismicity in that area was not part of our database.

According to our results, σ_1 is nearly vertical all over the Yellowstone area. The direction of σ_3, near horizontal everywhere, rotates from NNE-SSW near the Hebgen Lake fault zone (area 8), to ENE-WSW near Norris Junction (area 10). These areas are characterized by a higher density of earthquakes, which mainly occurred in an E-W band from the Hebgen Lake fault zone to Norris Junction and north of the Mallard Lake resurgent dome, inside the caldera. The σ_3 direction looks fairly uniform and nearly parallel to the direction of extension measured by GPS (Puskas et al., 2002).

The E-W band of highest earthquake activity includes areas with nearly N-S extension, perpendicular to the extension direction of the Gallatin fault, which is located immediately north of the area. The study by Waite and Smith (2004) suggested that the N-S extension may have been related to viscoelastic relaxation in the upper mantle and lower crust following the 1959 Hebgen Lake earthquake: the N-S extension may represent a result of the northeastward migration of the Yellowstone hotspot (Waite and Smith, 2004).

The areas 2, 3, 5, 6, 7 include the 0.64 Ma Yellowstone caldera boundary and they are all characterized by a stress-field σ_3 nearly parallel to this boundary (see figure 5.10).

The σ_3 direction in the area around Norris Geyser Basin, which corresponds to areas 6 and 10 in this study, seems to have changed throughout the years: in the study by Waite and Smith (2004) it was ENE-WSW, while the σ_3 direction computed in this study is NNE-SSW. This could reflect the time-varying stress field, but it is interesting to notice that the other σ_3 directions computed in the study are mostly unchanged, except that one area.

The σ_3 direction in area 1, which is located south of the Yellowstone caldera boundary, appears to be oriented N-S, but unfortunately this area is composed by just 5 events and 55 first motions, so it is difficult to compute a reliable stress tensor inversion. In fact, in this area and also in other areas which are characterized by few focal mechanisms (area 4, with just 5 events, and area 5, with 12 events), the 68% and 95% confidence regions overlap. Elsewhere, σ_3 is well constrained, especially close to the Hebgen Lake Fault zone and Norris Junction.

Despite an effort to discriminate areas of homogeneous stress, three areas show large values of dS: area 3, which is located in the Yellowstone Lake area, and areas 8, and 9, north of the caldera. Area 6 has a value of dS close to the 2.32 limit (dS=2.268). Area 8 has the largest dS (dS=3.362), but presents one of the best-constrained stress models. The lowest dS (dS=0.046) is located in area 1. The spatially largest area is area 5, in the north-eastern part of the caldera, it includes 12 earthquakes and however it has one of the lowest dS, which looks equal to 0.92. Table 5.1 lists the best fit models for each area.

Table 5.1: Nev=number of events, NFM=number of first motions, dS=difference between stress-constrained and unconstrained focal mechanism

Area	Nev	NFM	σ_1 (Tr. Pl.)	σ_3(Tr.Pl.)	dS
1	5	55	68° 52	17° 189°	0.046
2	23	213	83° 322°	2° 219°	0.355
3	43	430	72° 108°	15° 252°	2.855
4	5	50	75° 294°	6° 46°	0.216
5	12	143	66° 128°	22° 283°	0.92
6	47	555	77° 18°	7° 256°	2.268
7	40	515	10° 330°	22° 65°	1.634
8	70	741	83° 40°	6° 188°	3.362
9	87	1014	73° 124°	1° 219°	2.746
10	44	519	82° 197°	8° 32°	0.643

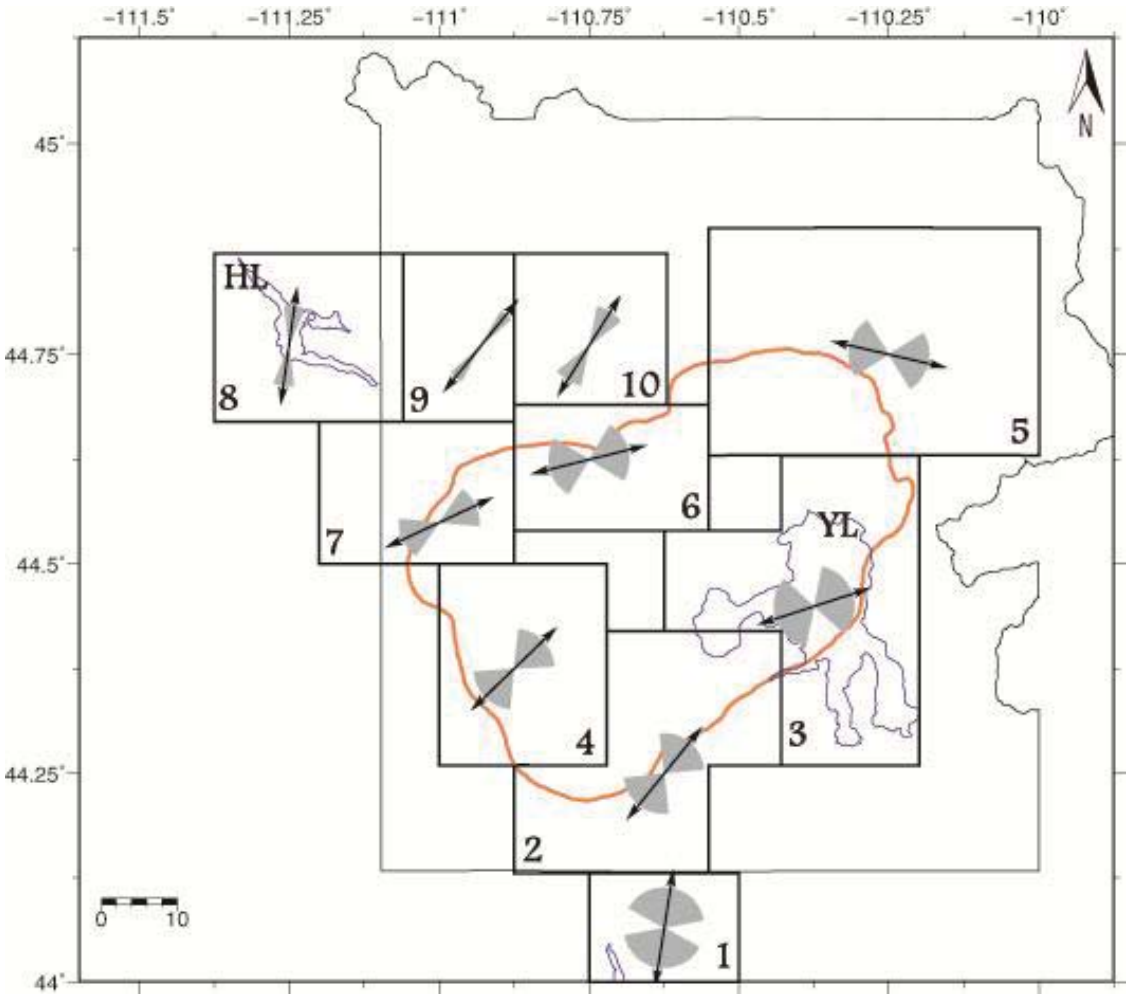

Figure 5.10: Map of areas that were used in stress tensor inversions. The thin black arrows indicate the direction of σ_3 for each area and the grey wedges indicate the 95% confidence intervals.

According to our stress inversions, the direction of extension throughout the 0.64 Ma Yellowstone caldera looks nearly ENE. This is consistent with what was supposed by previous studies. In fact, if alignments of volcanic vents within the caldera can be really considered as links between extensional structures north and south of the caldera as has been suggested (Ruppel, 1972; Christiansen, 2001), then the orientation of those alignments indicate ENE extension within the caldera. These structures may represent zones of weakness linking the normal faults to the north and south (Waite and Smith, 2004). This study, according to the minimum principal stress directions, confirms that the N-S striking faults to the north of the caldera may no longer be active, as it was already revealed in the study by Waite and Smith (2004).

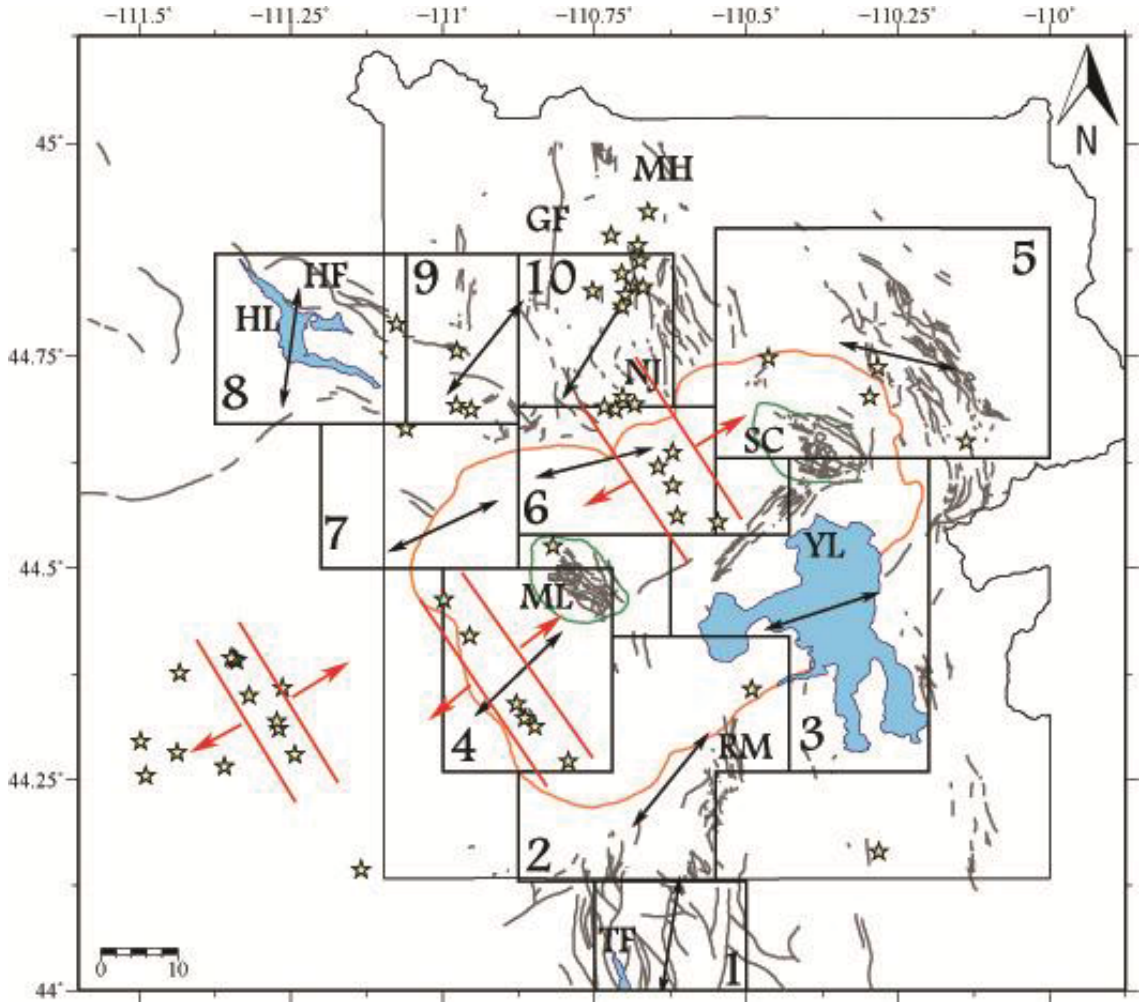

Figure 5.11: Geological features of Yellowstone volcanic field. Black arrows are stress-field σ_3 directions inferred in this study. Green lines represent Mallard Lake resurgent dome (ML) and Sour Creek resurgent dome (SC), respectively. Lines and arrows around the volcanic vents, represented with yellow stars, indicate the approximate extension direction that may be inferred from the alignments of the vents. Grey lines are Quaternary faults. Two- letter abbreviations are as follows: Gallatin Fault (GF), Hebgen and Red Canyon Faults (HF), Hebgen Lake (HL), Mammoth Hot Springs (MH), Norris Junction (NJ), Red Mountain Fault Zone (RM), Teton Fault (TF), and Yellowstone Lake (YL).

CHAPTER 6

DEFORMATION SOURCES OF THE YELLOWSTONE VOLCANIC PLATEAU

6.1 Gas and magmatic sources beneath Yellowstone volcanic plateau

One of Yellowstone's most important features is an expansive hydrothermal system which is caused by the circulation of hot water along fracture systems in the upper crust heated from below by crystallizing magma. The high heat flux in Yellowstone, estimated to be ~1800 mW/m^2, which is 30 times higher than the continental average, is further evidence for a large body of crystallizing magma (Fournier et al., 1976). Seismologically, crustal magma bodies are generally characterized by low P-wave velocities (V_p) and high P-wave to S-wave ratios (V_p/V_s).

The Yellowstone crustal magma reservoir is an integral part of the larger Yellowstone volcanic field, in which a fixed Yellowstone mantle plume feeds buoyant transport of basaltic melt and heat from mantle depths into the crust beneath Yellowstone National Park. This magma reservoir is the source of the caldera-forming dominantly rhyolitic eruptions of Yellowstone

and the bimodal basaltic-rhyolitic volcanism of the Snake River Plain volcanic field.

The first local earthquake tomography studies at Yellowstone (Benz and Smith, 1984; Miller and Smith, 1999) imaged an extended body of low P-wave velocity at depths of ~6-12 km, confirming the likely existence of crystallizing magma beneath the Yellowstone caldera. These studies, however, used limited earthquake data up to 1994 and very little S-wave data, because of the small number of three-component seismometers in Yellowstone at that time. S-wave modeling is important for detecting fluids in volcanic systems, because of the sensitivity of the P-wave to S-wave ratio to changes in pore fluids (Mavko and Mukerji, 1995).

According to the study by Miller and Smith (1999), the Sour Creek resurgent dome presented both low P and S velocities and higher V_p/V_s ratios at a depth of ~6 km, which demonstrated the presence of a moderate volume of partially melted rock, and the low P velocities beneath the Mallard Lake resurgent dome at a depth of ~8 km, despite a lack of corresponding S velocity and V_p/V_s ratio, had been also interpreted as a zone of partially

melted rock. The smaller depth extent of the Mallard Lake dome P velocity anomaly implied a smaller volume of partial melt than that beneath the Sour Creek dome (Miller and Smith, 1999).

In the study by Husen et al. (2004), the previous works were extended to image the crustal structure beneath Yellowstone thanks to significant technical upgrades and an expansion of the permanent seismic network at Yellowstone, providing more S-wave data.

The tomographic images confirmed the existence of a large body of low V_p at depths greater than 8 km beneath the Yellowstone caldera: absolute V_p in this case is as low as 5.4 km/s (Husen et al., 2004).

The V_p and V_p/V_s images revealed a new significant feature: at the shallow depth of ~2 km, a strong low V_p and low V_p/V_s anomaly is located in the northwestern part, close to the caldera boundary, with an absolute velocity of 4.6 km/s (Husen et al., 2004). This anomaly was modeled as a change in pore fluid from liquid to gas, probably CO_2, at shallow crustal depths. The location of this anomaly is close to the 1985 earthquake swarm and this suggests a model in which CO_2 might be part of magmatic fluids exsolved

from a large crystallizing magma body beneath the Yellowstone caldera and occasionally migrating outwards of the caldera (Husen et al., 2004). Many of the earthquake swarms in the area have been related to migrating magmatic fluids from the magma reservoir.

A similar low V_p anomaly is located further to the east just north of the caldera boundary, which has an absolute velocity of 4.6 km/s. However, V_p/V_s in this area is not resolved, so it looks difficult to interpret this second anomaly as evidence for another gas filled body (Husen et al., 2004).

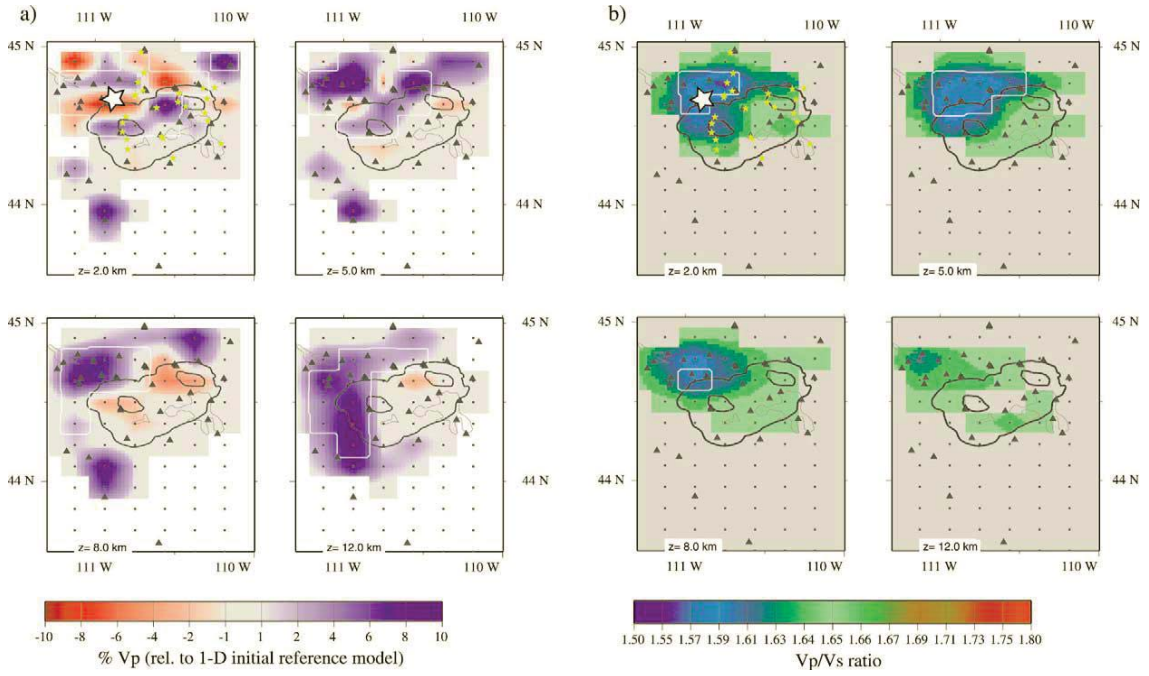

Figure 6.1: Tomographic results of 3D (a) V_p and (b) V_p/V_s models (Husen et al., 2004). Results are in horizontal cross sections at different depths as indicated. Areas with no ray coverage are masked. Yellow stars mapped hydrothermal features (Christiansen, 2001) and large white star marks the location of the 1985 earthquake swarm (Waite and Smith, 2002).

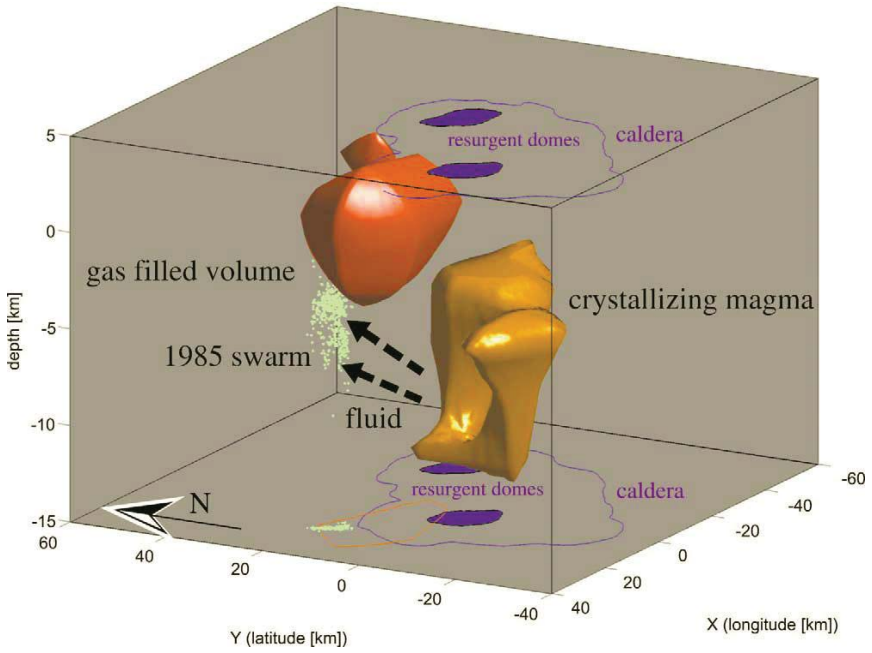

Figure 6.2: 3D view of low V_p beneath Yellowstone as imaged by local earthquake tomography in the study by Husen et al., 2004. Orange body represents the location of a possible crystallizing magma body beneath the caldera; red body outlines the location of shallow, possible gas filled volume. The green dots are hypocenter locations of the 1985 swarm. Dashed arrows represent a possible fluid migration from the crystallizing magma body towards gas filled volume caused by the 1985 swarm (Husen et al., 2004).

A new study by Farrell et al. (2014) computed a different estimate of the Yellowstone magma reservoir with a 5-15% partially melted volume 2.5 times larger than the previous tomographic determination. The three Yellowstone giant eruptions 2.1, 1.3 and 0.64 Ma ago erupted 2,500 km^3, 280 km^3 and 1,000 km^3 of material, respectively (Christiansen, 2001): based on Farrell et al. (2014), there would be sufficient melt volume for another eruption with a similar size to the 1.3 Ma eruption. Thanks to a better coverage in the northeastern part of the Yellowstone volcanic field, in the study by Farrell et al. (2014) it was possible to display the shallowest portion of the Yellowstone magma reservoir, which underlies the large Hot Spring Basin Group, characterized by a huge hydrothermal alteration and one of the most thermally active basins in Yellowstone (DeNosaquo et al., 2009; Werner et al., 2008).

The study by Farrell et al. (2014) found out that a continuity of low P-wave velocities about 15 km NE of the Yellowstone caldera coincided with the largest negative Bouguer gravity anomaly, ~80 mGal, in the Yellowstone plateau: the distance the Yellowstone hotspot would migrate because of the SW motion of the North America plate, at about 2.35 cm/yr (Anders et

al., 2014), since the 0.64 Ma Yellowstone eruption, shows an apparent NE migration of about 15 km which is similar to the NE extent of the low velocity body imaged in this study. This suggests that the apparent NE migration of the hotspot over the last 640,000 years has fueled the crustal magma reservoir through new magma pathways NE of the caldera.

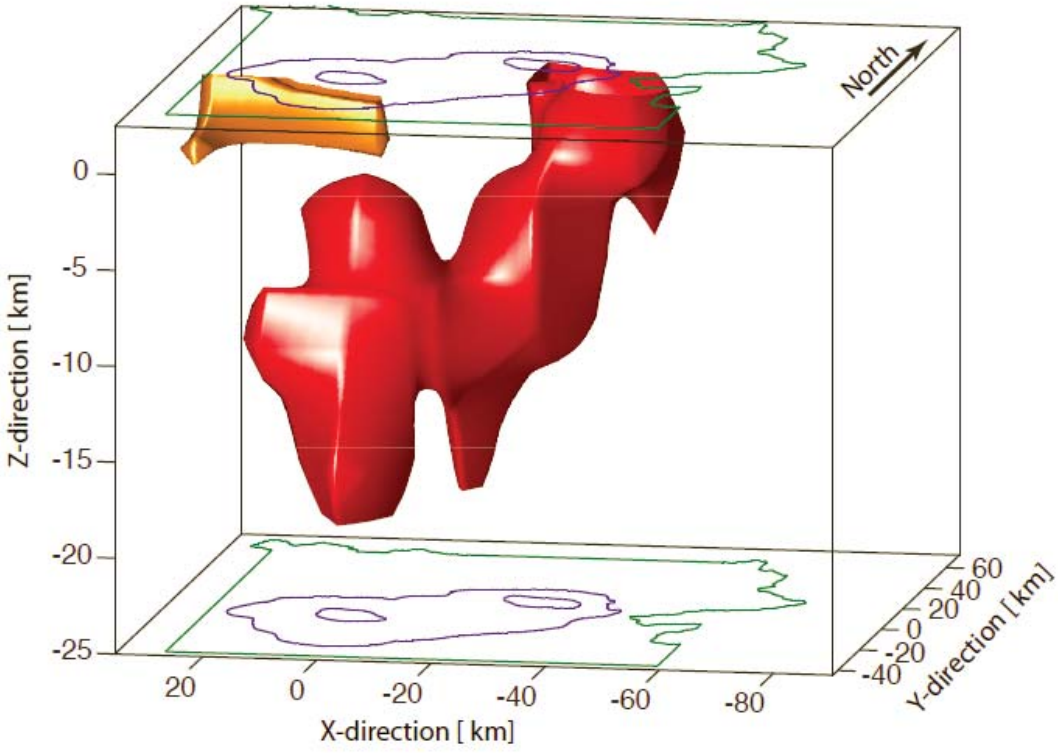

Figure 6.3: P-wave velocity isosurface of the Yellowstone crustal magma reservoir (Farrell et al., 2014). The red surface is a -2% isosurface, while the orange surface represents a -6% isosurface and indicates the low V_p body that was previously interpreted as a CO_2 gas-saturated volume. Blue lines outline the 0.64 Ma Yellowstone caldera and the two resurgent domes.

6.2 Crustal deformation of the Yellowstone volcanic plateau

Precise vertical leveling of benchmarks estabilished in 1923 in conjunction with road construction provided the earliest ground motion measurements in Yellowstone: the benchmarks were surveyed again in 1975-77 (Pelton and Smith, 1982) leading to the discovery of uplift of the caldera by up to 75 cm (Pelton and Smith, 2002; Dzurisin and Yamashita, 1987). After this new discovery, 15 permanent GPS stations were installed in Yellowstone, in the Eastern Snake River Plain and surrounding areas for the Yellowstone Geodynamics project beginning in 1996. GPS data from about 160 stations, supported by the UNAVCO, a non-profit university-governed consortium that facilitates geoscience research and education using geodesy, were acquired in many surveys throughout the years. GPS velocities were determined by calculating changes in station coordinates over time and were constrained to a North America fixed reference frame (Bennett et al., 2001), where it is assumed that no deformation happens in the U.S. continental interior, east of the Rocky Mountains.

The InSAR and GPS data sets are found to be both in qualitative and quantitative agreement: they are complementary data sets, each important

in its own regard. GPS observations provide estimates of the horizontal components of displacement which are helpful to constrain the geometry of subsurface volume change, while InSAR data (Interferometric Synthetic Aperture Radar) provide dense spatial sampling of the projection of the displacement components into the vector pointing from the sample points on the Earth's surface to the satellite (Vasco et al., 2007).

These measurements have revealed multiple episodes of caldera uplift and subsidence, with maximum average rates of about 1 to 2 cm/yr, generally centered at its two resurgent domes. These spatial and temporal variations of ground deformation are correlated with changes in seismic and hydrothermal activity (Smith et al., 2009).

The GPS derived velocities were partitioned into multiple time windows to determine temporal changes in deformation of the Yellowstone plateau: 1987-1995, 1995-2000, 2000-2003, 2004-2007. The first three time periods showed remarkable deformation changes in horizontal and vertical components, with alternating subsidence and uplift of the caldera at up to 2 cm/yr, uplift northwest of the caldera, and regional extension of 2 to 4 mm/yr across the Hebgen Lake fault zone (Wicks et al., 1998; Puskas et al.,

2007). Regional extension with respect to the stable North America was indicated by the stations southwest of the caldera moving southwest during the observing periods. Starting from mid-2004, GPS and InSAR measurements showed an episode of caldera uplift at very high rates up to 7 cm/yr, three times greater than every uplift episode observed in the previous deformation episodes (Chang et al., 2010).

The eastern Snake River Plain, adjacent to Yellowstone, moved southwest at 2.4 ± 0.4 mm/yr from 1995 to 2000, in contrast with the westward extension of the eastern Basin and Range province and it is part of a larger pattern of clockwise rotation in the direction of deformation of the western U.S. (Puskas et al.,2007).

Episodes of uplift and subsidence in the caldera have been attributed to combinations of two processes taking place beneath the caldera: pressurization and de-pressurization of an alternately self-sealed and leaking hydrothermal fluid reservoir that traps volatiles exsolved from a

crystallizing rhyolitic magma; or movement, formation and crystallization of rhyolitic or basaltic magma (Wicks et al., 2006).

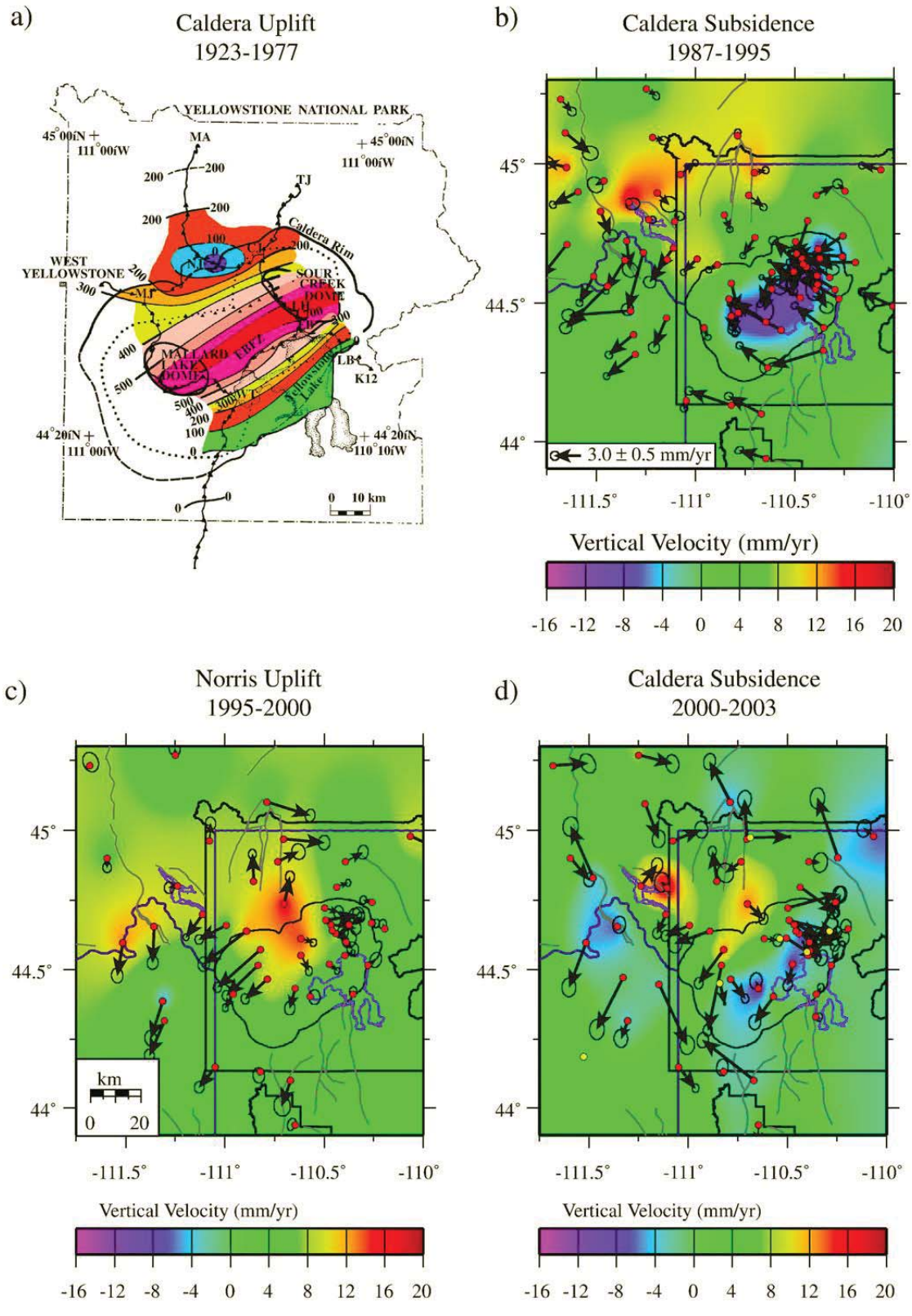
a)
Caldera Uplift
1923-1977
YELLOWSTONE NATIONAL PARK
45°00'N
111°00'W
MA
TJ
Caldera Rim
WEST YELLOWSTONE
MF
SOUR CREEK DOME
LH
MALLARD LAKE DOME
LBFZ
NNBFZ
Yellowstone Lake
LB
K12
44°20'N
110°10'W
0 10 km
b)
Caldera Subsidence
1987-1995
3.0 ± 0.5 mm/yr
-111.5°
-111°
-110.5°
-110°
45°
44.5°
44°
Vertical Velocity (mm/yr)
-16 -12 -8 -4 0 4 8 12 16 20
c)
Norris Uplift
1995-2000
km
0 20
d)
Caldera Subsidence
2000-2003

Figure 6.4: Crustal deformation of the Yellowstone Plateau from leveling and GPS observations. Color backgrounds represent vertical motion, in mm, measured from (a) leveling surveys between 1923 and 1987 (mm) and (b)-(d) GPS campaigns between 1987 and 2003. Red circles represent campaign GPS sites, yellow circles represent permanent GPS stations and arrows are the direction of motion relative to the stable North America. Time windows correspond to the distinct periods of caldera uplift and subsidence (Smith et al., 2009).

The configuration and depths of the sources responsible for deformation of the Yellowstone caldera were determined using volumetric strain modeling. Surface motions, measured by leveling surveys between 1987 and 1993 and InSAR between 1992 and 2002, were combined with GPS data. The modeled volumetric decrease in the period of time between 1992 and 1995 occurred along the caldera axis, between the two resurgent domes at ~6 to 10 km depth (Vasco et al.,2007), with a deflation rate of 8.7×10^{-3} km^3/yr. The caldera uplift stage between 1996 and 2000 was modeled by volume increase below the northwest caldera boundary of 4.6×10^{-3} km^3/yr at ~6 to 10 km depth. Additional models from 2000-2001 and 2001-2002 employed InSAR data to image a volumetric decrease along the Yellowstone caldera axis at depths of ~6-8 km with uplift along the north caldera boundary at ~4 to 6 km deep for 2000-2001 and ~2-4 km deep for 2001-2002. The deeper parts of the volumetric source volumes overlap with the top of the seismically imaged magma reservoir (Husen et al., 2004): the subsidence source originated within the upper part of the magma reservoir.

The Yellowstone caldera began a rapid episode of ground uplift in mid-2004, at rates up to 7 centimeters per year at the Sour Creek dome, while

three months later the Norris area began to subside at a rate of about 3 cm/yr, more than two times greater than the 1996-2002 uplift rate in this area. The inflation increases symmetrically toward the caldera center. The GPS horizontal velocities indicate ground motions directed outward from the caldera at 0.8 to 2.2 cm/year and inward to the Norris area at 0.7 to 2.0 cm/yr (Chang et al., 2007).

Source modeling of the 2004 accelerated uplift (Chang et al., 2007) suggests a near-horizontal expanding sill-like magma body, dipping 5°SE over an area 40 x 60 km^2 at a depth of ~9 km beneath the caldera and a contracting volume dipping 12°SE at a depth of ~8 km under the Norris area. The estimated rate of volumetric expansion of about 0.1 km^3/yr for this uplift episode is similar to the magma intrusion rate required to supply the high heat flow of about 2000 mW/m^2 of Yellowstone (Fournier, 1989).

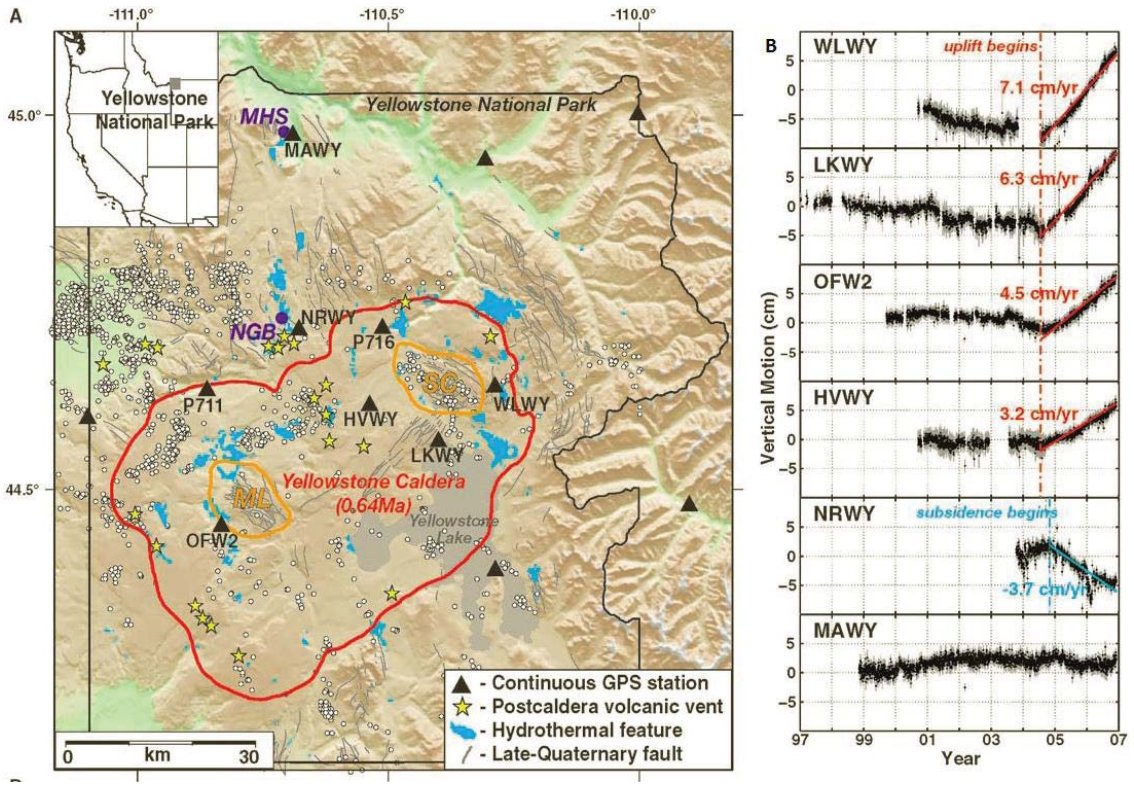

Figure 6.5: (A) Volcano tectonic setting and GPS station locations of the Yellowstone volcanic field. White circles are earthquake epicenters from October 2004 to March 2007, considered in this study. SC=Sour Creek dome; ML=Mallard Lake resurgent dome; NGB=Norris Geyser Basin; MHS=Mammoth Hot Springs. (B) Temporal variation of vertical ground motions of labeled Yellowstone GPS stations. Each dot is a daily position determination. Red and blue lines mark the inceptions of the uplift and the subsidence, respectively. The slopes of the interpolated lines represent the deformation rates (Chang et al., 2007).

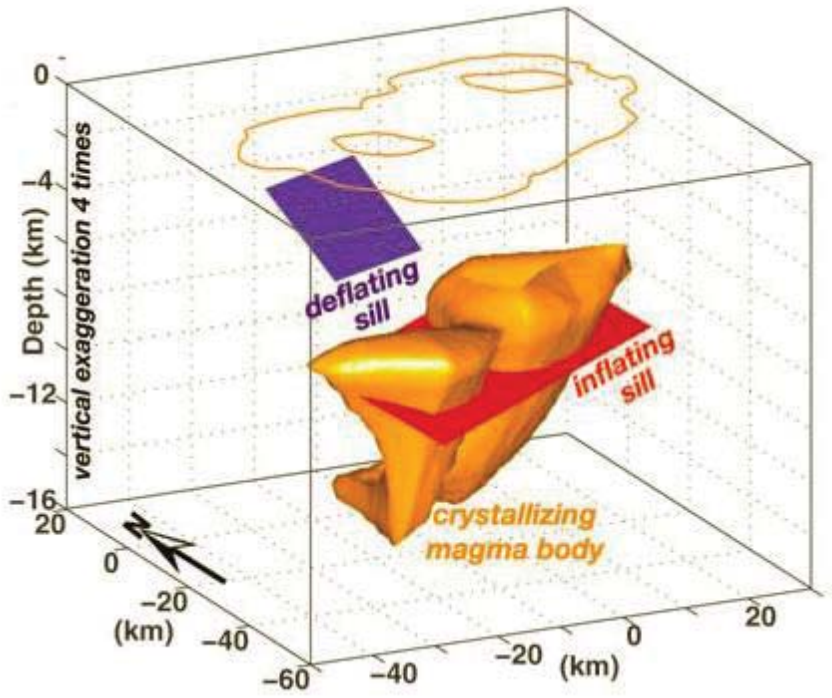

Figure 6.6: Three dimensional view from the southwest of the modeled volcanic sills superimposed on a seismically images magma body (Chang et al., 2007).

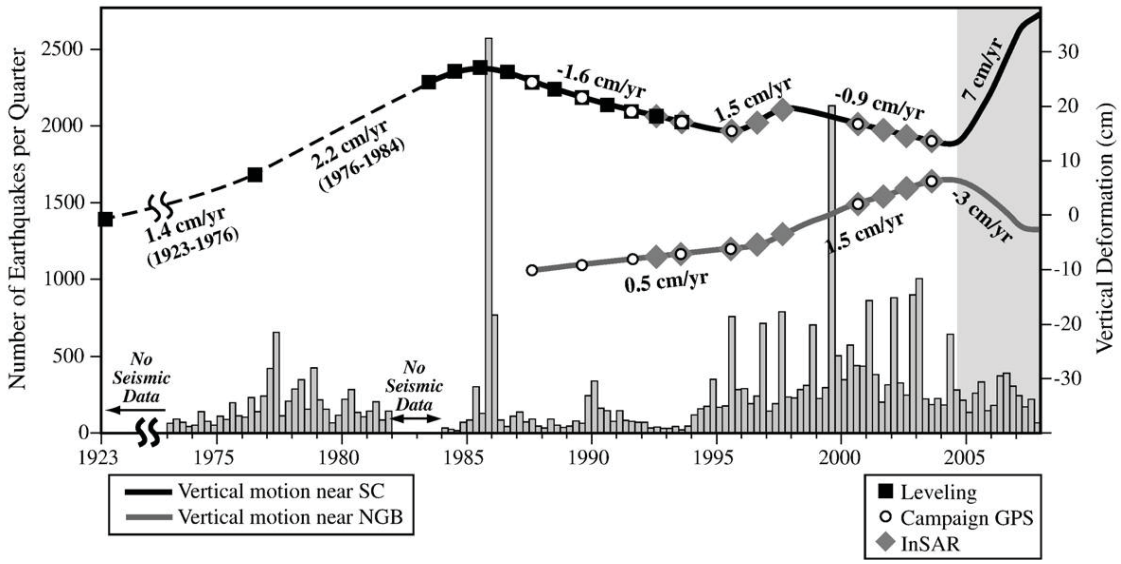

Figure 6.7: Correlation between seismic activity in Yellowstone caldera and temporal history of deformation. Specific leveling and GPS surveys are shown as black squares and white circles. SC=Sour Creek dome, NGB=Norris Geyser basin (Chang et al., 2007).

The episodes of uplift and subsidence from 1973 to 2006 can be correlated to Yellowstone earthquake occurrence, as shown in figure 6.7, where the temporal history of deformation of the Sour Creek dome area and the Norris Geyser Basin area is described (Chang et al., 2007).

The change from uplift to subsidence in 1984-1985 seems to coincide with Yellowstone's largest earthquake swarm which happened in fall 1985. In

2002, Waite and Smith interpreted the seismicity migration rate and the stress directions arguing that the 1985 swarm seismicity was related to magmatic or hydrothermal fluid flow that originated beneath the Mallard Lake resurgent dome: the transport of fluids was towards the northwest, causing earthquakes once it reached the brittle crust (Waite and Smith, 2002). After the 1985 caldera reversal, subsidence continued until 1995, when the caldera began a 5-year period of minor uplift followed by renewed subsidence until the sudden change to accelerated caldera uplift. From the beginning of the 1995 uplift, seismicity started to increase until the onset of accelerated uplift in late 2004 (Chang et al., 2007).

The area interested by uplift in the 1990s is located under the north caldera rim near Norris Geyser Basin, so that area was renamed NUA (north rim uplift anomaly). As NUA continued to rise after 1995, vertical motion of the caldera floor connecting the Sour Creek resurgent dome and the Mallard Lake resurgent dome changed from uplift to subsidence between late 1997 and early 1998. NUA continued to inflate as the caldera floor subsided until 2002 at which time both movements ceased, or at least paused. In order to model a deformation source for the entire inflation episode at NUA, the

four interferograms were summed: the total amount of volume added by the modeled inflating sill beneath NUA was calculated to be 0.06-0.1 km^3 (Wicks et al., 2006).

Measurements of the chloride flux, which is one of the volatile species that is usually exsolved from rhyolitic magma during crystallization, did not show any obvious temporal change that might have been related to changes in deformation style leading to the idea that, in this particular case, the deformation had been caused by a magmatic source, instead of considering the hydrothermal activity as a source. All the evidences showed that the uplift at NUA and the subsidence of the caldera floor were linked: increases in the rate of basaltic magma flux out of the caldera near Norris Geyser Basin favour subsidence of the caldera, whereas decreases favor inflation (Wicks et al., 2006). The combination of extensional stress and high heat flow in Yellowstone, which is at the northeastern corner of the Basin and Range extension, should favour the emplacement of magma. The beginning of the caldera uplift in 1995 was interpreted to be due to the introduction of basaltic magma below SC from a source in the upper mantle: as the magma spread horizontally, the uplift began to get wider

across the entire caldera, including the area of NUA. The flux of magma out of the Yellowstone system was then controlled by extra-caldera tectonic activity acting on fractured rock bordering the northern caldera boundary (Wicks et al., 2006).

The shallower southeastern end of the dipping sill that was interpreted to model the inflation at NUA is at the same depth as two deflating sills it intersects beneath the caldera floor. This dipping sill deepens to the north-northwest by about 7 km, forming a trap for the negatively buoyant magma (Wicks et al., 2006).

The main mechanism proposed to explain the previous Yellowstone caldera uplift stages is the episodic intrusion or recharge of magma into the upper crust. In this conceptual model, a mantle plume located at depths of about 50 km originates basaltic magma, which ascends buoyantly through the crust, providing thermal energy to partially melt crustal rocks and create the rhyolitic magma component which is a characteristic of a silicic volcanism (Chang et al., 2007). The crystallizing and cooling of those basaltic and rhyolitic magmas releases the energy responsible for the

extraordinarily high heat flow of ~2000 mW/m^2 of Yellowstone, measured from Yellowstone Lake and geochemical evidence. Anomalies of low P-wave velocity, up to 6%, at depths of 8 to 16 km were interpreted as a 4,000 km^2 body of crystallized magma underlying the caldera: the top of this body and the sill overlap, implying that the accelerated uplift occurred in response to a caldera-wide magma recharge of the Yellowstone volcanic system (Chang et al., 2007).

An alternate interpretation for the caldera uplift stages in general is that magmatic fluids created by the magma crystallization were trapped beneath impermeable rocks, such as the brittle-ductile transition zone or a stratigraphic boundary, leading to increased pore pressure, volumetric increase, pressurization of the deep hydrothermal system and inflation of the ground surface. Crystallizing 0.1 km^3/yr of rhyolitic magma, which is required to provide the thermal heat flow, and trapping all the released water would cause a volumetric expansion of about 0.013 km^3/yr, which is 10 times smaller than the source inflation rate of 0.11 km^3/yr which seems to be responsible of this uplift episode in particular (Chang et al., 2007). Magma intrusion and fluid pressurization should be considered both as

operating processes to explain the 2004 accelerated caldera uplift. The subsidence in the Norris area is proposed to have been caused by the depressurization of the Norris hydrothermal systems, due to an induced pressure gradient that drove fluids southeastward into the caldera (Chang et al., 2007). This pressure gradient is caused by an increase in permeability and a decrease in pore pressure by opening new or self-sealed fractures, because the inflation of the magmatic sill can induce dilatational strain in the surrounding volcanic rocks.

Volumetric expansion of crustal rocks due to the induced dilatation can increase the strain rate and make possible a brittle fracturing: earthquake activity during this period was concentrated near the northern caldera boundary, while the rest of the caldera experienced low rates of seismicity (Chang et al., 2007).

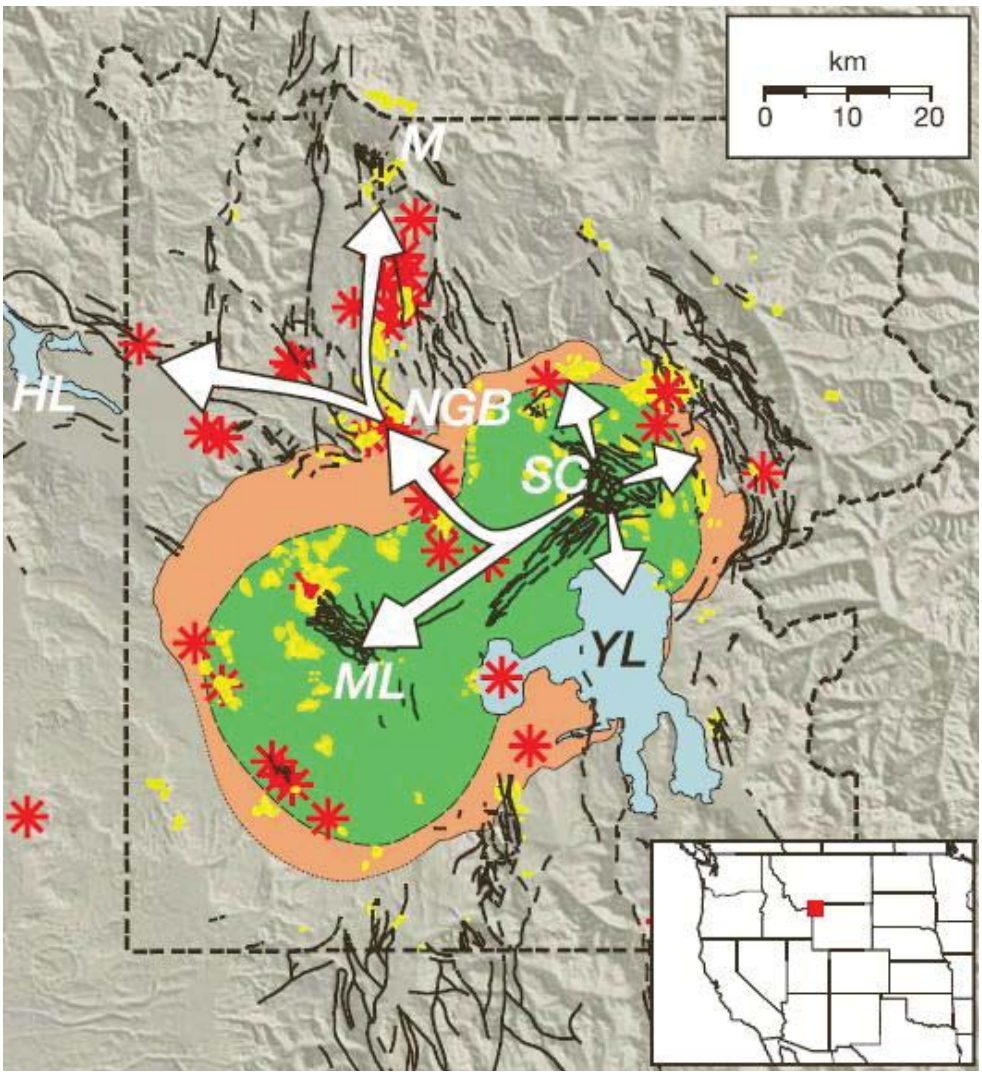

Figure 6.8: Map of structural, thermal and volcanic features in and around Yellowstone caldera (Christiansen, 2001). The red symbols mark volcanic centres that erupted after the 0.64 Ma eruption. The areas coloured in yellow are zones of known past or present thermal activity. The ring-fracture zone of the caldera is outlined in green. The park boundary is the dashed black line. Faults active in the Quaternary are marked with black lines. NGB=Norris Geyser Basin, M=Mammoth Hot Springs, SC=Sour Creek dome, ML=Mallard Lake dome, HL=Hebgen Lake, YL=Yellowstone Lake. The white arrows show magma migration paths (Wicks et al., 2006).

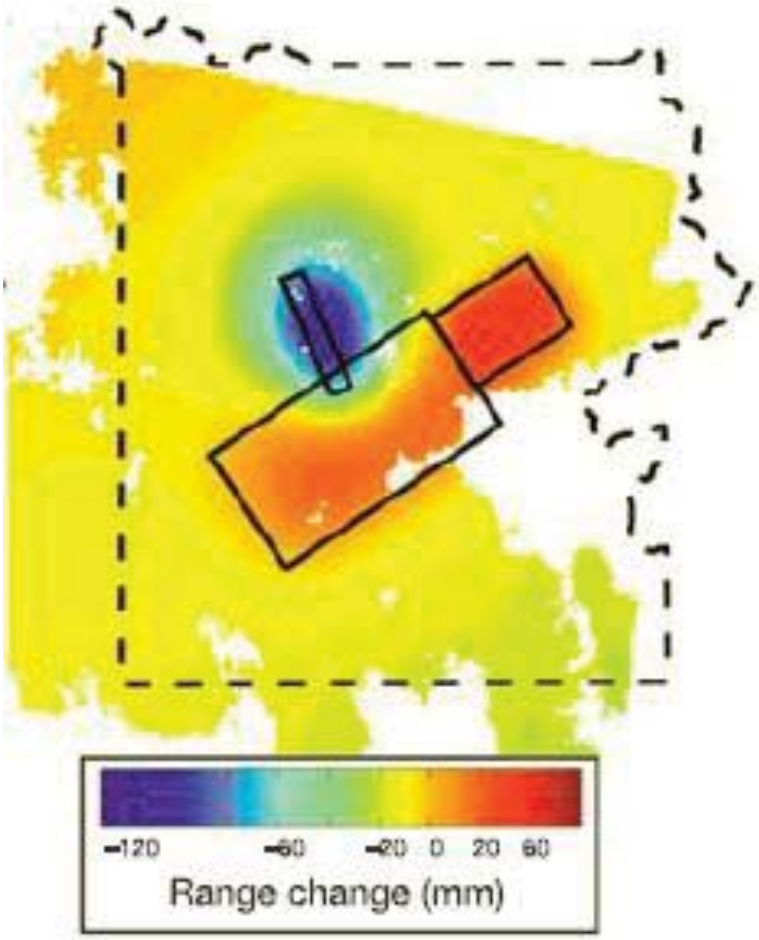

Figure 6.9: Synthetic interferogram from best-fit model (Wicks et al., 2006). The black outlines are the surface projections of a north-northwest-trending expanding sill, and two northeast-trending contracting sills. The dashed line is the outline of Yellowstone National Park.

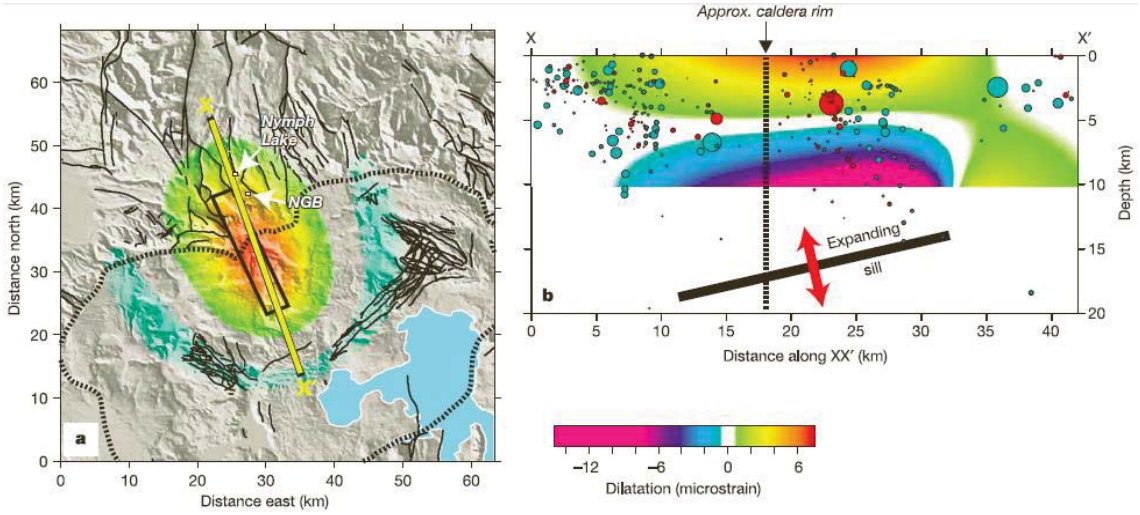

Figure 6.10: Dilatation calculated from the inflating sill in figure. (a) Dilatation at the surface resulting from the NUA uplift episode. The black lines are mapped faults active in the Quaternary. The black rectangle is the surface projection of the best-fit expanding sill. The broken line shows the location of the 0.64 Ma-year-old caldera rim. NGB=Norris Geyser Basin. (b) Cross-section through X-X'. The cyan circles are earthquakes that occurred before the uplift episode (1992 through 1997) and the red circles show earthquakes that occurred during the uplift episode (1997 through 2003). The size of circles is scaled to earthquake magnitude (Wicks et al., 2006).

CHAPTER 7

SPATIAL AND TEMPORAL VARIATIONS IN SEISMICITY

7.1 Evaluation of the evolving stress field in the Norris Geyser Basin area: results and discussion

As shown in figure 6.7, the Norris Geyser Basin Area experienced a period of uplift up to 2004, at the initial rate of 0.5 cm/yr which accelerated since 1997 reaching 1.5 cm/yr, followed by subsidence at a rate of 3 cm/yr (Chang et al., 2007). In the study by Wicks et al. (2006), the uplift stage in Norris Geyser Basin area, which corresponds to NUA (North rim Uplift Anomaly), was interpreted to be caused by a north-northwest-trending inflating sill (figures 6.9 and 6.10), while the subsidence stage in the study by Chang et al. (2007) is believed to be due to a 12° SE dipping contracting volume at a depth of ~5 to 8 km, as it is shown in figure 6.6.

The data considered in this study contain enough events to allow for study of both the subsidence and the uplift stages. As a first step, we defined temporal windows of different length in order to find correlations between time and changes in the orientations of P and T axes of focal mechanism

solutions and, in general, in the deformation pattern of the Norris Geyser Basin area.

The entire period of time covered by the database used in this study, from 1988 to 2010, was divided into two temporal windows: the first lasting from 1988 until 2004 corresponded to the uplift stage, while the second temporal window, from 2004 to 2010, corresponded to the entire subsidence stage documented in the area. We examined the focal mechanism solutions throughout the Norris Geyser Basin area and the P and T axes orientations inside each temporal window, expecting to find vertical-sub-vertical P axes and horizontal-sub-horizontal T axes associated with the extension and subsidence stage (2004-2010) and horizontal-sub-horizontal P axes associated with vertical-sub-vertical T axes during the compression and uplift stage (1988-2004). Instead, the P and T axes revealed a strong heterogeneity: examining one temporal window at the time, the compressive stress axes are distributed from vertical to horizontal angles all over the Norris Geyser Basin area and the focal mechanism solutions, which are predominantly strike-slip and dip-slip normal faulting

mechanisms, are equally distributed both in the uplift and the subsidence stage (plots with P and T axes are shown in Appendix A and B).

Since the first stage lasted 16 years and the second stage lasted 6 years, the next step was to subdivide each temporal window in two-years intervals in order to investigate whether it was possible to detect a gradual change in the deformation pattern throughout the years.

The uplift stage was divided into three smaller time windows: 1996-1998, 2000-2002, 2002-2004, each one with 6, 7 and 25 events, respectively. The time period between 1988 and 1996 is not considered because it contains only one event and the analysis could not have been statistically relevant. The time period between 1998 and 2000 does not contain any event.

The subsidence stage (2004-2010) was divided into three smaller time windows as well: 2004-2006, 2006-2008, 2008-2010. These temporal windows contain 15, 12 and 24 events, respectively.

7.1.1 Changes in the deformation pattern in Norris Geyser Basin area during uplift stage (1988-2004)

In the time interval between 1996 and 1998, two earthquakes with nearly N-S normal faulting occurred inside the 0.64 Ma Yellowstone caldera, while, north of the caldera, the focal mechanisms indicate the presence of a NNW-SSE dip-slip normal faults and oblique strike-slip (figure 7.2). Since 2000, while the movement along normal faults with NNW-SSE to NNE-SSW direction continues, perpendicular ENE-WSW normal faults have also been active inside the Yellowstone caldera (figure 7.3). This is particularly evident in the time interval between 2002 and 2004 (figure 7.4), when a ENE-WSW fault and a NNE-SSW to NNW-SSE fault intersect inside the caldera, generating a "chocolate tablet" structure, which is composed by a double set of orthogonal dilational fractures, due to a change between σ_2 and σ_3. The chocolate tablet boudinage is a structure with crossing boudin neck zones, rarely regularly developed or mutually perpendicular; arising from the superposition of different deformations or different phases within one overall deformation, these structures often show periodic or sequential

development, and the boudins often intersect at angles other than 90° (Ramsay and Huber, 1983).

The “chocolate tablet” structures have been detected in other areas, such as on the Red Mountain Creek pluton, eastern Sierra Nevada, California, USA (Zak and Paterson, 2006), in Carboniferous turbidites in SW Portugal (Reber et al., 2010) or on the Piedmont accretionary wedge, western Alps (Schwartz et al., 2009). The Interpretation of the formation of these structures is shown in figure 7.1.

Outside the caldera, most of the deformation is shown by NNE-SSW to NNW-SSE dip-slip normal faults, together with strike-slip faults.

It is interesting to note that, in all the temporal windows examined so far in this study, most of the strike-slip faults are located at the northern margins of the area.

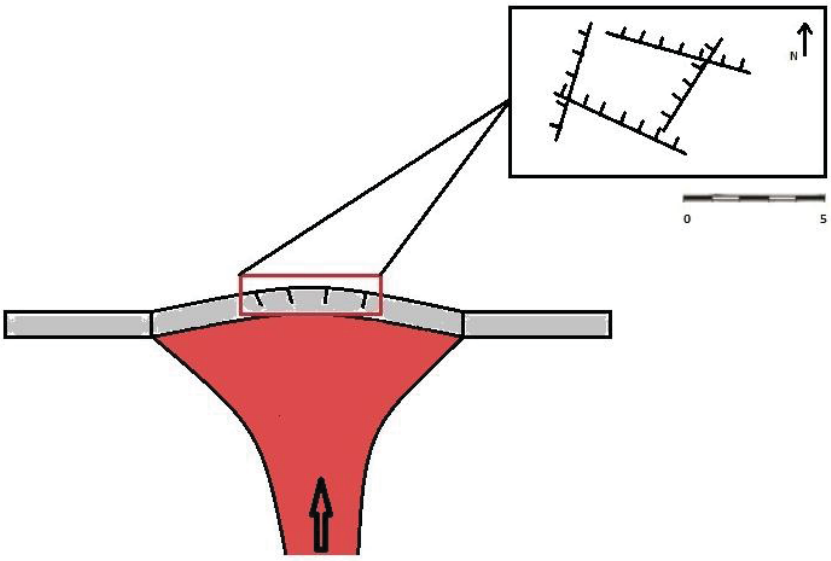

Figure 7.1: Magma movement towards the surface causes uplift and formation of “chocolate tablet” structures.

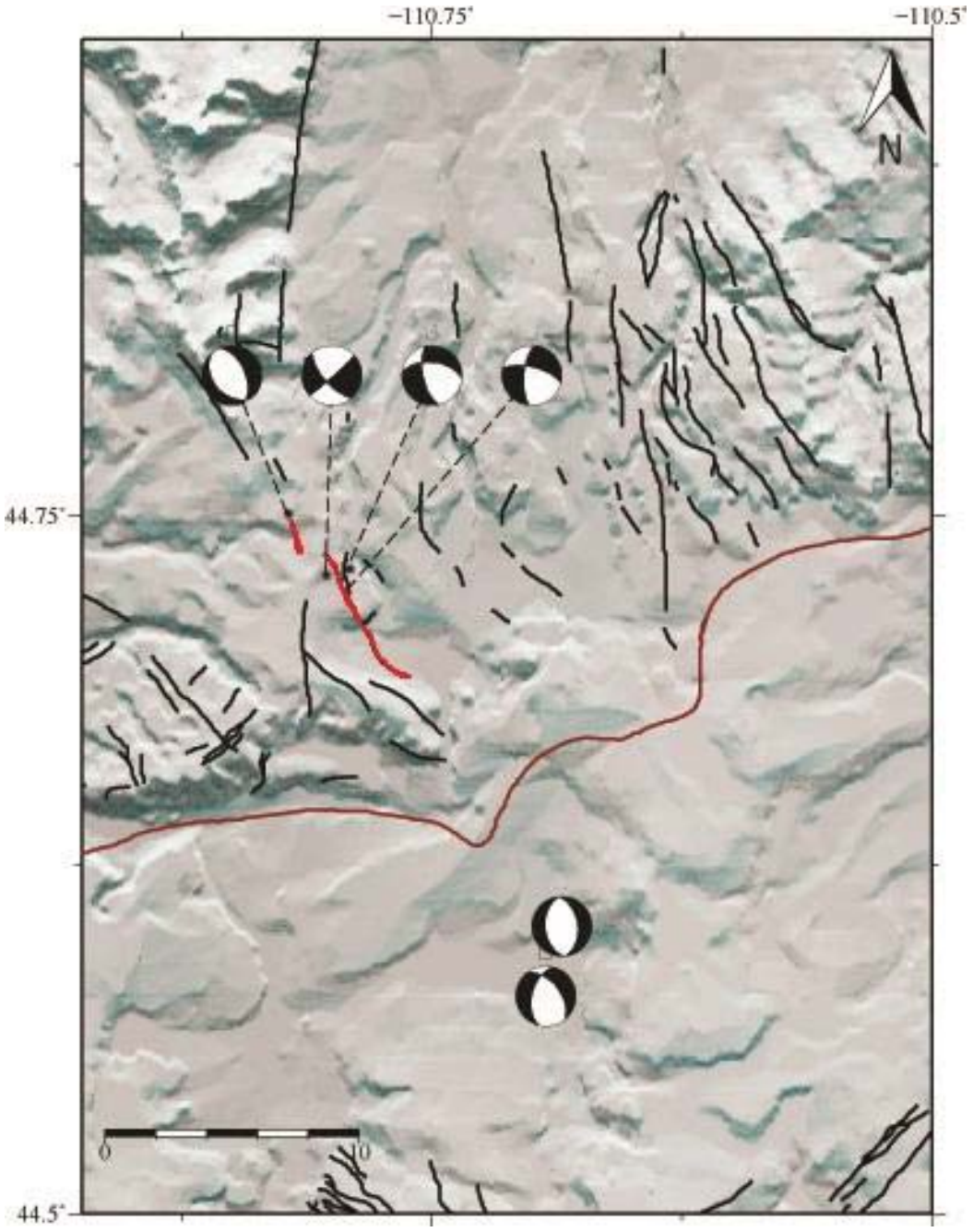

Figure 7.2: Map of selected focal mechanisms in Norris Geyser Basin area, from 1996 to 1998 (uplift stage). Quaternary faults are shown as black lines, reactivated Quaternary faults are shown as red lines. The topographic data is provided by the USGS National Elevation Dataset.

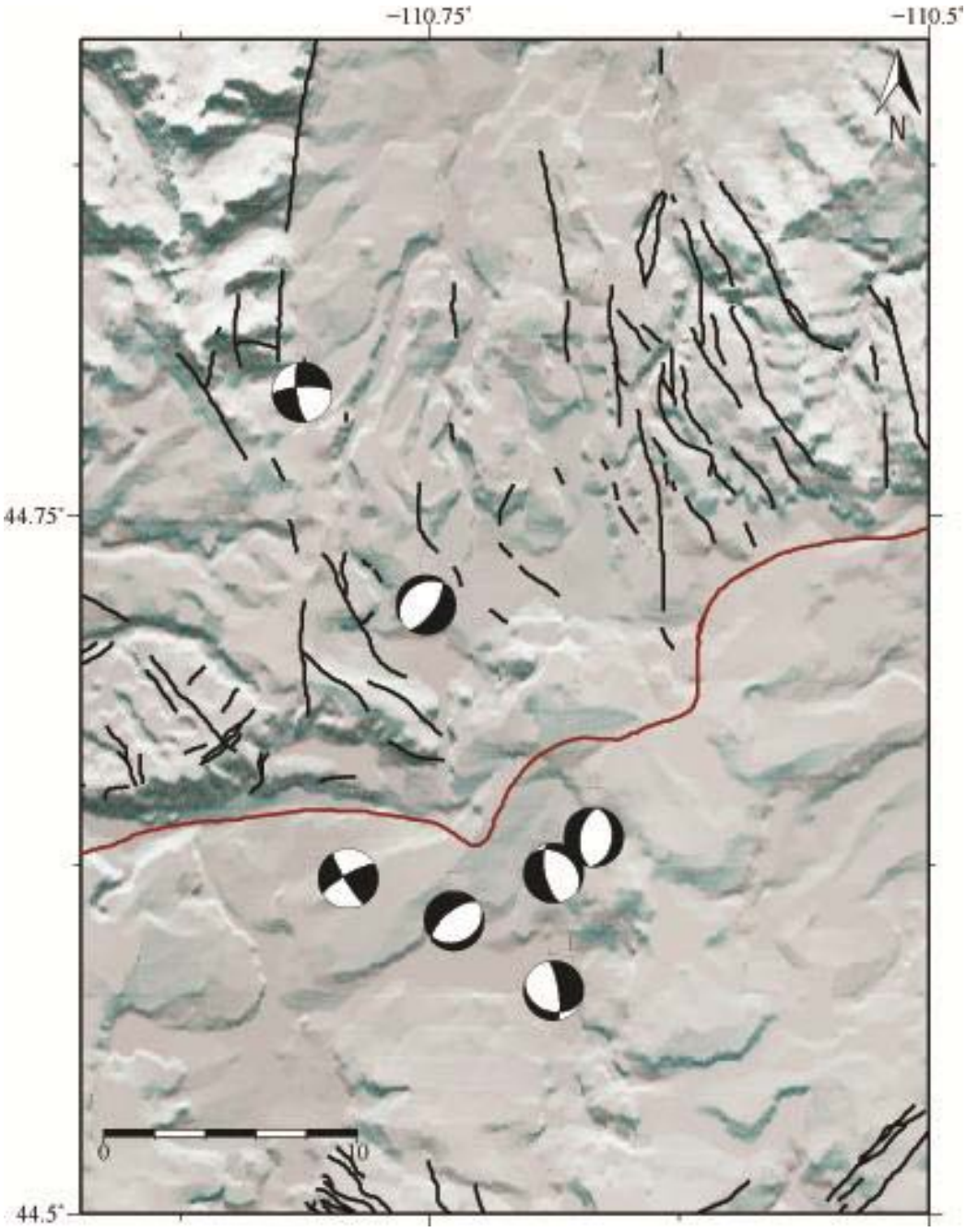

Figure 7.3: Map of selected focal mechanisms in Norris Geyser Basin area, from 2000 to 2002 (uplift stage). Quaternary faults are shown as black lines. The topographic data is provided by the USGS National Elevation Dataset.

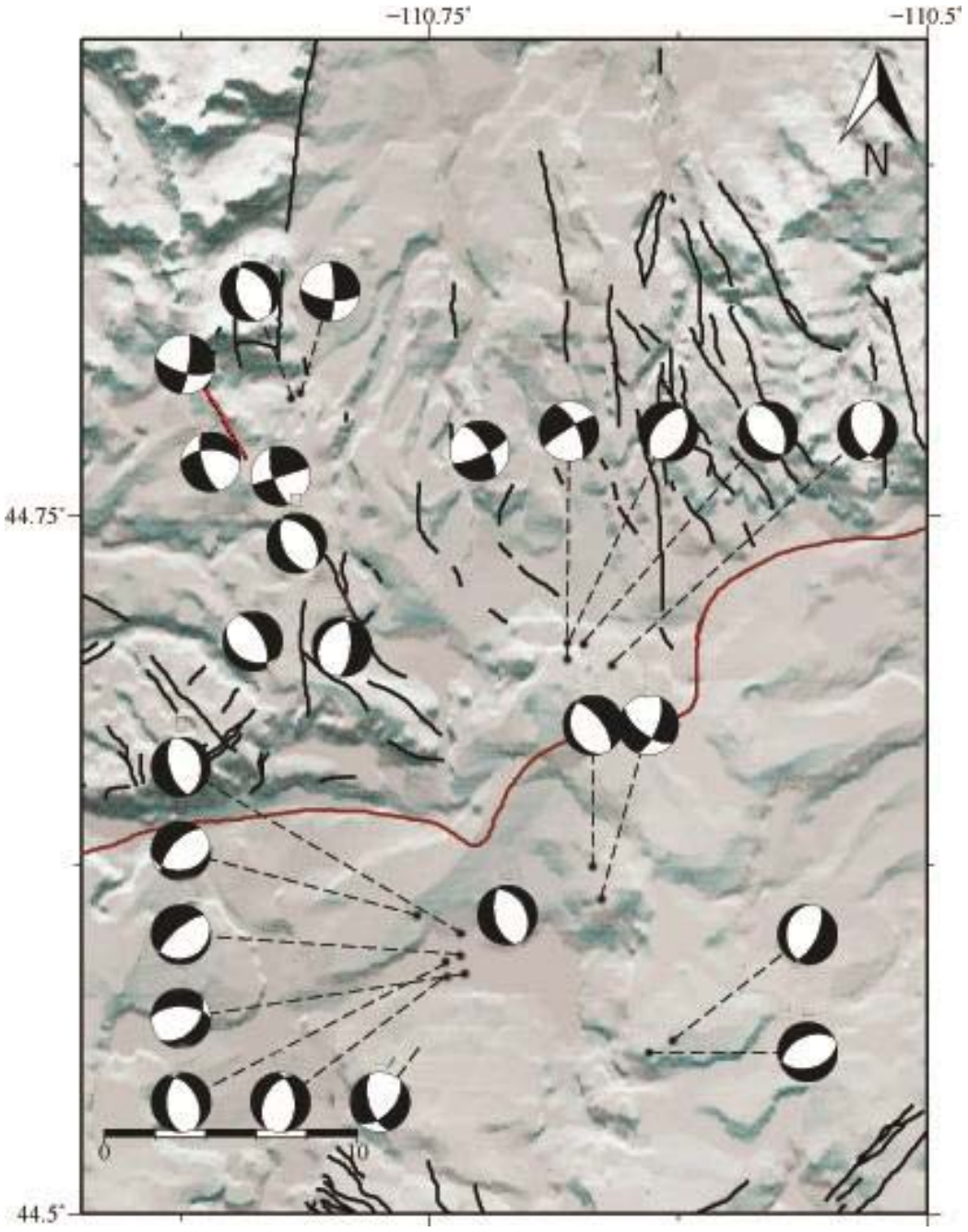

Figure 7.4: Map of selected focal mechanisms in Norris Geyser Basin area, from 2002 to 2004 (uplift stage). Quaternary faults are shown as black lines, reactivated Quaternary faults are shown as red lines. The topographic data is provided by the USGS National Elevation Dataset.

7.1.2 Changes in the deformation pattern in Norris Geyser Basin area during subsidence stage (2004-2010)

The first temporal window, between 2004 and 2006, which represents the beginning of the subsidence stage, shows that, as with the beginning of the uplift stage, the deformation inside the 0.64 Ma Yellowstone caldera coincides with slip along nearly N-S dip-slip normal faults. Most of the strike-slip faults are concentrated outside the caldera (figure 7.5).

In the second temporal window, from 2006 to 2008, most of the deformation occurs inside rather than outside the caldera, where both NNE-SSW to NNW-SSE normal faults and ENE-WSW normal faults, forming another “chocolate tablet” structure, move together with strike-slip faults that are mostly located at the southern margins of the area (figure 7.6).

The deformation described by figure 7.7 in the period of time between 2008 and 2010 is mostly concentrated on strike-slip with some dip-slip movement faults, both outside and inside the Yellowstone caldera, where also few NNE-SSW faults and an ENE-WSW fault are present.

It is also interesting to note that from 2004 to 2008, the deformation is especially concentrated in latitudes greater than 44.750° and lower than 44.640°, while after 2008 the deformation includes all the Norris Geyser Basin area.

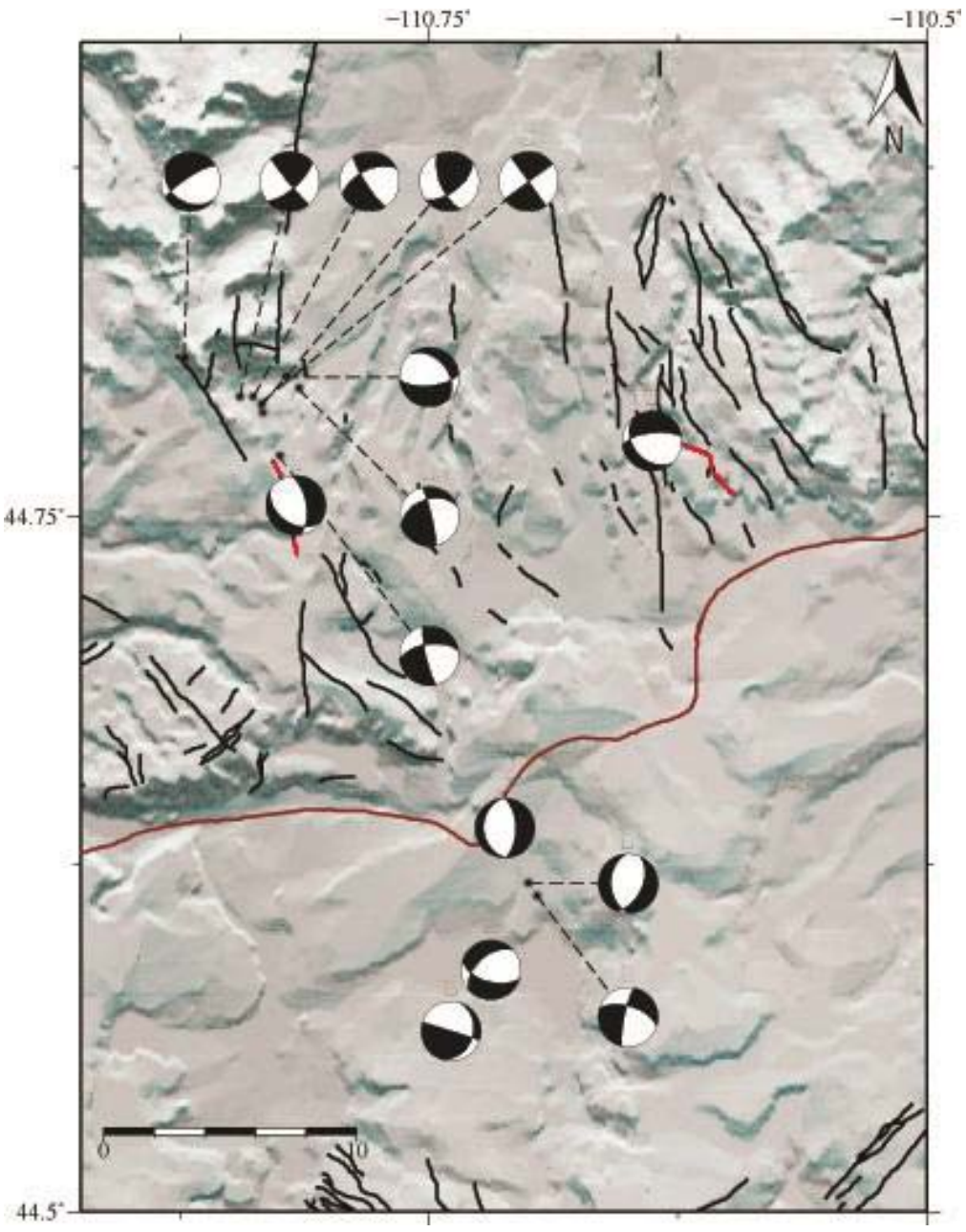

Figure 7.5: Map of selected focal mechanisms in Norris Geyser Basin area, from 2004 to 2006 (subsidence stage). Quaternary faults are shown as black lines, reactivated Quaternary faults are shown as red lines. The topographic data is provided by the USGS National Elevation Dataset.

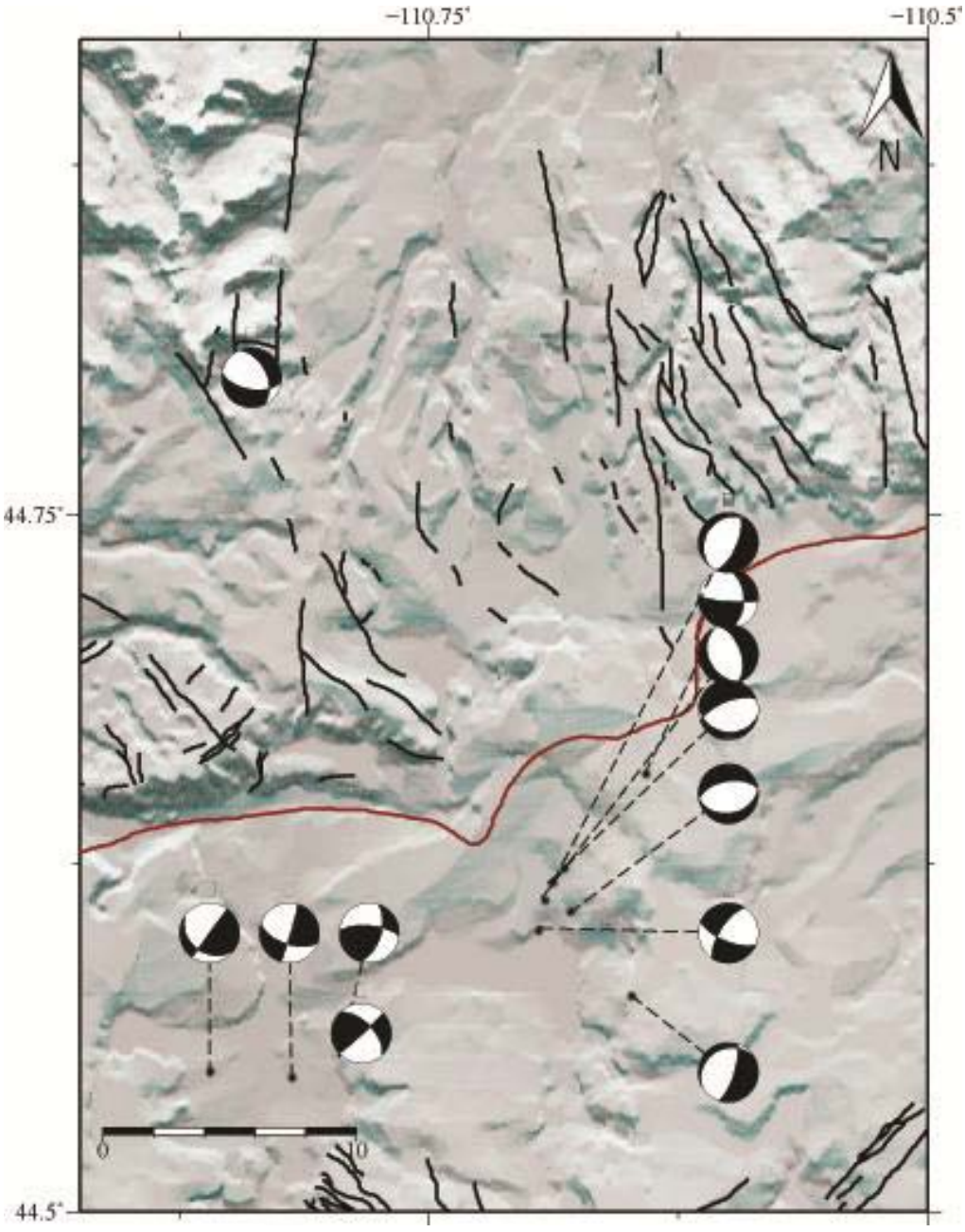

Figure 7.6: Map of selected focal mechanisms in Norris Geyser Basin area, from 2006 to 2008 (subsidence stage). Quaternary faults are shown as black lines. The topographic data is provided by the USGS National Elevation Dataset.

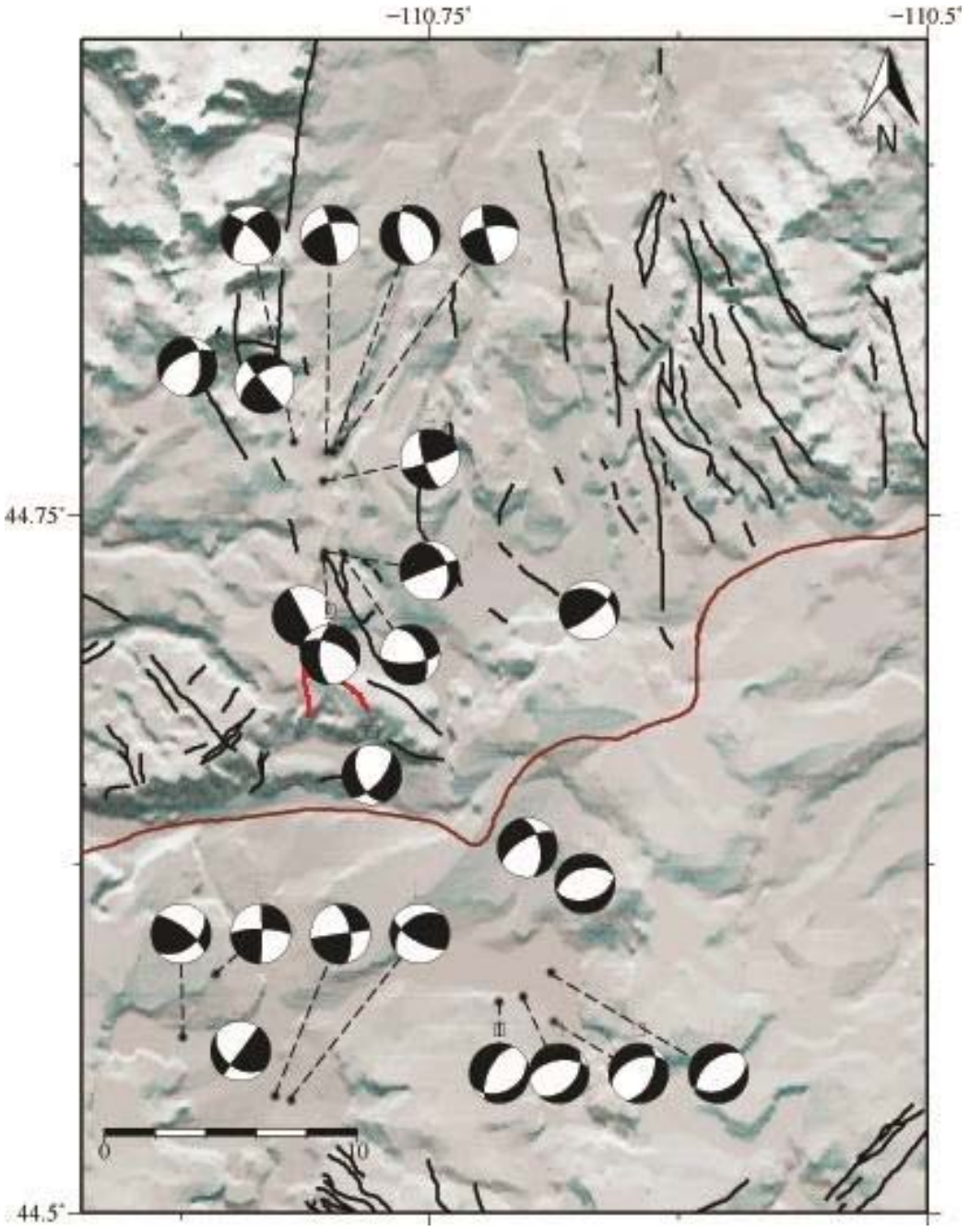

Figure 7.7: Map of selected focal mechanisms in Norris Geyser Basin area, from 2008 to 2010 (subsidence stage). Quaternary faults are shown as black lines, reactivated Quaternary faults are shown as red lines. The topographic data is provided by the USGS National Elevation Dataset.

7.1.3 Evaluation of the correlation between deformation and earthquake depth in the Norris Geyser Basin area (2004-2010)

In the study by Wicks et al. (2006), the uplift stage in Norris Geyser Basin area, which corresponds to NUA (North rim Uplift Anomaly), was interpreted to be caused by a north-northwest-trending inflating sill, at a depth between ~13 and 19 km, as shown in figures 6.9 and 6.10. All earthquakes during this period occurred above the proposed expanding sill.

In the study by Chang et al. (2007) the subsidence stage was thought to be caused by a 12° SE dipping contracting volume at a depth of ~5 to 8 km, as shown in figure 6.6. We selected the earthquakes that were located in the Norris Geyser Basin area that occurred during the subsidence stage (2004-2010) and dividing them into three depth windows: 0-5 km, 5-8 km, below 8 km.

The first depth window, from 0 to 5 km, represents the deformation above the contracting sill, which is represented by both strike-slip faults, especially outside the 0.64 Ma Yellowstone caldera, and dip-slip normal faults, with either ENE-WSW or NNE-SSW to NNW-SSE direction, forming a

“chocolate tablet” structure (figure 7.8). The interpretation of the deformation between 0 and 5 km depth in the area is shown in figure 7.11.

All the focal mechanisms inside the 0.64 Ma Yellowstone caldera in the second depth window, between 5 and 8 km, are located above the sill, while the focal mechanisms outside the caldera, in the northern part of the area, are located beneath the contracting sill: this happens because, since the contracting sill is dipping 12° SE, it reaches greater depths in the southern part of the area.

In this second depth window, above the contracting sill, the focal mechanisms show again both strike-slip and NNE-SSW dip-slip normal faults, while the deformation beneath the sill is mainly defined by strike-slip with some dip-slip focal mechanisms. This is shown both by the northern part of the area in the current depth window and by the focal mechanism solutions in third depth window (below 8 km) which represents the deformation beneath the contracting sill (figures 7.9 and 7.10).

This is unexpected because it would be more reasonable to think that below the sill there would be contraction and not dilatation together with

movement along strike-slip faults. The reason could be that the movement of magmatic fluids below the sill towards the 0.64 Ma Yellowstone caldera causes the deformation to be distributed along transfer faults.

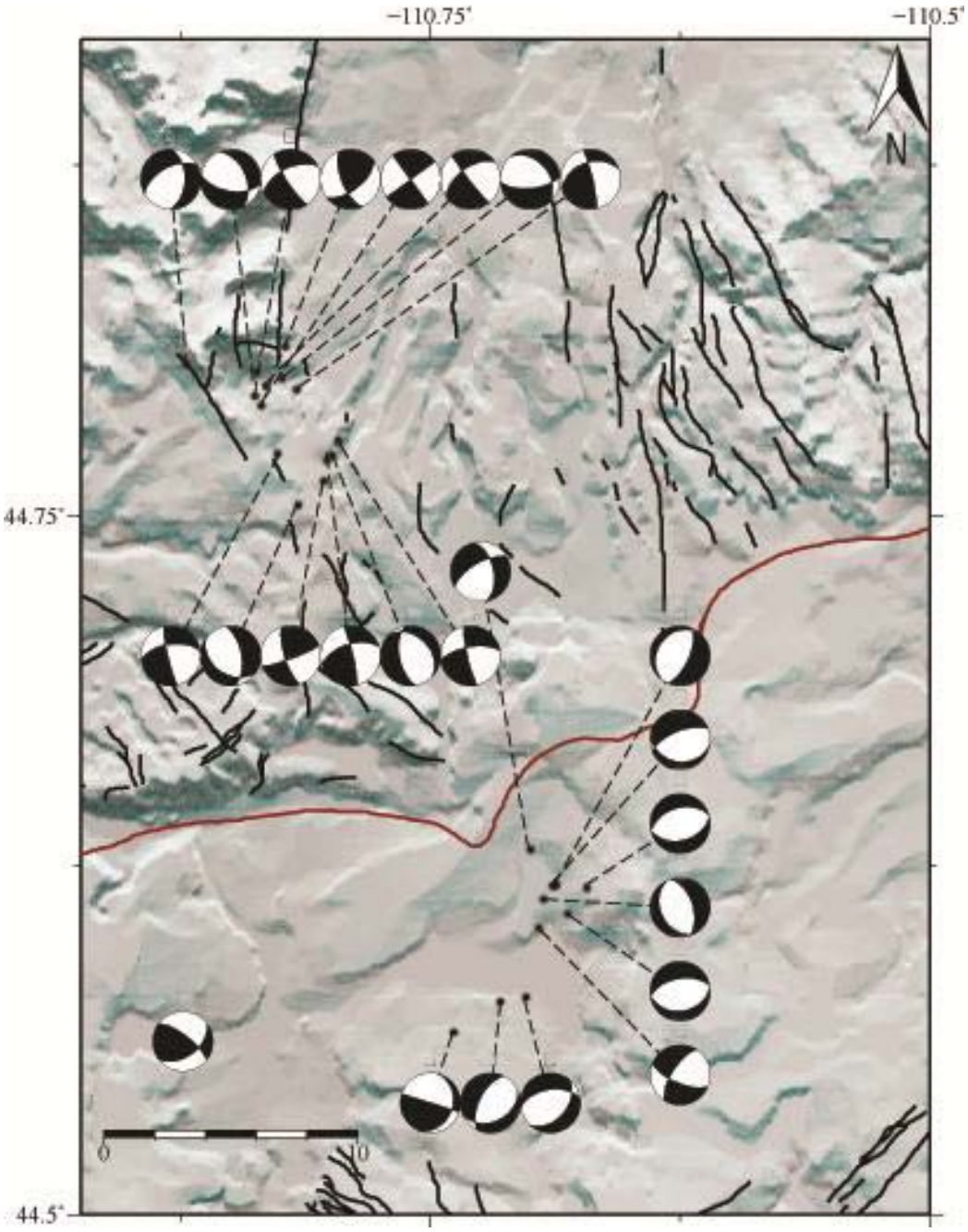

Figure 7.8: Map of selected focal mechanisms in Norris Geyser Basin area, from 0 to 5 km depth, above the proposed 12° SE dipping contracting sill, during the subsidence stage (2004-2010) (Chang et al., 2007). Quaternary faults are shown as black lines, reactivated Quaternary faults are shown as red lines. The topographic data is provided by the USGS National Elevation Dataset.

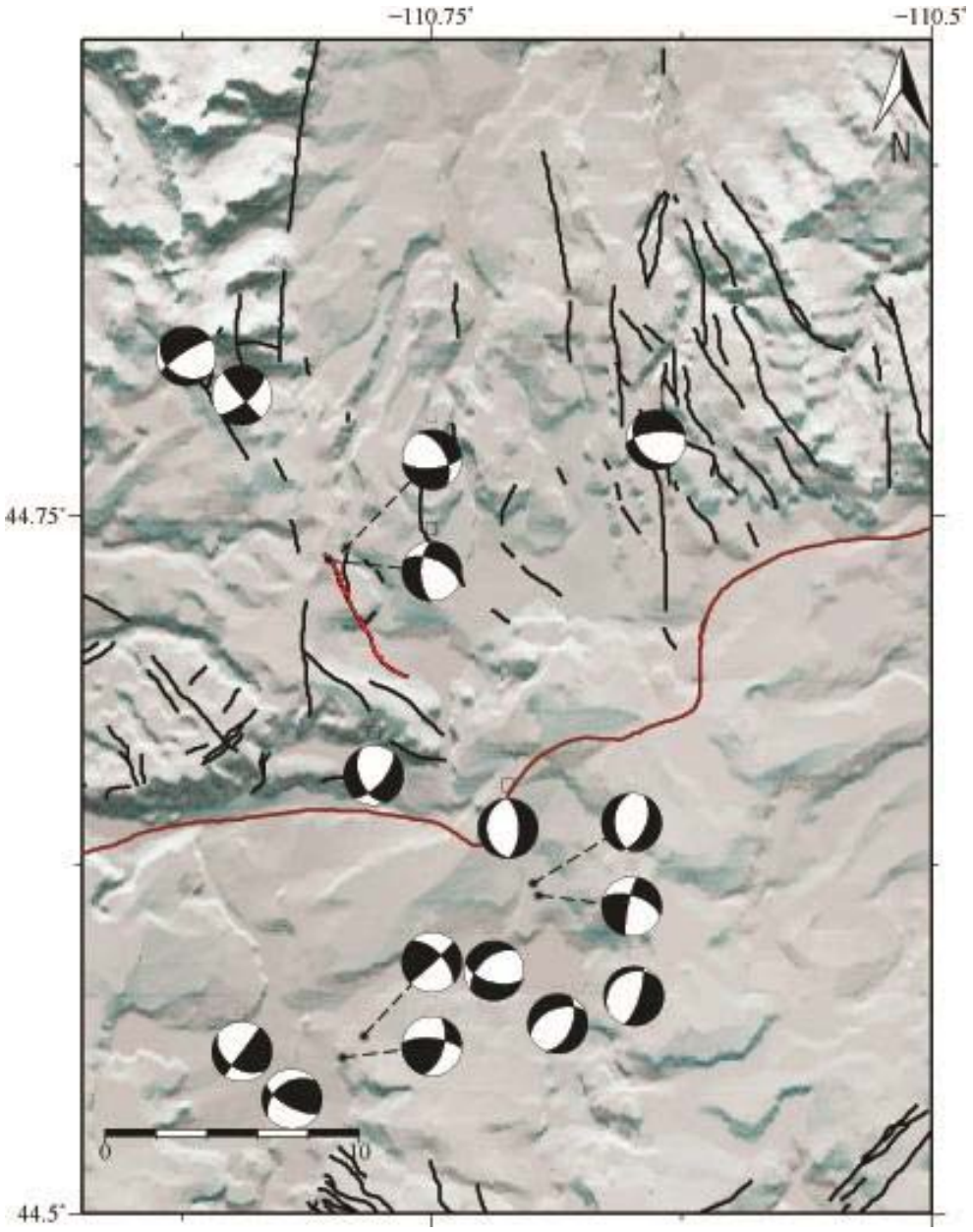

Figure 7.9: Map of selected focal mechanisms in Norris Geyser Basin area, from 5 to 8 km depth, above (inside the caldera) and below (outside the caldera) the supposed 12° SE dipping contracting sill, during the subsidence stage (2004-2010) (Chang et al., 2007). Quaternary faults are shown as black lines, reactivated Quaternary faults are shown as red lines. The topographic data is provided by the USGS National Elevation Dataset.

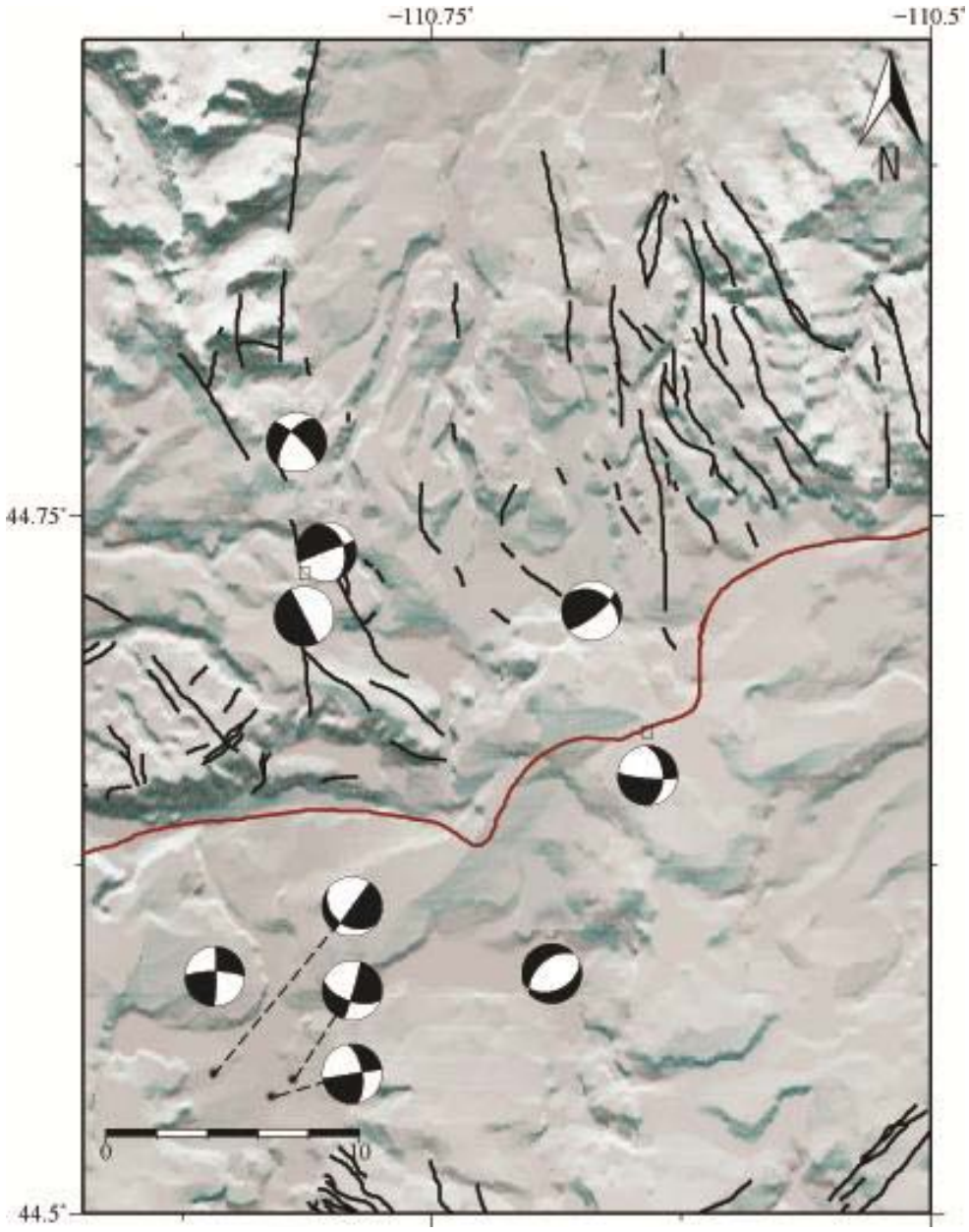

Figure 7.10: Map of selected focal mechanisms in Norris Geyser Basin area, at depths greater than 8 km, below the supposed 12° SE dipping contracting sill, during the subsidence stage (2004-2010) (Chang et al., 2007). Quaternary faults are shown as black lines. The topographic data is provided by the USGS National Elevation Dataset.

In the study by Chang et al. (2007), also the correlation between seismic activity and temporal history of deformation of the Sour Creek resurgent dome area has been examined (figure 6.7).

In this study, our aim was to examine the focal mechanism solutions and the relative P and T axes belonging to the Sour Creek resurgent dome area for each stage, as we did for the Norris Geyser Basin area, but the database did not contain enough events to make the analysis statistically relevant.

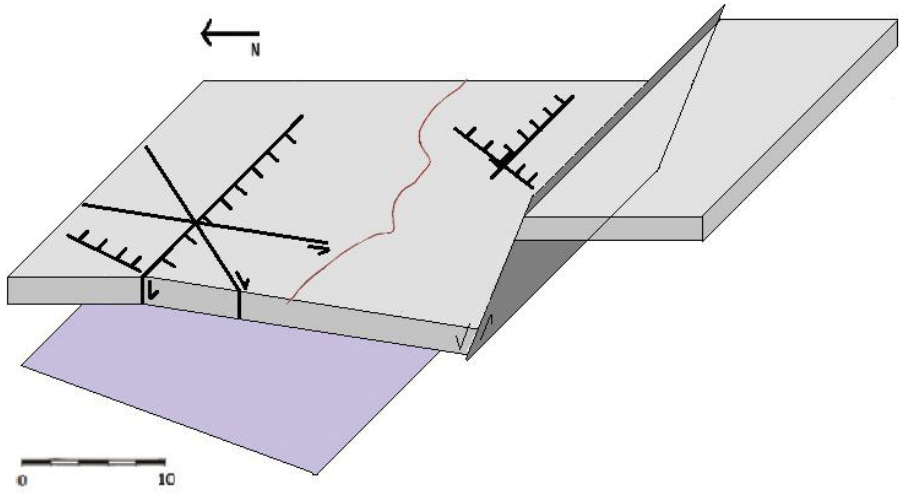

Figure 7.11: Interpretation of the deformation in the Norris Geyser Basin area, during the subsidence stage (2004-2010), between 0 to 5 km depth, above the 12° SE dipping contracting sill supposed by the study by Chang et al. (2007). The 0.64 Ma Yellowstone caldera is shown as a red line, the purple surface represents the contracting sill. Black lines represent perpendicular normal faults (forming the “chocolate tablet” structures) and strike-slip faults..

7.2 Evaluation of the evolving stress field inside the 0.64 Ma Yellowstone caldera: results and discussion

According to the studies by Puskas et al. (2007) and Chang et al. (2010), the 0.64 Ma Yellowstone caldera experienced five clear periods of caldera-wide deformation between 1972 and 2010: 1) uplift at a rate of 22 mm/yr from the early 1970s until 1985; 2) 10-years of subsidence at a rate of 14 mm/yr; 3) uplift from 1995 to 2000 at a rate of 9 mm/yr; 4) subsidence until 2004 at the same rate; and 5) uplift from 2004 to 2010 at a rate of 50 mm/yr, as it is shown in figure 7.12 (Puskas et al., 2007; Chang et al., 2010).

Based on the deformation studies, we subdivided our data in order to examine the relationship between the style of faulting and caldera-wide deformation through time. We used four temporal windows that correspond respectively to periods of subsidence, uplift, subsidence and uplift: 1988-1995, 1995-2000, 2000-2004, 2004-2010.

The first and second temporal windows contain only 3 and 6 events, respectively. For this reason, the analysis is not statistically relevant. The focal mechanism solutions are all dip-slip normal to strike-slip with some dip-slip component, and none of them indicates a remobilization of

Quaternary faults, but a creation of new structures instead (figures 7.13 and 7.14).

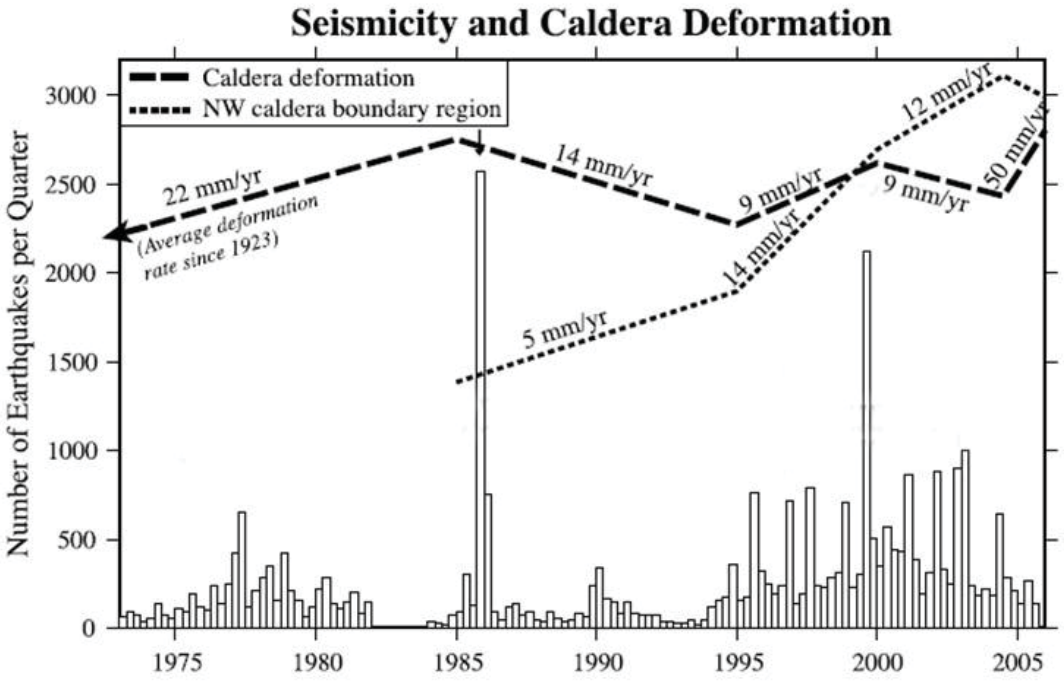

Figure 7.12: Plot of Yellowstone plateau seismicity (Puskas et al., 2007) and deformation. Histogram showing number of earthquakes per quarter and trends in caldera deformation from leveling and GPS campaigns.

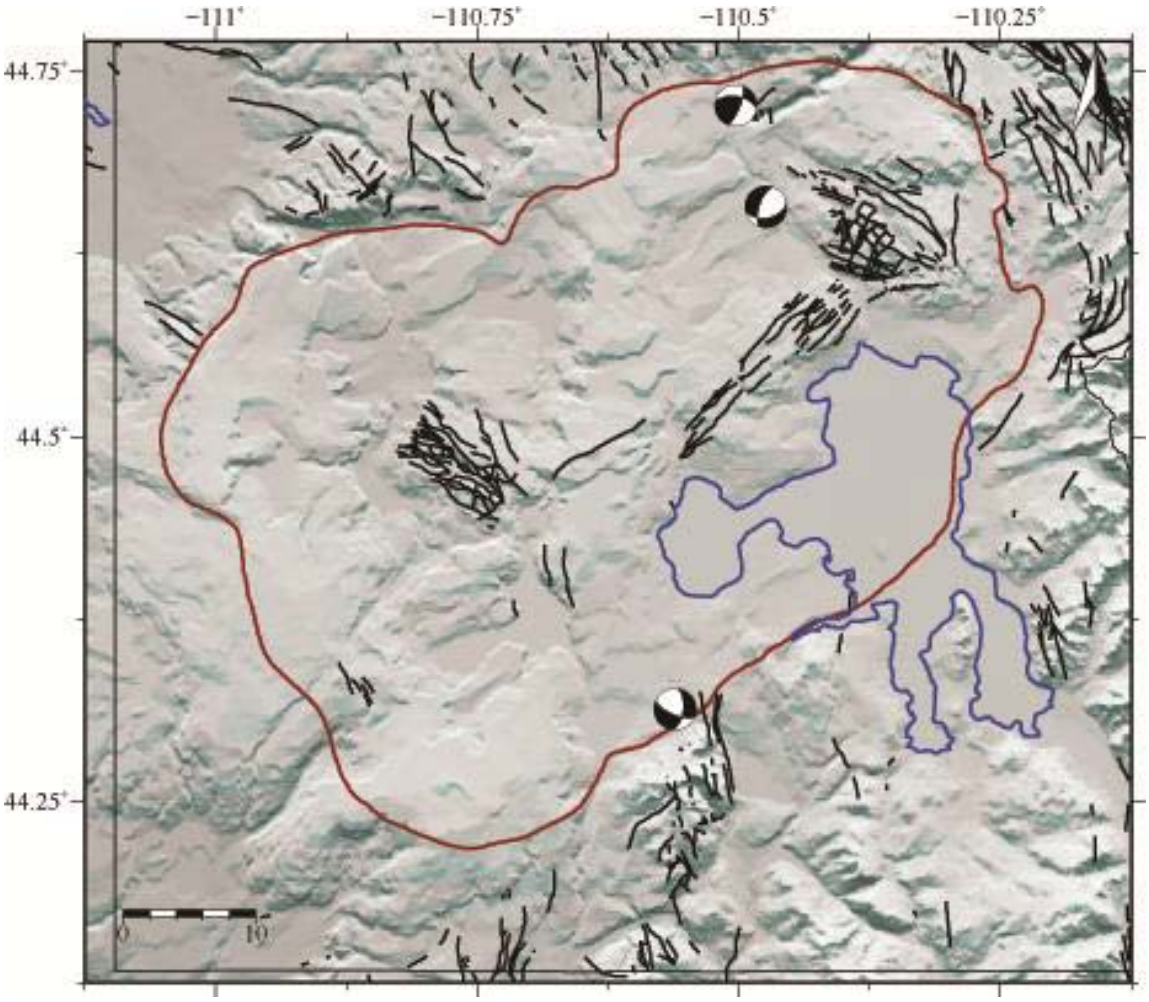

Figure 7.13: Map of selected focal mechanisms in 0.64 Ma Yellowstone caldera area, from 1988 to 1995 (subsidence stage).The red line represents the caldera border, the blue line is the Yellowstone Lake. Quaternary faults are shown as black lines. The topographic data is provided by the USGS National Elevation Dataset.

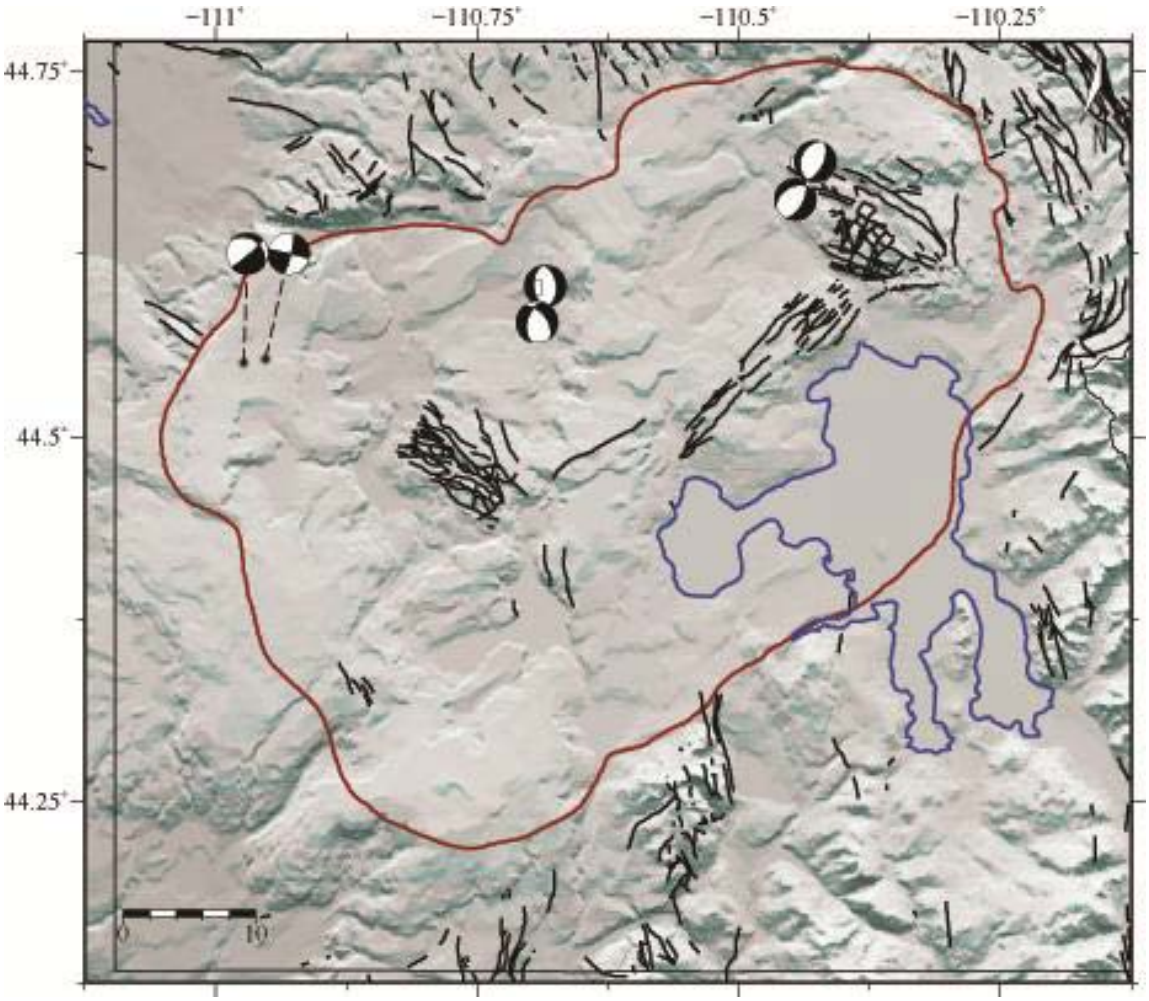

Figure 7.14: Map of selected focal mechanisms in 0.64 Ma Yellowstone caldera area, from 1995 to 2000 (uplift stage) as in Figure 7.13. The topographic data is provided by the USGS National Elevation Dataset.

The last two temporal windows contain 44 and 103 events, respectively. In the subsidence stage between 2000 and 2004, faulting consistent with “chocolate tablet” structures occurs in parts of the Yellowstone caldera, especially west of the Yellowstone Lake and north-east of the Mallard Lake resurgent dome. In these areas, earthquakes occur mostly with a NNW-SSE normal faulting system and an ENE-WSW normal faulting system. Strike-slip with some dip-slip movement faults are distributed all over the area (figure 7.15).

In the last temporal window, lasting from 2004 to 2010, the deformation continues to develop especially in the northwestern part of the caldera, north of the Mallard Lake resurgent dome, mainly along strike-slip faults, NNW-SSE to NNE-SSW and few ENE-WSW dip-slip normal faults. The deformation is also concentrated close to the caldera southern rim and, as it was not detected in the previous temporal window, this uplift stage is also characterized by deformation in the area inside the Yellowstone Lake, predominantly along N-S to NNE-SSW normal faults, few nearly E-W normal faults and strike-slip faults (figure 7.16).

All the deformation in the 0.64 Ma Yellowstone caldera is determined by the creation of new structures rather than by the remobilization of already mapped Quaternary faults, except one case in the temporal window between 2004 and 2010 (shown in red in figure 7.16).

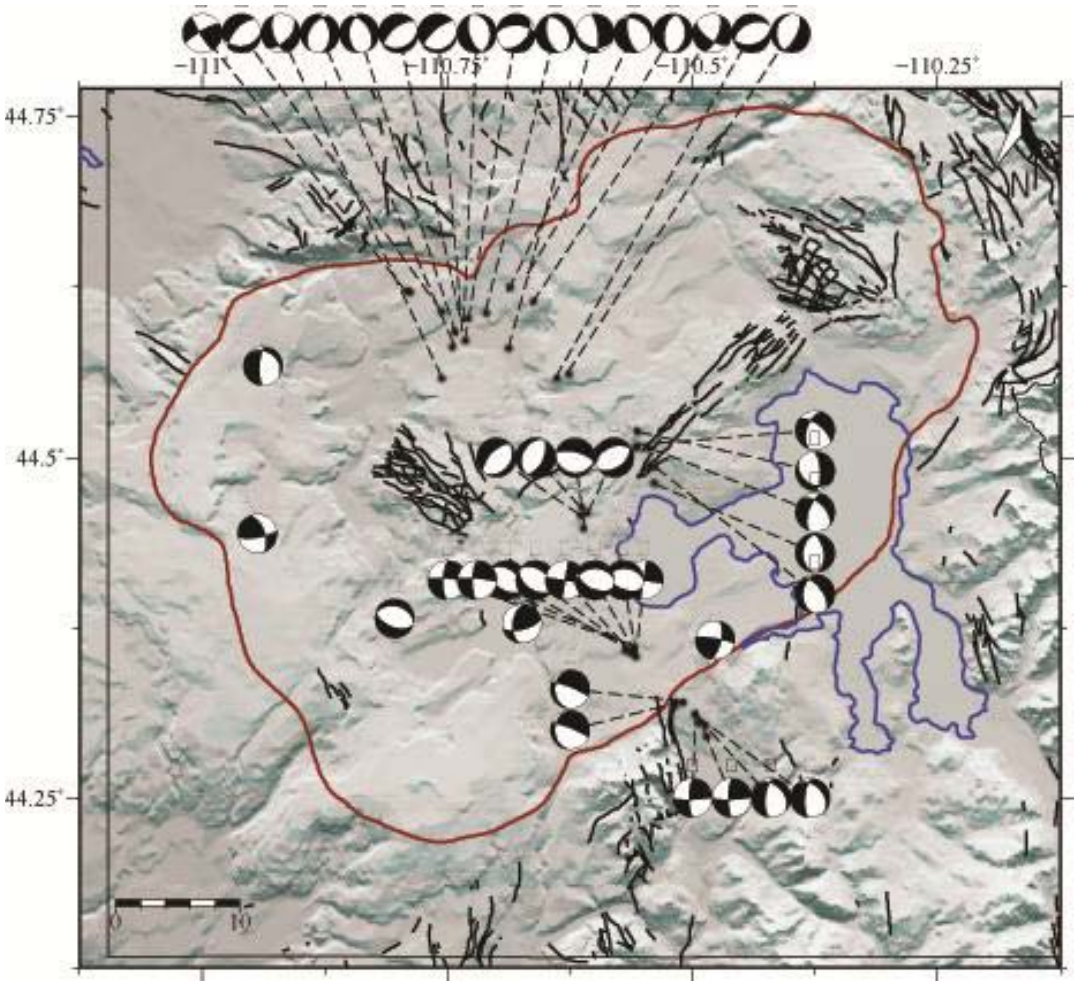

Figure 7.15: Map of selected focal mechanisms in 0.64 Ma Yellowstone caldera area, from 2000 to 2004 (subsidence stage), as in Figure 7.13. The topographic data is provided by the USGS National Elevation Dataset.

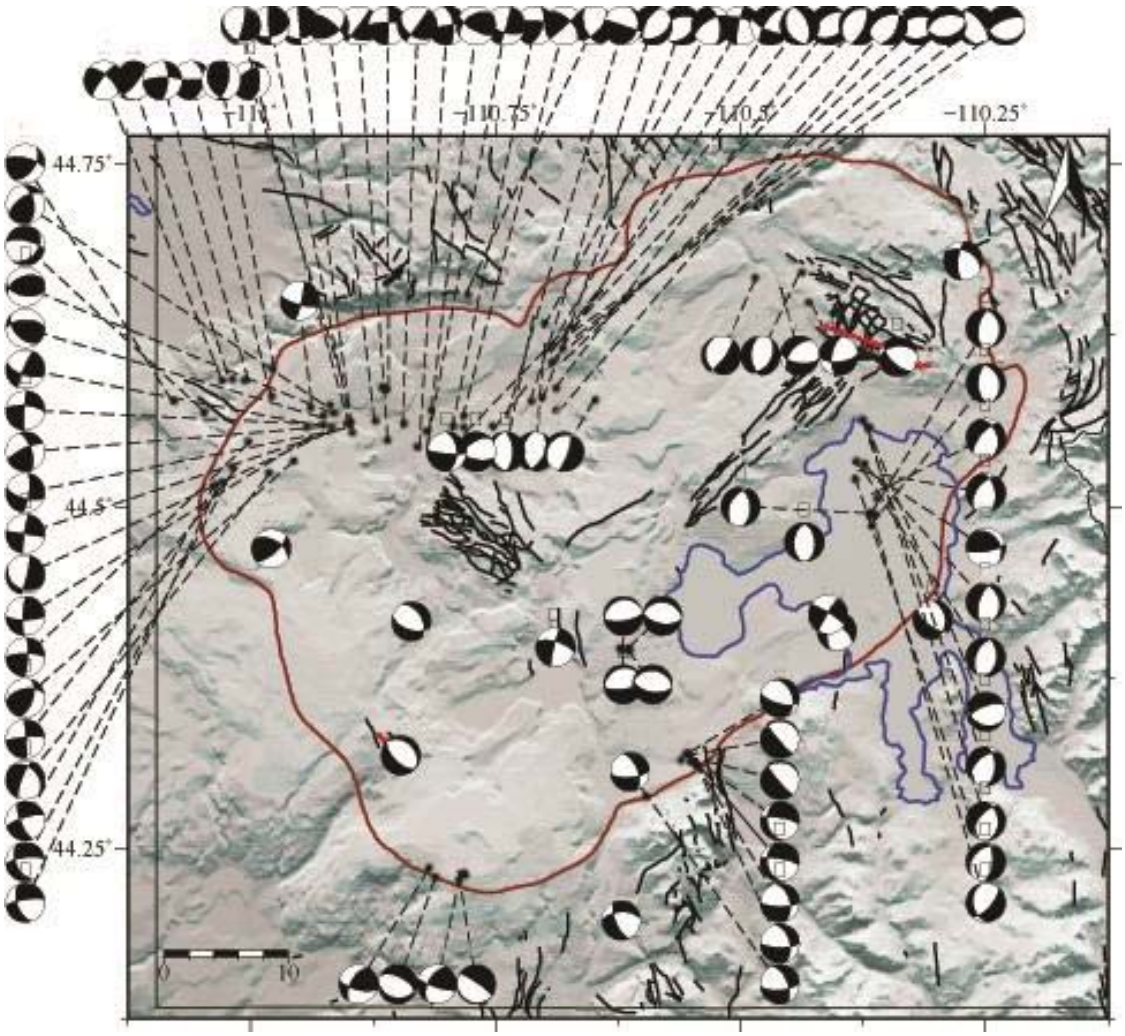

Figure 7.16: Map of selected focal mechanisms in 0.64 Ma Yellowstone caldera area, from 2004 to 2010 (uplift stage), as in Figure 7.13. Quaternary faults are shown as black lines, with Quaternary faults that may be responsible for some of the earthquakes shown as red lines. The topographic data is provided by the USGS National Elevation Dataset.

7.2.1 Evaluation of the correlation between deformation and depth within the 0.64 Ma Yellowstone caldera (2004-2010)

The studies by Chang et al. (2007; 2010) suppose that the last uplift stage of the 0.64 Ma Yellowstone caldera, lasting from 2004 to 2010, in coincidence with subsidence in the upper Norris Geyser Basin area, was due to an inflating sill, at depths between ~7 and 11 km, as shown in figure 7.17.

In this study, we selected the data belonging to the temporal window between 2004 and 2007 in order to create three depth subdivisions: from 0 to 7 km, to explore the deformation above the inflating sill, from 7 to 11 km, and below 11 km, to examine the deformation style below the expanding sill. The first two depth windows have 17 and 8 events, respectively. Unfortunately, the database used in this study did not contain any events below 11 km, so it is impossible to investigate the deformation below the sill.

By looking at the results of the event selection belonging to the first two depth windows, we noticed that most of the focal mechanism solutions are not located above the proposed sill, which occupies the SSW-NNE part of

the Yellowstone caldera, but they are concentrated mainly in the northwestern part or immediately below the south caldera rim. Only four focal mechanism solutions, in the depth window between 0 and 7 km and located above the Sour Creek resurgent dome, may represent the deformation above the sill. These indicate movement along two dip-slip normal faults with a WNW-ESE and NNE-SSW direction respectively, and two strike-slip faults. In particular, the nearly E-W normal fault may represent a remobilization of a Quaternary fault.

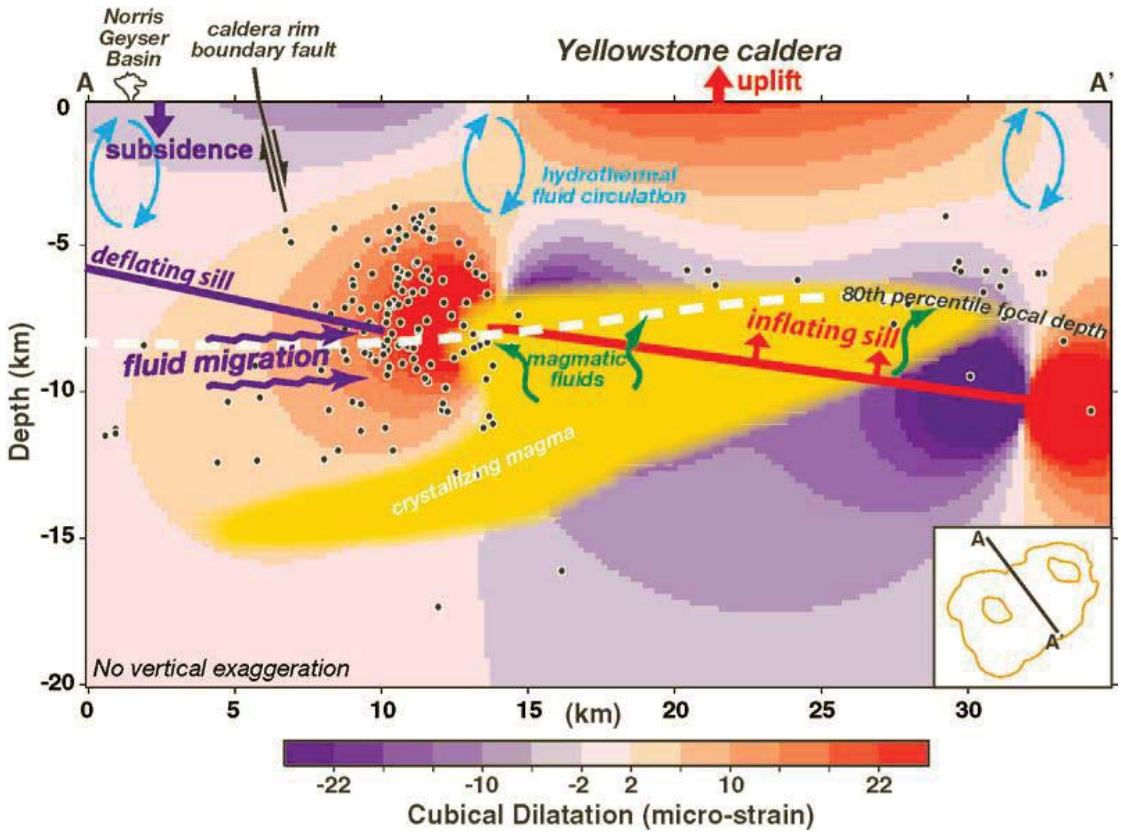

Figure 7.17: Schematic diagram of plausible magmatic and hydrothermal processes responsible for 2004-2007 accelerated Yellowstone caldera uplift and Norris subsidence. Black dots are earthquake hypocenters in the time window between 2004 and 2007, used in Chang et al.'s study (2007). The yellow area shows the seismically imaged magma body. Background colors represent cubical dilatation, in unit changes of volume, induced by the modeled inflating sill. Fluids exsolved from magma crystallization can be trapped beneath the nonpermeable rocks near the brittle-ductile transition zone (Chang et al., 2007).

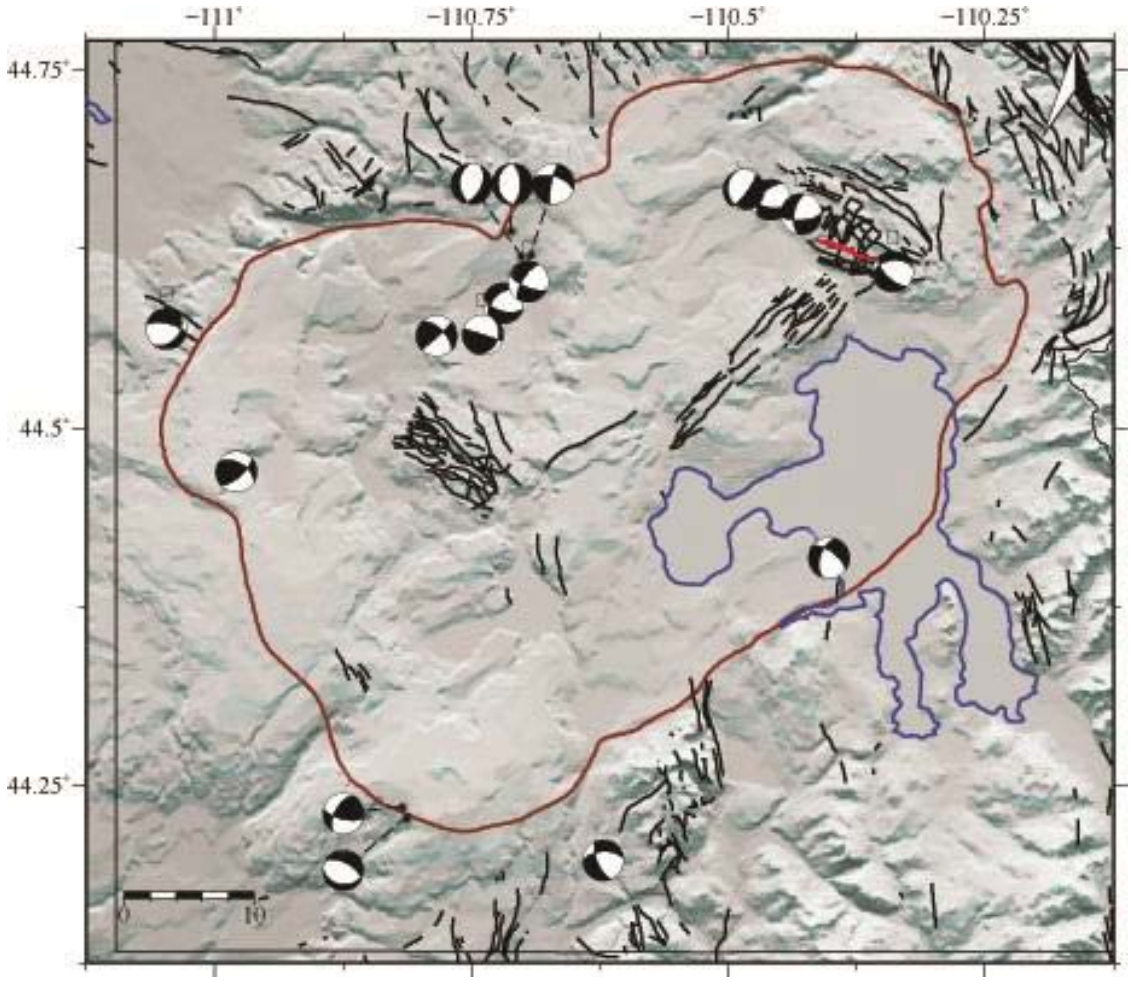

Figure 7.18: Map of selected focal mechanisms in 0.64 Ma Yellowstone caldera area, during the temporal window between 2004 and 2007 (uplift stage) and belonging to the depth window between 0 and 7 km, above the supposed expanding sill (Chang et al., 2007). The red line represent the caldera border, the blue line is the Yellowstone Lake. Quaternary faults are shown as black lines, reactivated Quaternary faults are shown as red lines. The topographic data is provided by the USGS National Elevation Dataset.

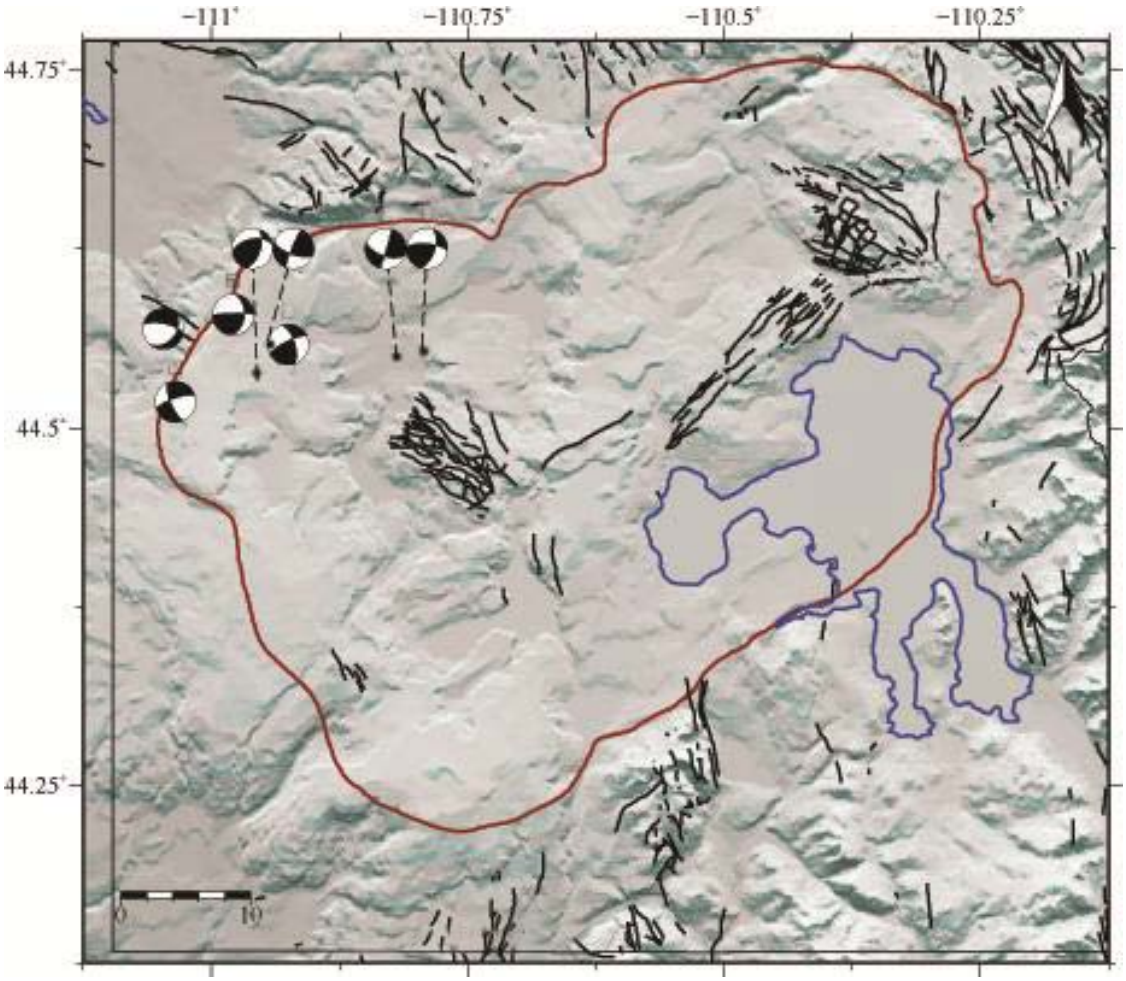

Figure 7.19: Map of selected focal mechanisms in 0.64 Ma Yellowstone caldera area, during the temporal window between 2004 and 2007 (uplift stage) and belonging to the depth window between 7 and 11 km, where the supposed expanding sill is located (Chang et al., 2007). The red line represent the caldera border, the blue line is the Yellowstone Lake. Quaternary faults are shown as black lines. The topographic data is provided by the USGS National Elevation Dataset.

CHAPTER 8

CONCLUSIONS

Being one of the most active volcanic systems all over the world, the silicic Yellowstone volcanic field is characterized by a high seismicity and a continuous deformation. The questions addressed in this research relate to the evaluation of model stress-field solutions from P-wave polarity data and focal mechanisms and both temporal and spatial changes in the deformation pattern inside the 0.64 Ma Yellowstone caldera. Even though the seismic activity still looks higher north of the current caldera, suggesting a particularly highly fractured crust, as it was already detected in previous works, the database used in this study comprises also a high quantity of events located inside the caldera, except the southern and north-eastern part, where the population is too sparse to compute reliable stress tensor inversions.

The 369 focal mechanism solutions showed normal to strike-slip faults, accordingly to the tectonically active extensional Basin and Range province, where the Yellowstone volcanic field is located. In order to define areas

with a nearly homogeneous stress, the difference in the fit score between the stress-constrained and unconstrained focal mechanism was taken into account: this value should be lower than 2.32, or at least as close as possible to it. Finally, ten areas were defined but not all of them could be considered reliable; in fact, some areas south of the Yellowstone caldera and within the caldera contained a small number of earthquakes, causing the stress inversion results to be not reliable enough to be considered.

According to our results, σ_1 is nearly vertical all over the Yellowstone area, while the direction of σ_3 rotates from NNE-SSW near the Hebgen Lake fault zone to ENE-WSW near Norris Junction. In some areas inside the caldera, the direction of σ_3 is nearly parallel to the caldera rim. An interesting result shows that the σ_3 direction in the area around Norris Geyser Basin seems to have changed throughout the years, varying from ENE-WSW, as it was computed in Waite and Smith (2004), to NNE-SSW. This could reflect the time influence on stress-field variations; elsewhere, except the σ_3 directions look unchanged. According to our stress inversions and coherently with previous studies, the direction of extension through the 0.64 Ma Yellowstone caldera looks nearly ENE. This is indicated by

alignments of volcanic vents within the caldera which can be considered as links between extensional structures north and south of the caldera, a suggestion made by Ruppel in 1972 and Christiansen in 2001. As it was already revealed in 2004 by Waite and Smith's study, this research confirms that the N-S striking faults to the north of the caldera may no longer be active.

The evaluation of spatial and temporal deformation both in the 0.64 Ma Yellowstone caldera and in the Norris Geyser Basin area showed the onset of "chocolate tablet" structures, composed by a double set of orthogonal dilational fractures, due to a change between σ_2 and σ_3. The sets of perpendicular normal faults on the Sour Creek and Mallard Lake resurgent domes also demonstrate this style of deformation. The strike-slip deformation below the 5-8 km 12° SE dipping contracting sill, believed to have caused the subsidence stage, between 2004 and 2010, in the Norris Geyser Basin area (Chang et al., 2007), indicates the movement of magmatic material towards the 0.64 Ma Yellowstone caldera. Except for a few cases, the mapped Quaternary faults inside and outside the caldera look inactive, and the results of this research suggest the creation of new

structures, which in most cases are not visible on satellite images, mainly due to the depth of the events.

9.

APPENDIX A

P AND T AXES

IN THE NORRIS GEYSER BASIN AREA

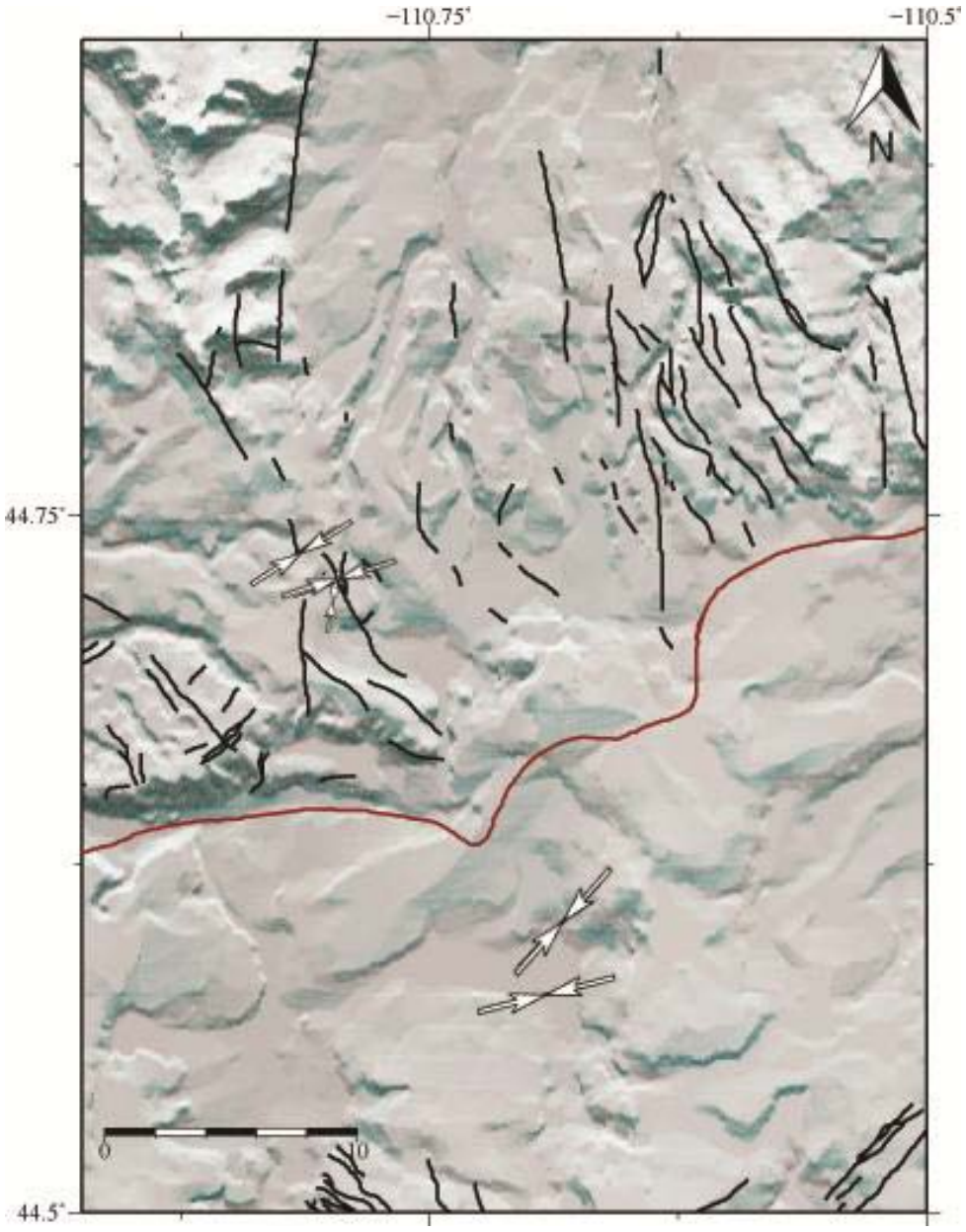

Figure A.1: Mapped orientation of P axes of focal mechanism solutions in the Norris Geyser Basin area, in the time window between 1996 and 1998 (uplift), shown as white arrows. The length of the arrows represents the inclination of the axes. The 0.64 Ma Yellowstone caldera is shown as a red line, Quaternary faults are shown as black lines. The topographic data is provided by the USGS National Elevation Dataset.

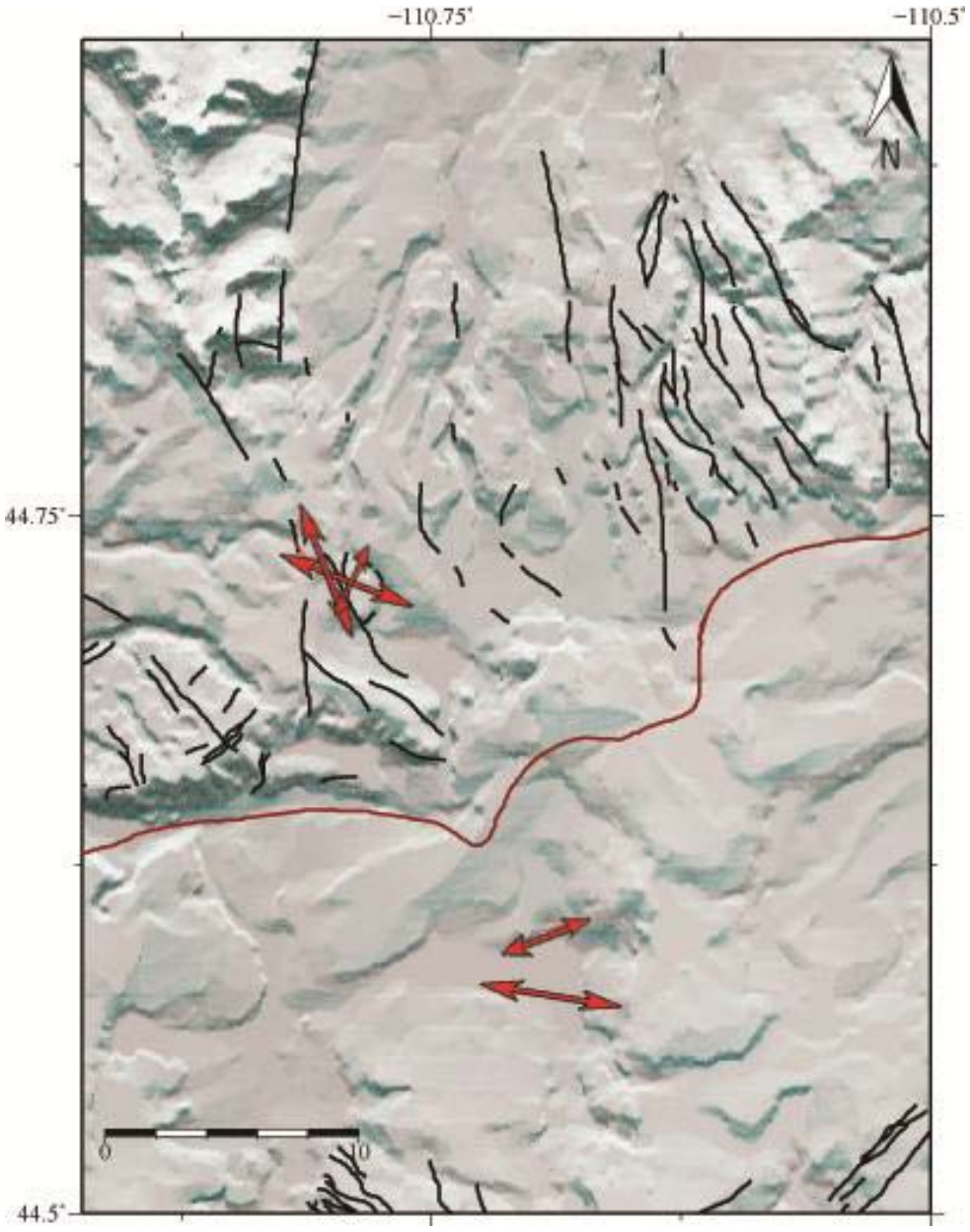

Figure A.2: Mapped orientation of T axes of focal mechanism solutions in the Norris Geyser Basin area, in the time window between 1996 and 1998 (uplift), shown as red arrows. The length of the arrows represents the inclination of the axes. The 0.64 Ma Yellowstone caldera is shown as a red line, Quaternary faults are shown as black lines. The topographic data is provided by the USGS National Elevation Dataset.

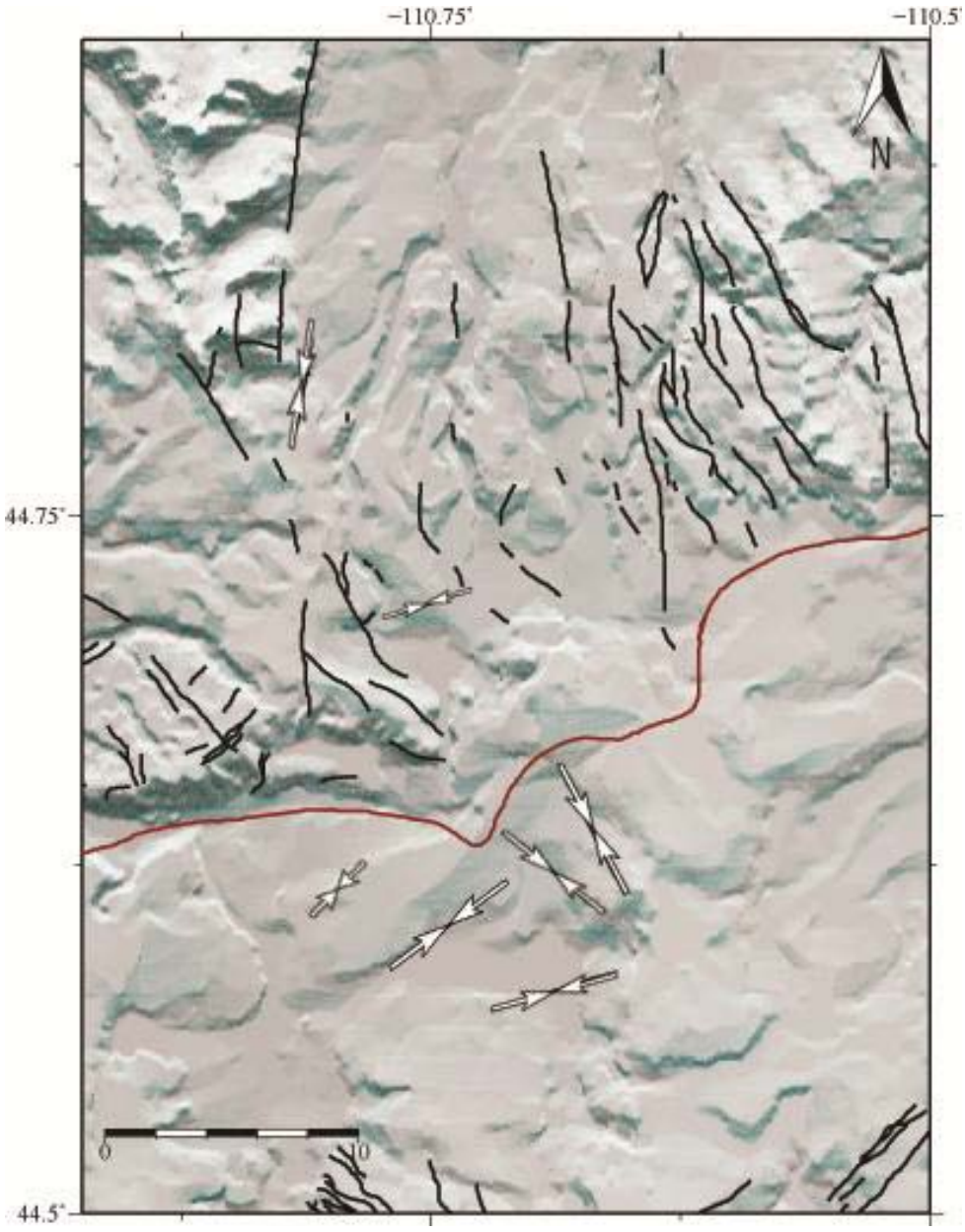

Figure A.3: Mapped orientation of P axes of focal mechanism solutions in the Norris Geyser Basin area, in the time window between 2000 and 2002 (uplift), shown as white arrows. The length of the arrows represents the inclination of the axes. The 0.64 Ma Yellowstone caldera is shown as a red line, Quaternary faults are shown as black lines. The topographic data is provided by the USGS National Elevation Dataset.

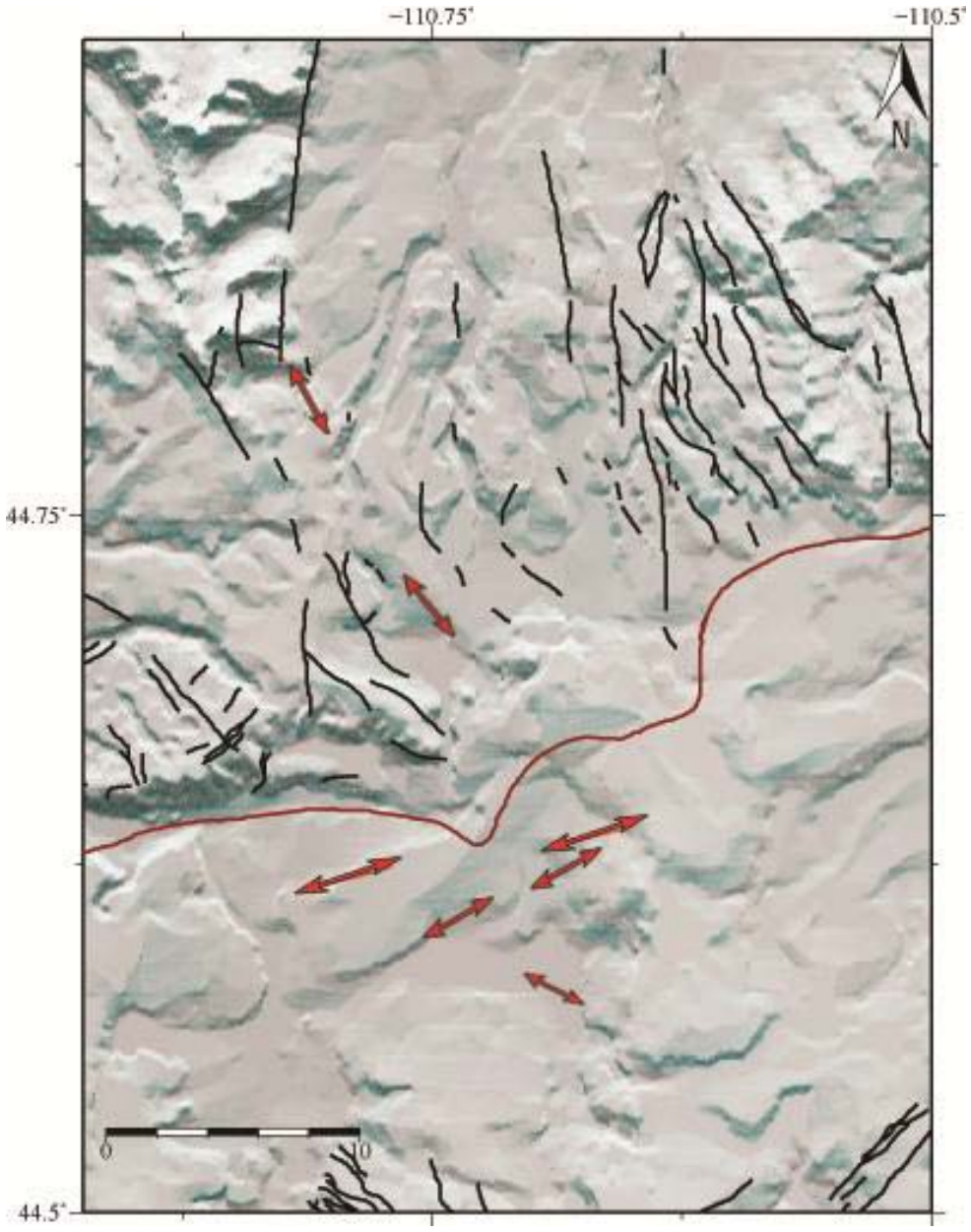

Figure A.4: Mapped orientation of T axes of focal mechanism solutions in the Norris Geyser Basin area, in the time window between 2000 and 2002 (uplift), shown as red arrows. The length of the arrows represents the inclination of the axes. The 0.64 Ma Yellowstone caldera is shown as a red line, Quaternary faults are shown as black lines. The topographic data is provided by the USGS National Elevation Dataset.

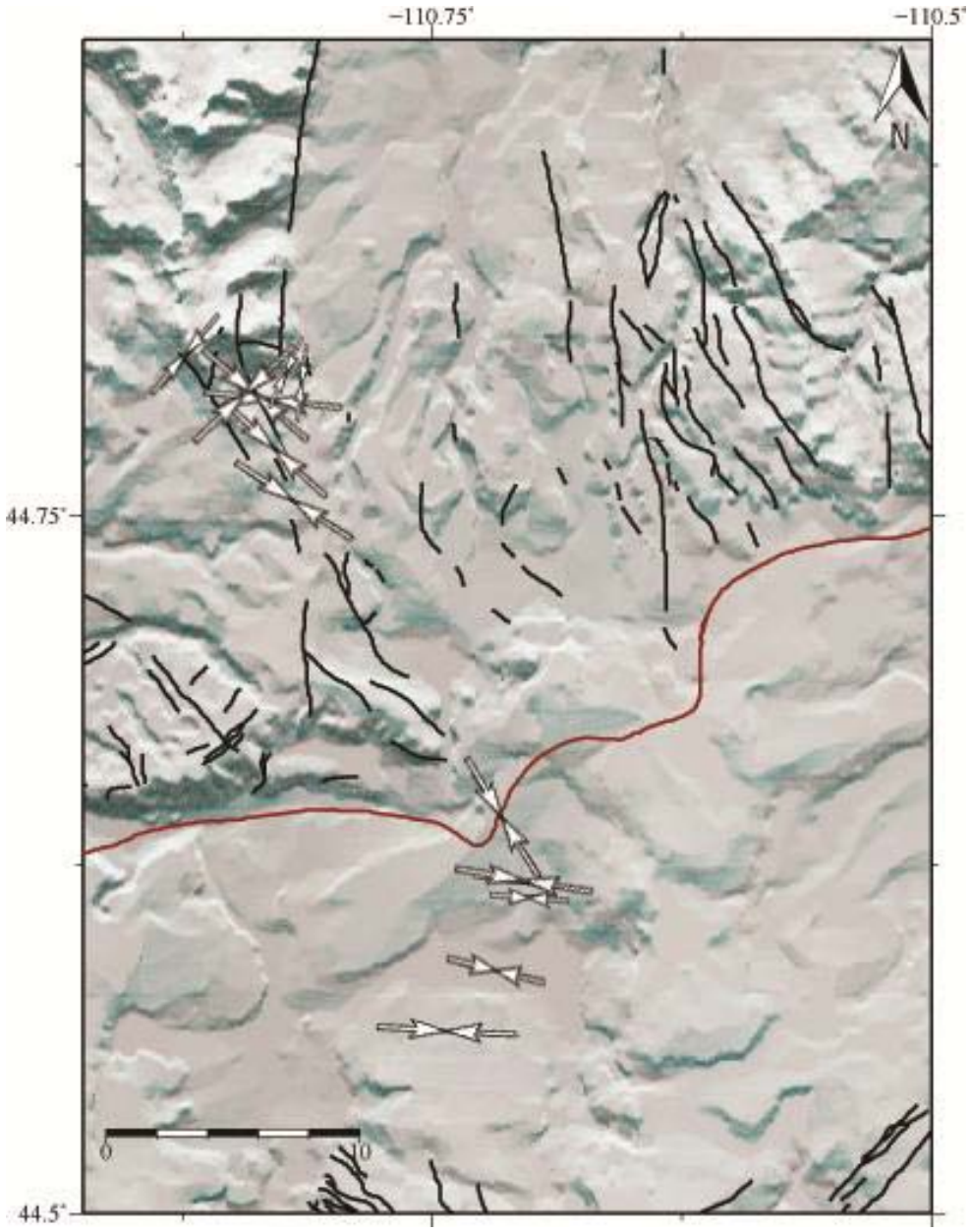

Figure A.5: Mapped orientation of P axes of focal mechanism solutions in the Norris Geyser Basin area, in the time window between 2002 and 2004 (uplift), shown as white arrows. The length of the arrows represents the inclination of the axes. The 0.64 Ma Yellowstone caldera is shown as a red line, Quaternary faults are shown as black lines. The topographic data is provided by the USGS National Elevation Dataset.

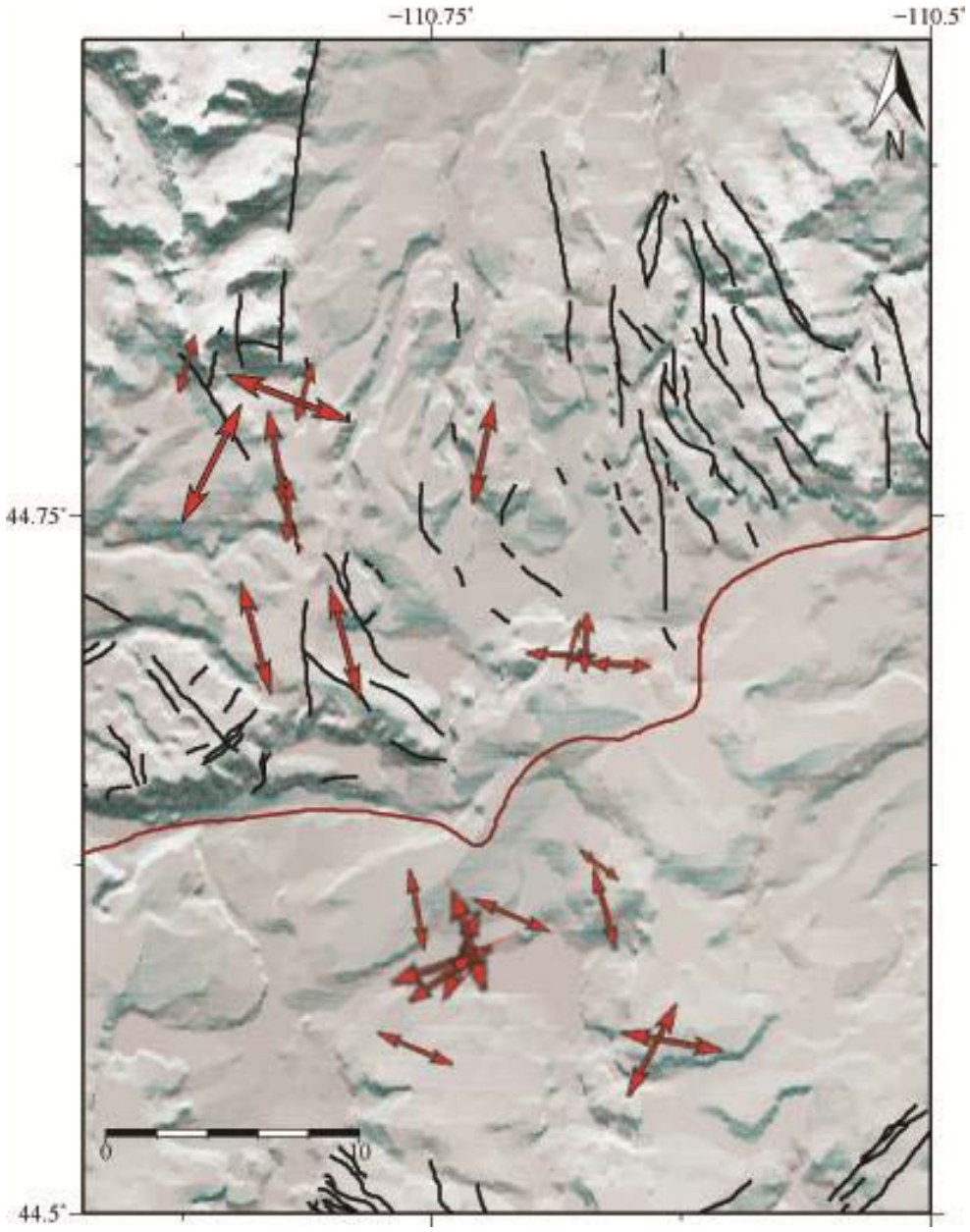

Figure A.6: Mapped orientation of T axes of focal mechanism solutions in the Norris Geyser Basin area, in the time window between 2002 and 2004 (uplift), shown as red arrows. The length of the arrows represents the inclination of the axes. The 0.64 Ma Yellowstone caldera is shown as a red line, Quaternary faults are shown as black lines. The topographic data is provided by the USGS National Elevation Dataset.

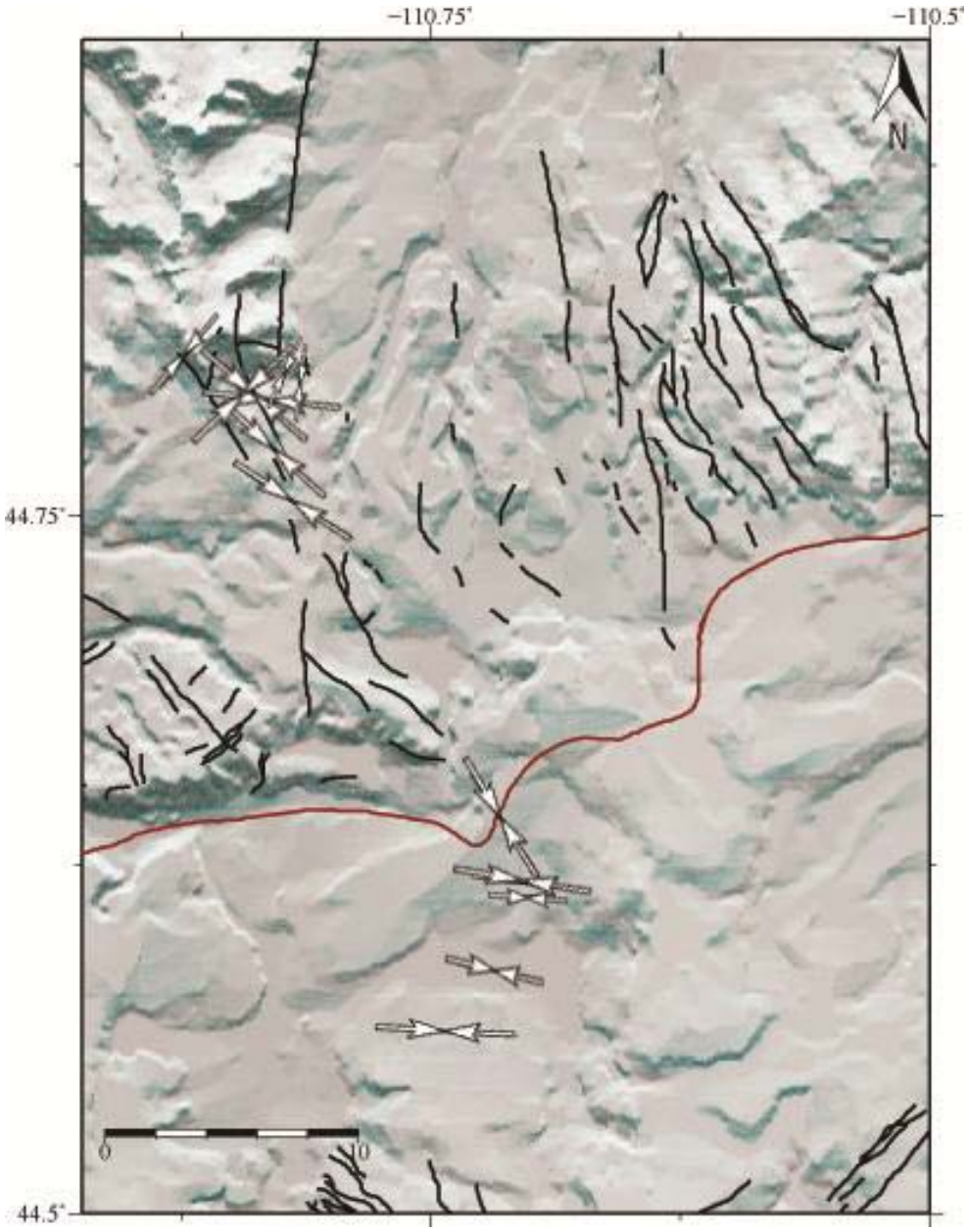

Figure A.7: Mapped orientation of P axes of focal mechanism solutions in the Norris Geyser Basin area, in the time window between 2004 and 2006 (subsidence), shown as white arrows. The length of the arrows represents the inclination of the axes. The 0.64 Ma Yellowstone caldera is shown as a red line, Quaternary faults are shown as black lines. The topographic data is provided by the USGS National Elevation Dataset.

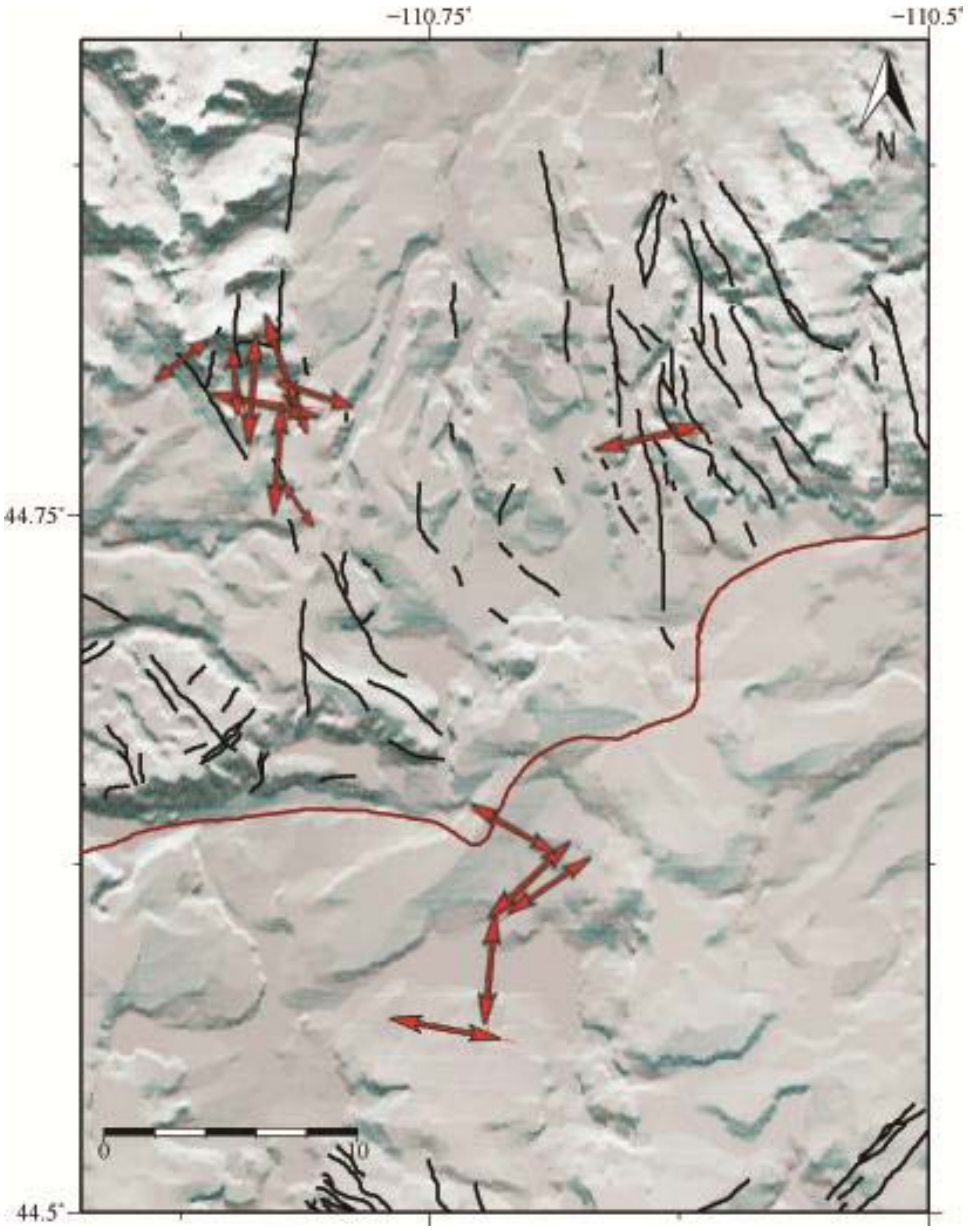

Figure A.8: Mapped orientation of T axes of focal mechanism solutions in the Norris Geyser Basin area, in the time window between 2004 and 2006(subsidence), shown as red arrows. The length of the arrows represents the inclination of the axes. The 0.64 Ma Yellowstone caldera is shown as a red line, Quaternary faults are shown as black lines. The topographic data is provided by the USGS National Elevation Dataset.

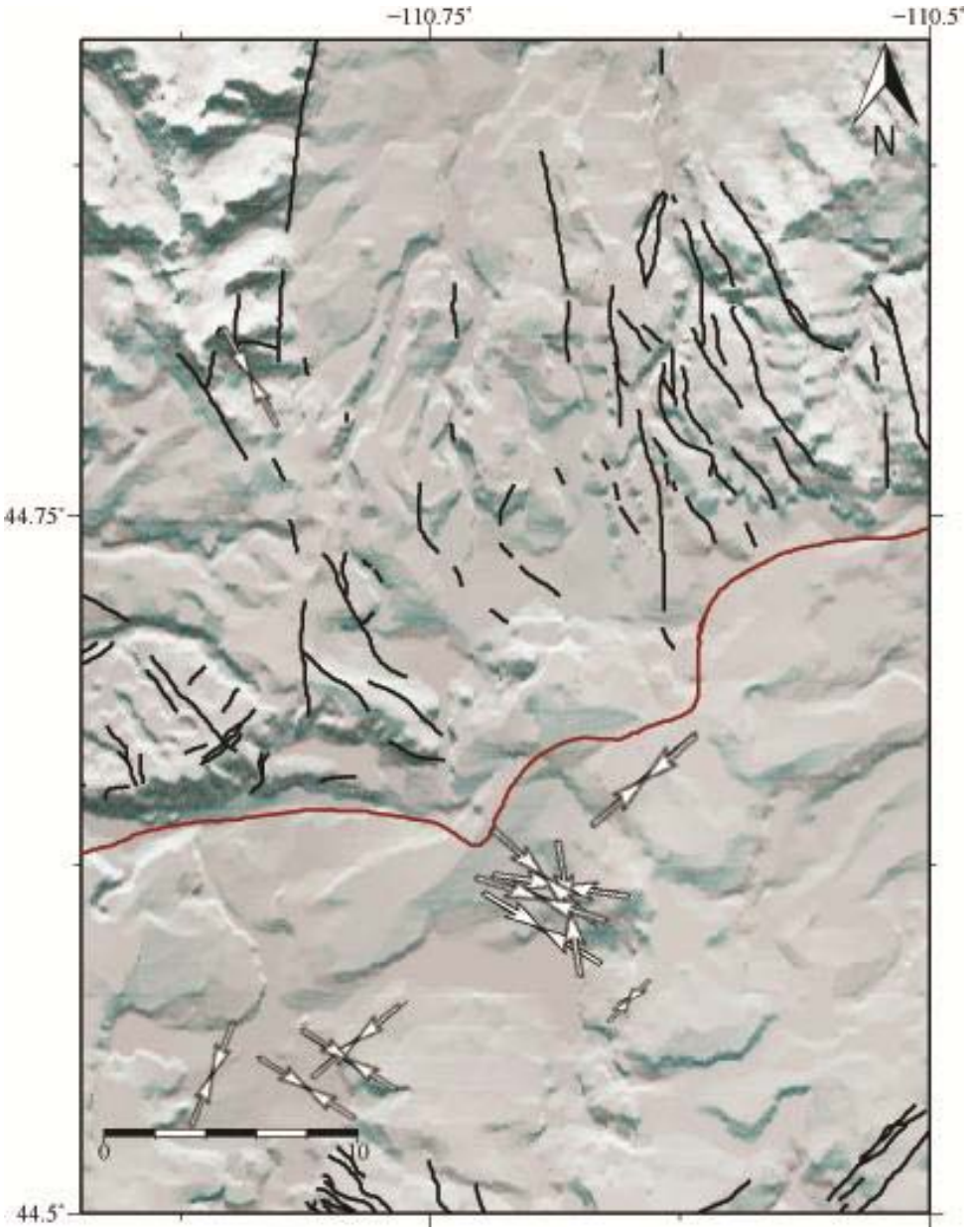

Figure A.9: Mapped orientation of P axes of focal mechanism solutions in the Norris Geyser Basin area, in the time window between 2006 and 2008(subsidence), shown as white arrows. The length of the arrows represents the inclination of the axes. The 0.64 Ma Yellowstone caldera is shown as a red line, Quaternary faults are shown as black lines. The topographic data is provided by the USGS National Elevation Dataset.

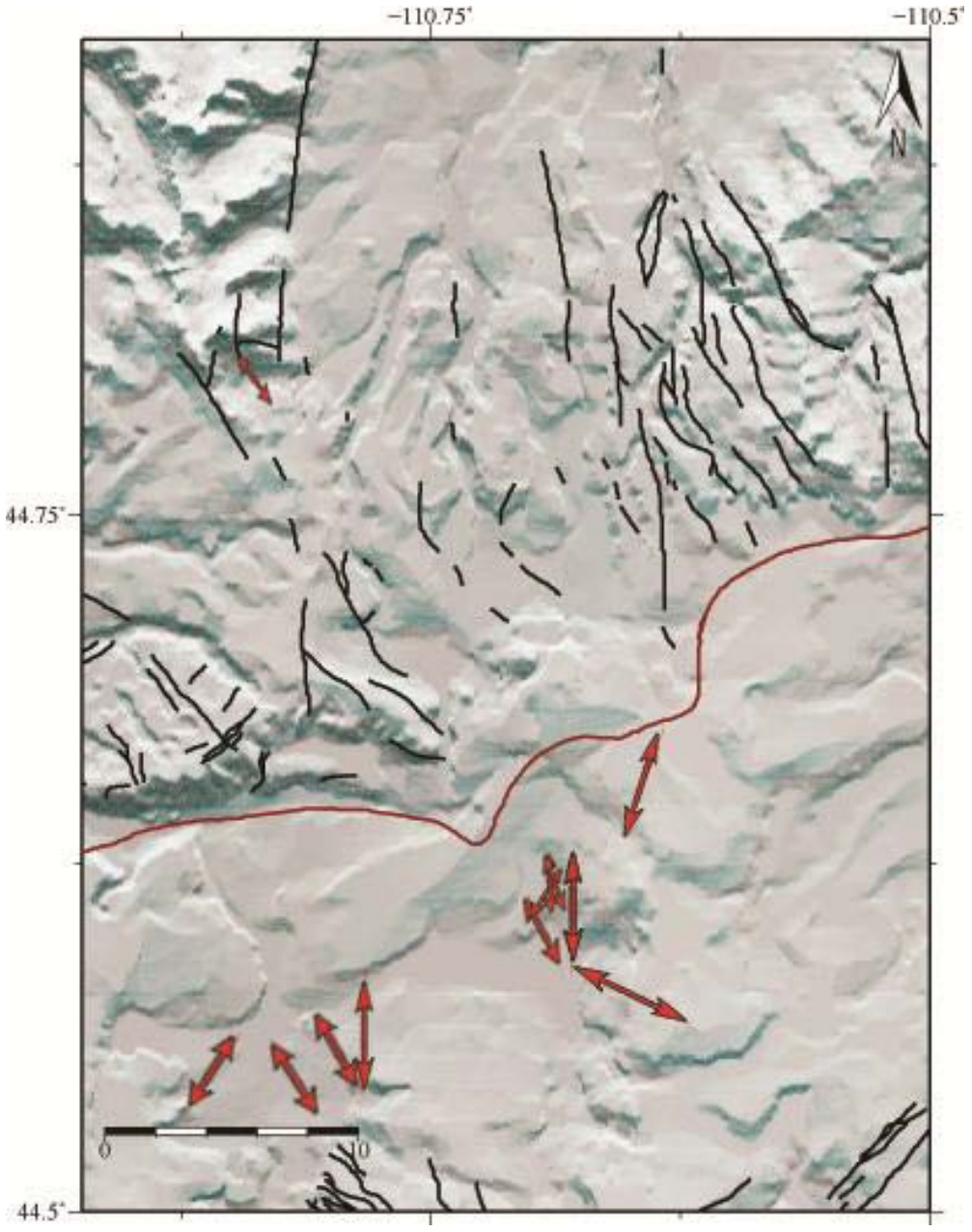

Figure A.10: Mapped orientation of T axes of focal mechanism solutions in the Norris Geyser Basin area, in the time window between 2006 and 2008 (subsidence), shown as red arrows. The 0.64 Ma Yellowstone caldera is shown as a red line, black lines are Quaternary faults. The topographic data is provided by the USGS National Elevation Dataset.

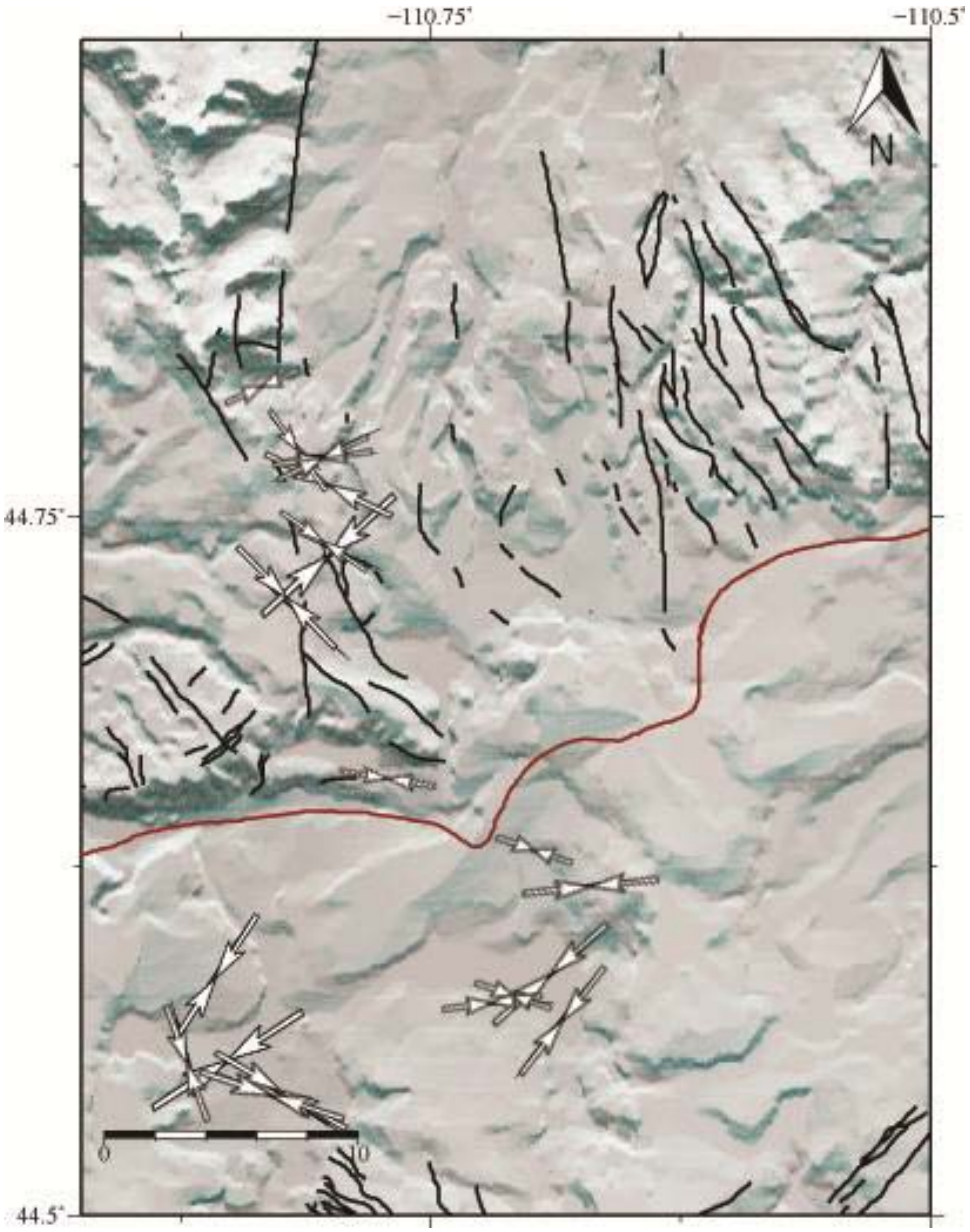

Figure A.11: Mapped orientation of P axes of focal mechanism solutions in the Norris Geyser Basin area, in the time window between 2008 and 2010 (subsidence), shown as white arrows. The length of the arrows represents the inclination of the axes. The 0.64 Ma Yellowstone caldera is shown as a red line, Quaternary faults are shown as black lines. The topographic data is provided by the USGS National Elevation Dataset.

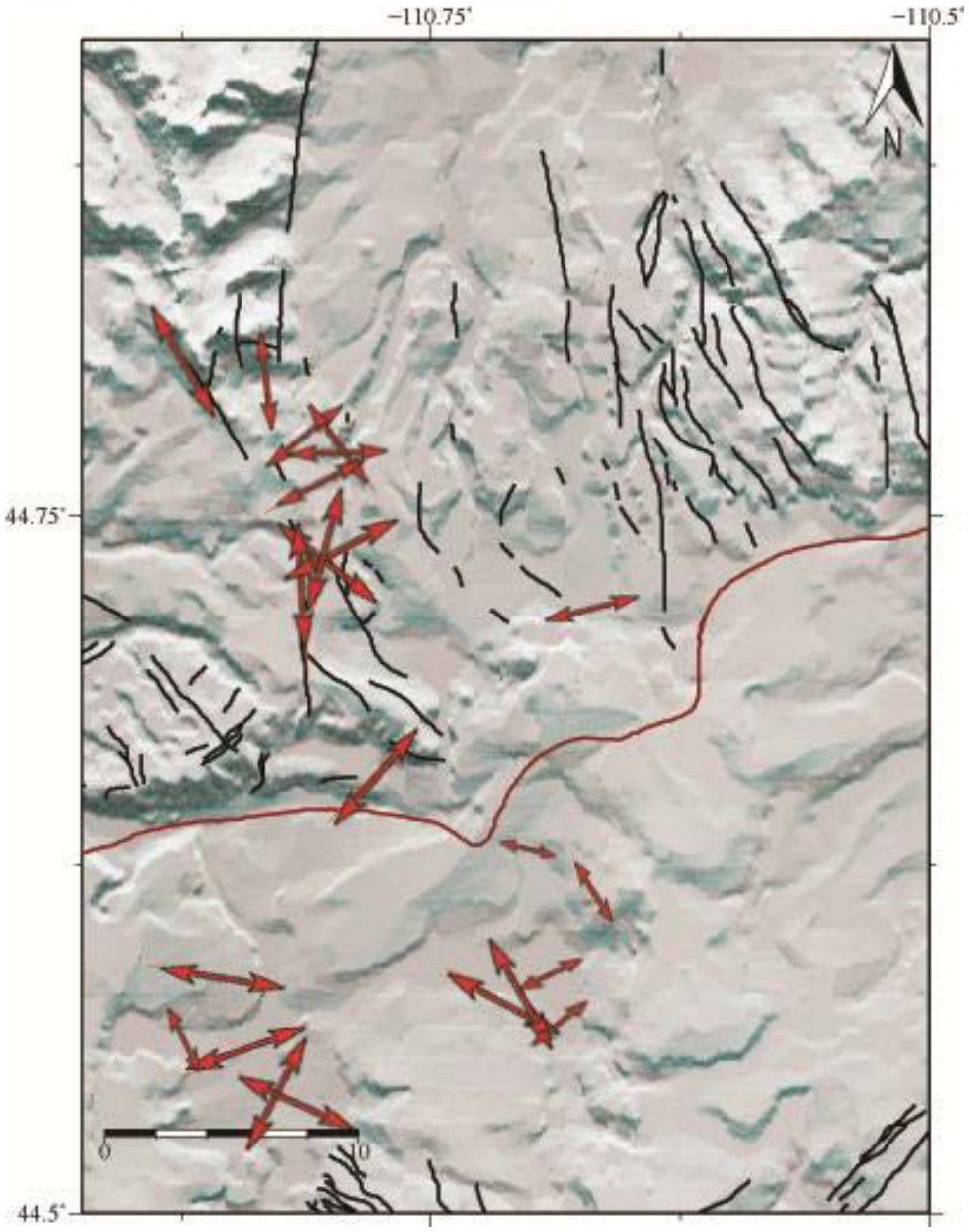

Figure A.12: Mapped orientation of T axes of focal mechanism solutions in the Norris Geyser Basin area, in the time window between 2008 and 2010 (subsidence), shown as red arrows. The length of the arrows represents the inclination of the axes. The 0.64 Ma Yellowstone caldera is shown as a red line, Quaternary faults are shown as black lines. The topographic data is provided by the USGS National Elevation Dataset.

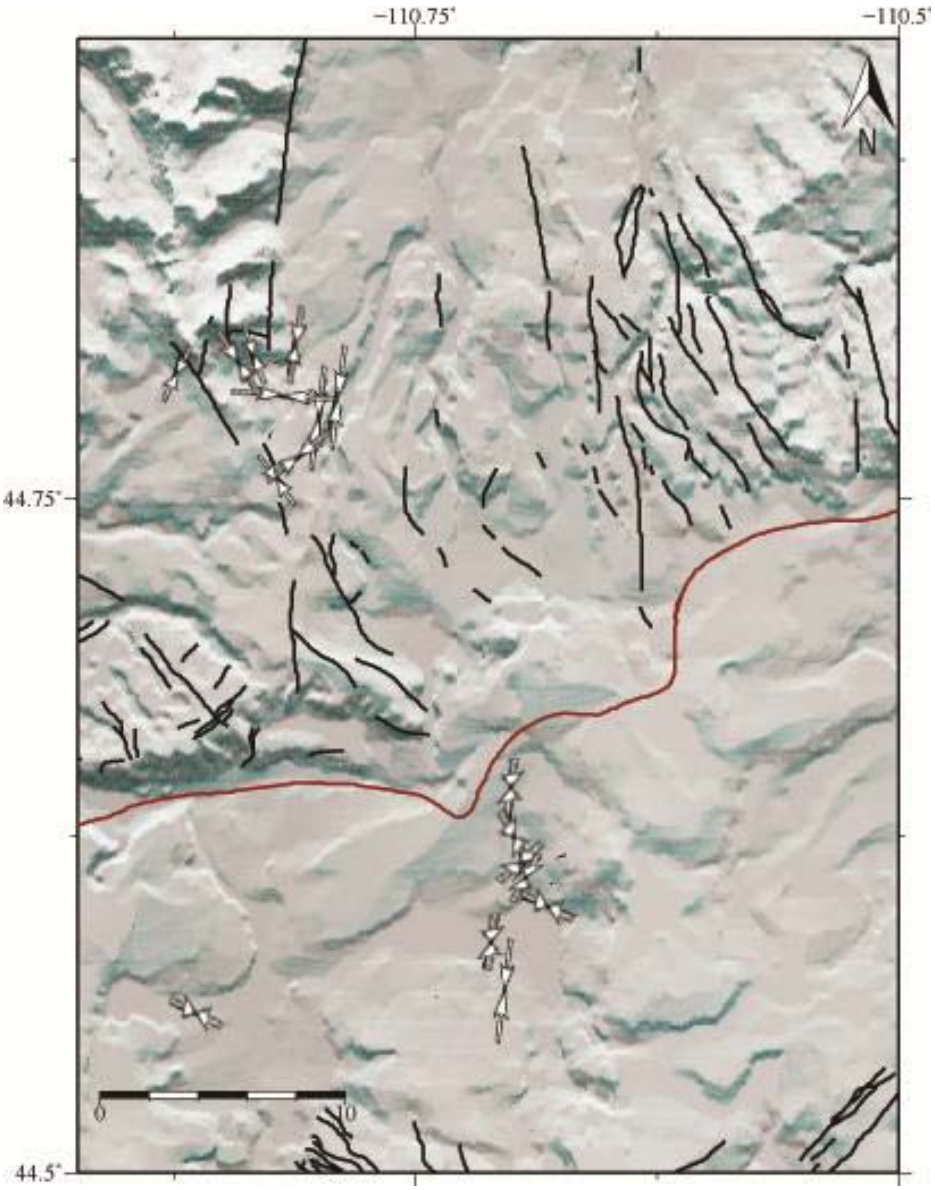

Figure A.13: Mapped orientation of P axes of focal mechanism solutions in the Norris Geyser Basin area, in the time window between 2004 and 2010 (subsidence), in a depth window between 0 and 5 km, above the proposed contracting sill (Chang et al., 2007), shown as white arrows. The length of the arrows represents the inclination of the axes. The 0.64 Ma Yellowstone caldera is shown as a red line, Quaternary faults are shown as black lines. The topographic data is provided by the USGS National Elevation Dataset.

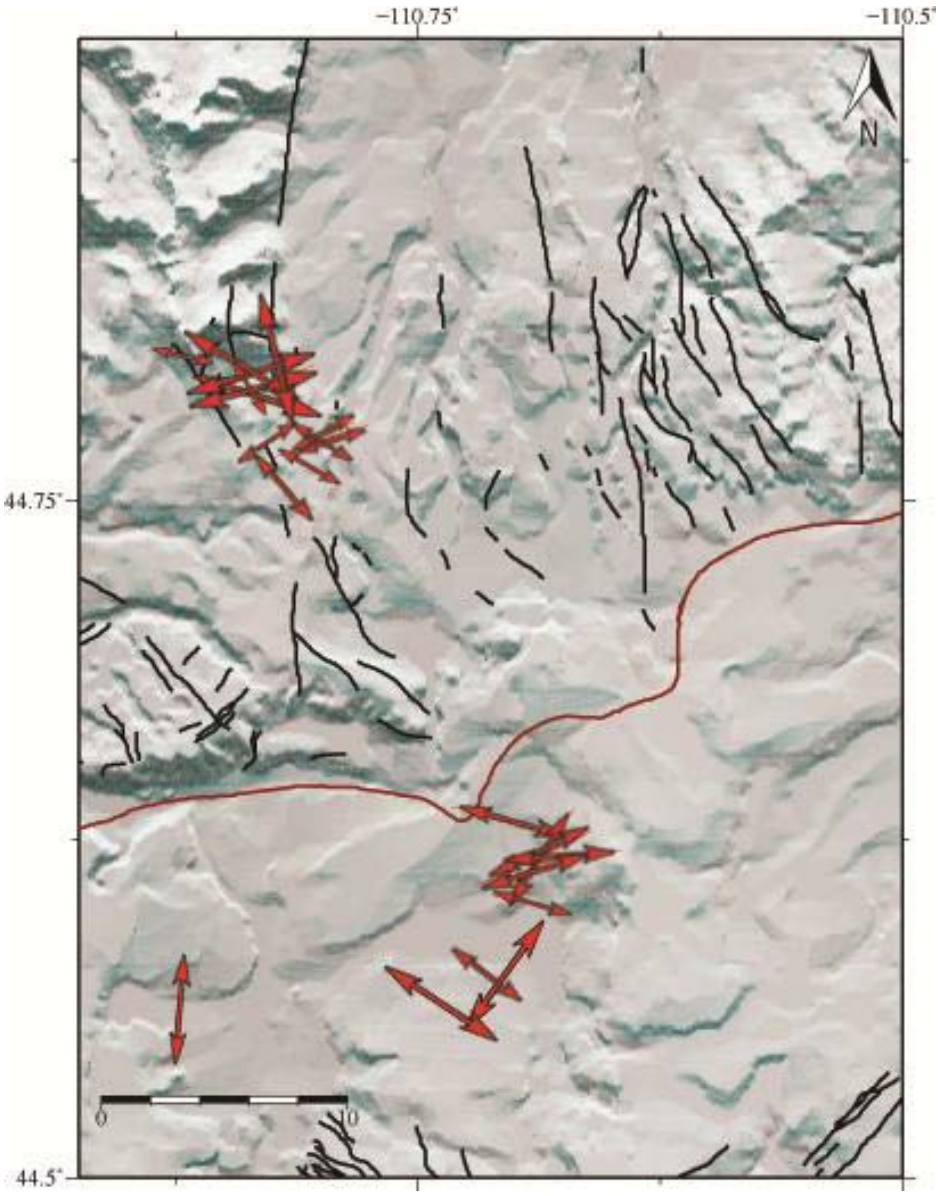

Figure A.14: Mapped orientation of T axes of focal mechanism solutions in the Norris Geyser Basin area, in the time window between 2004 and 2010 (subsidence), in a depth window between 0 and 5 km, above the proposed contracting sill (Chang et al., 2007), shown as red arrows. The length of the arrows represents the inclination of the axes. The 0.64 Ma Yellowstone caldera is shown as a red line, Quaternary faults are shown as black lines. The topographic data is provided by the USGS National Elevation Dataset.

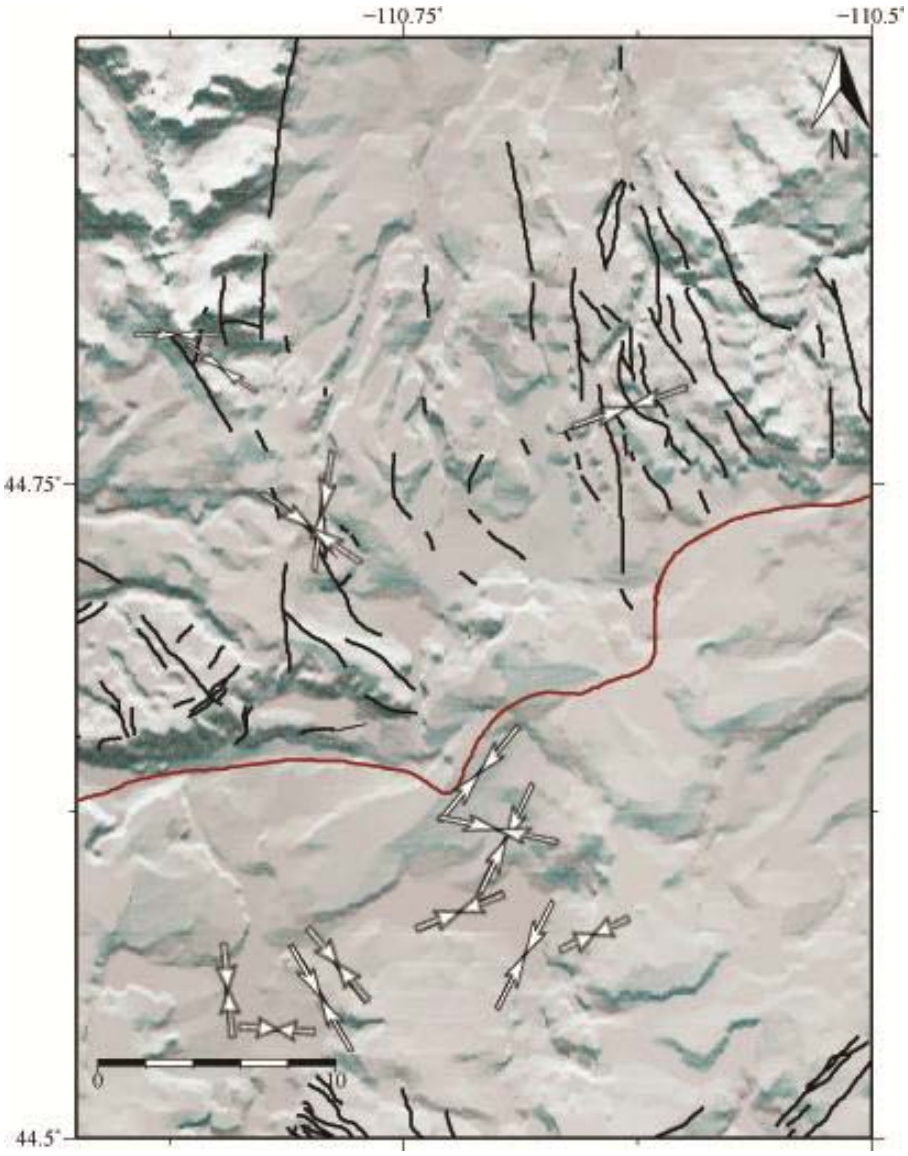

Figure A.15: Mapped orientation of P axes of focal mechanism solutions in the Norris Geyser Basin area, in the time window between 2004 and 2010 (subsidence), in a depth window between 5 and 8 km, where the proposed contracting sill is located (Chang et al., 2007), shown as white arrows. The length of the arrows represents the inclination of the axes. The 0.64 Ma Yellowstone caldera is shown as a red line, Quaternary faults are shown as black lines. The topographic data is provided by the USGS National Elevation Dataset.

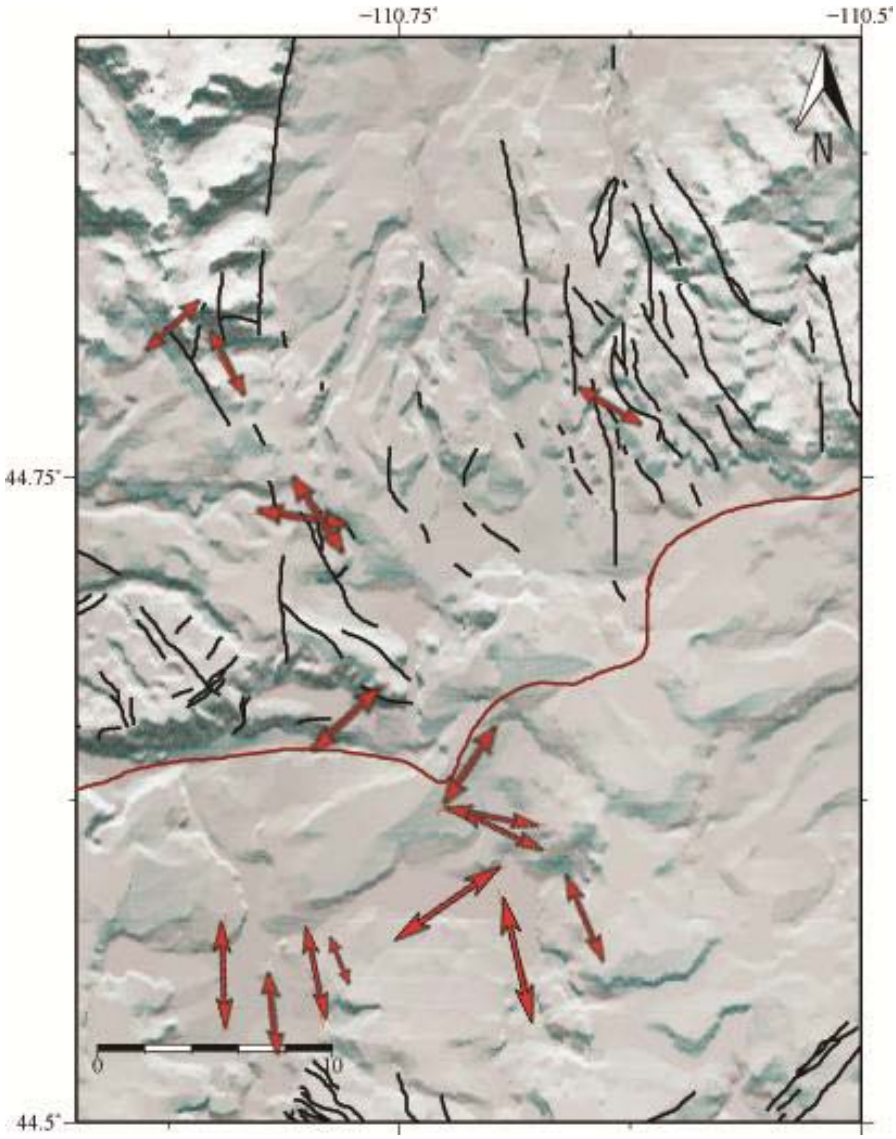

Figure A.16: Mapped orientation of T axes of focal mechanism solutions in the Norris Geyser Basin area, in the time window between 2004 and 2010 (subsidence), in a depth window between 5 and 8 km, where the proposed contracting sill is located (Chang et al., 2007), shown as red arrows. The length of the arrows represents the inclination of the axes. The 0.64 Ma Yellowstone caldera is shown as a red line, Quaternary faults are shown as black lines. The topographic data is provided by the USGS National Elevation Dataset.

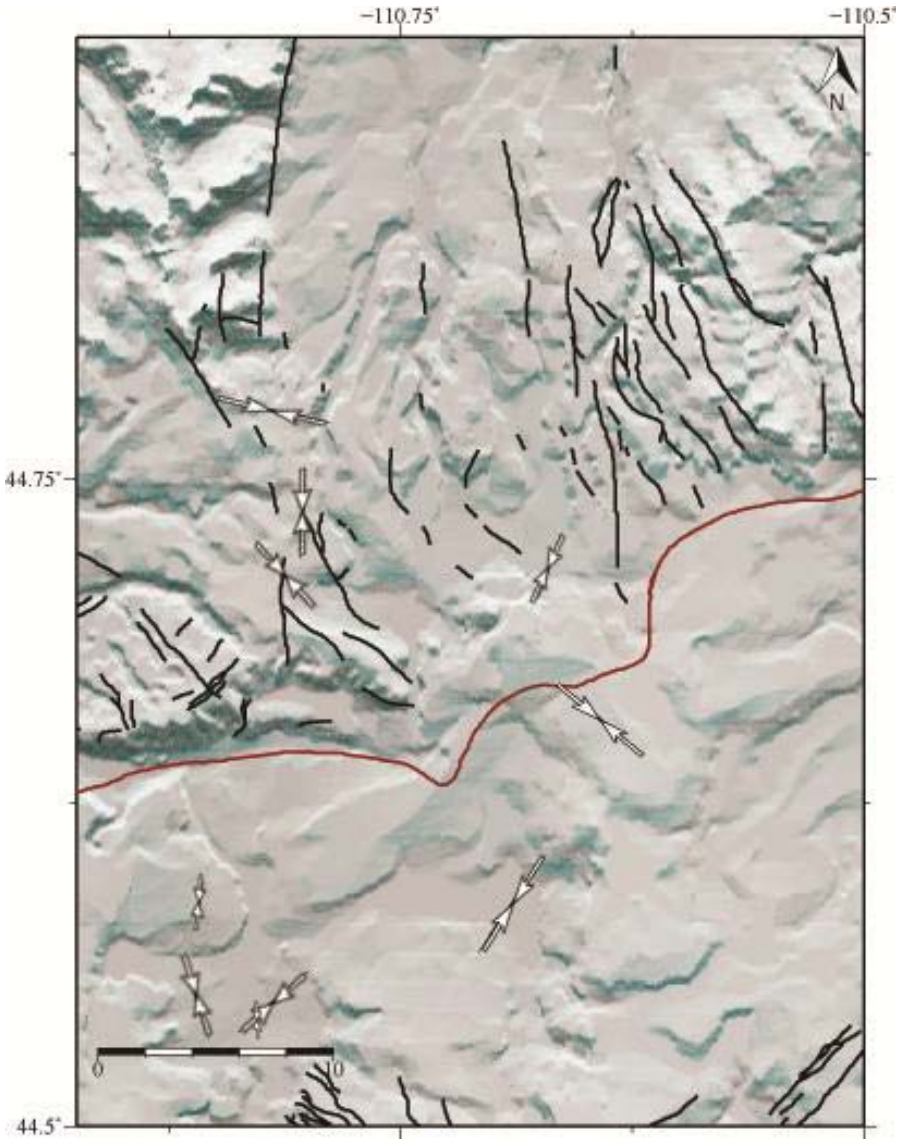

Figure A.17: Mapped orientation of P axes of focal mechanism solutions in the Norris Geyser Basin area, in the time window between 2004 and 2010 (subsidence), in a depth window below 8 km, beneath the proposed contracting sill (Chang et al., 2007), shown as white arrows. The length of the arrows represents the inclination of the axes. The 0.64 Ma Yellowstone caldera is shown as a red line, Quaternary faults are shown as black lines. The topographic data is provided by the USGS National Elevation Dataset.

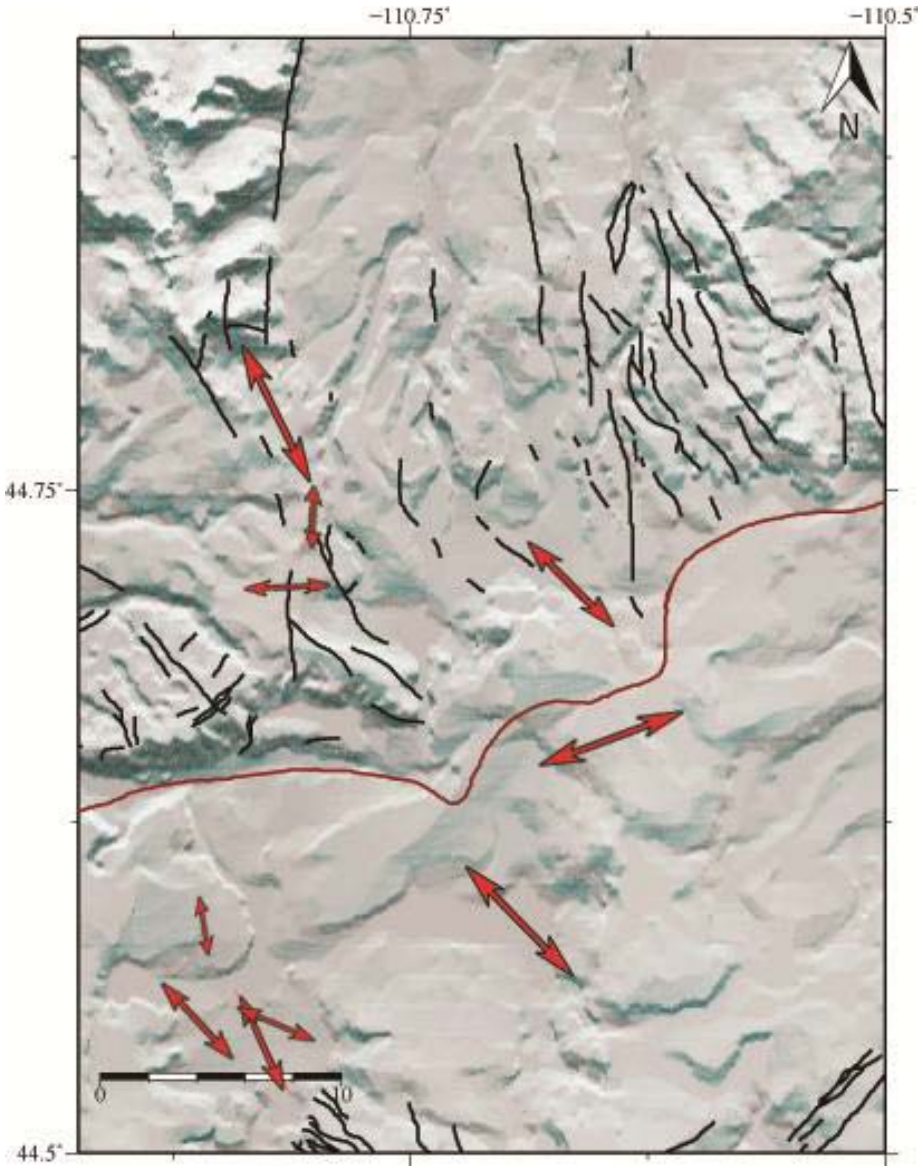

Figure A.18: Mapped orientation of T axes of focal mechanism solutions in the Norris Geyser Basin area, in the time window between 2004 and 2010 (subsidence), in a depth window below 8 km, beneath the proposed contracting sill (Chang et al., 2007), shown as red arrows. The length of the arrows represents the inclination of the axes. The 0.64 Ma Yellowstone caldera is shown as a red line, Quaternary faults are shown as black lines. The topographic data is provided by the USGS National Elevation Dataset.

APPENDIX B

P AND T AXES

WITHIN THE YELLOWSTONE CALDERA

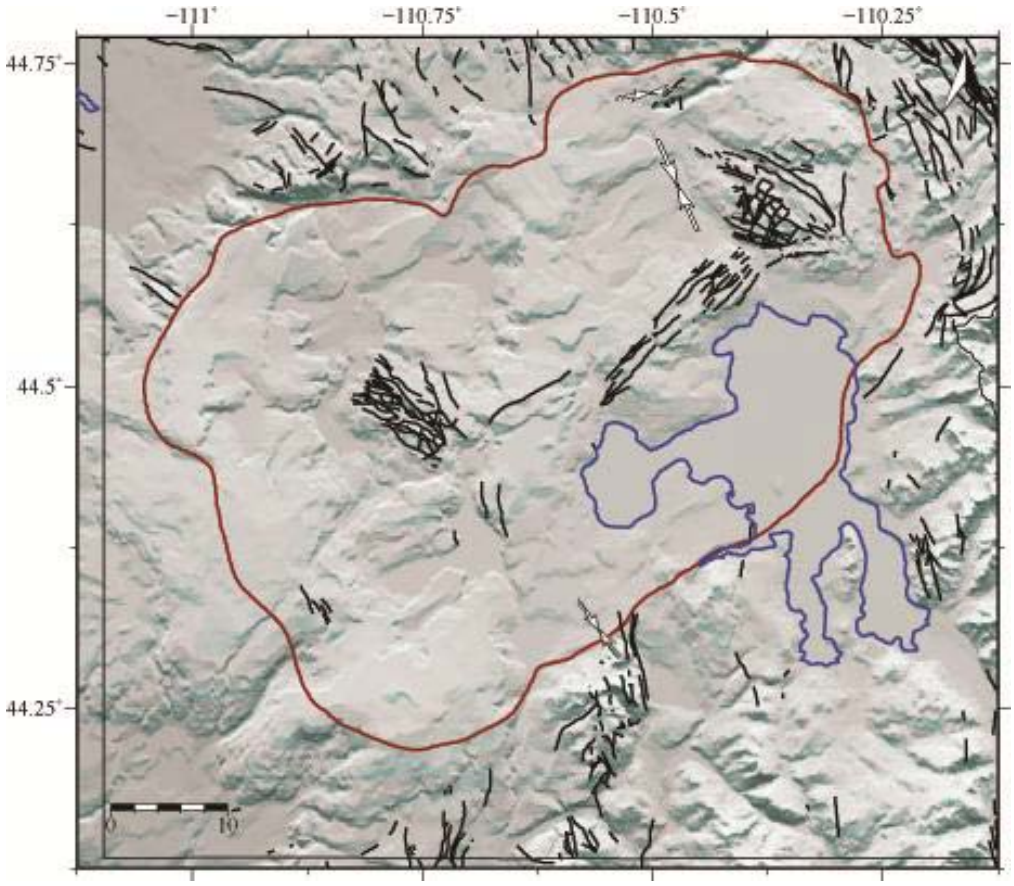

Figure B.1: Mapped orientation of P axes of focal mechanism solutions in the 0.64 Ma Yellowstone caldera, in the time window between 1988 and 1995 (subsidence stage), shown as white arrows. The length of the arrows represents the inclination of the axes. The 0.64 Ma Yellowstone caldera is shown as a red line, Quaternary faults are shown as black lines. The topographic data is provided by the USGS National Elevation Dataset.

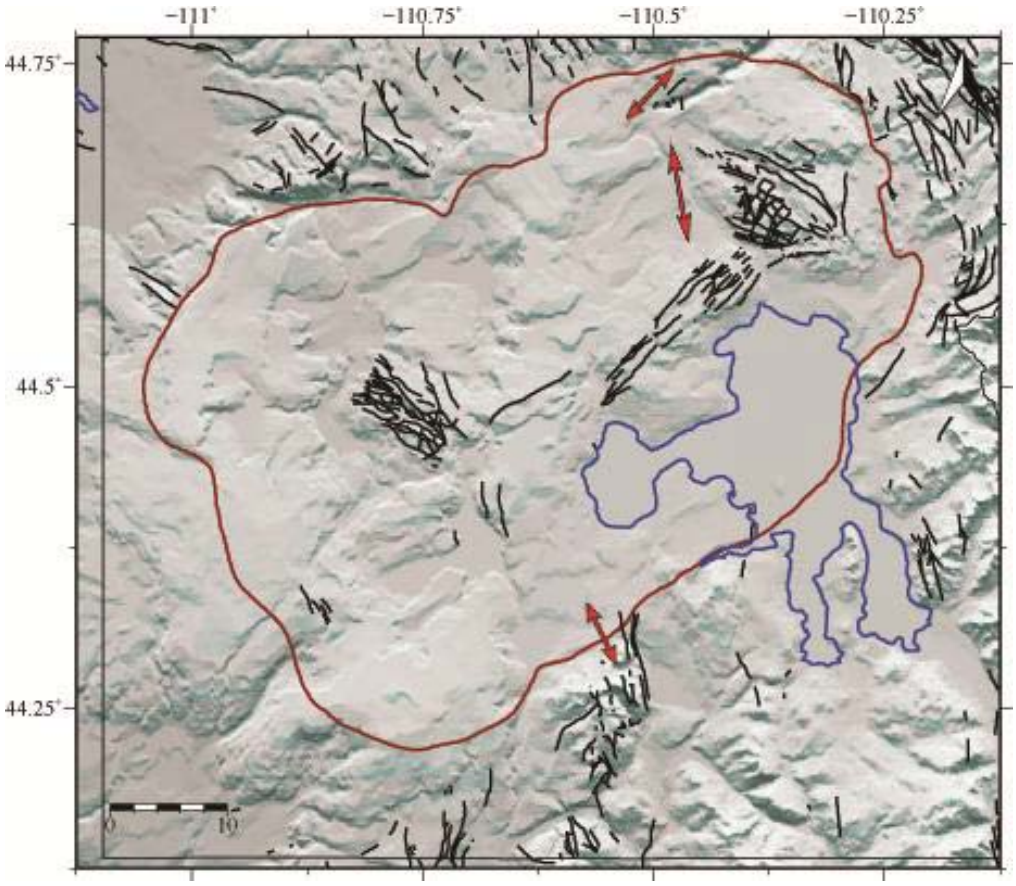

Figure B.2: Mapped orientation of T axes of focal mechanism solutions in the 0.64 Ma Yellowstone caldera, in the time window between 1988 and 1995 (subsidence stage), shown as red arrows. The length of the arrows represents the inclination of the axes. The 0.64 Ma Yellowstone caldera is shown as a red line, Quaternary faults are shown as black lines. The topographic data is provided by the USGS National Elevation Dataset.

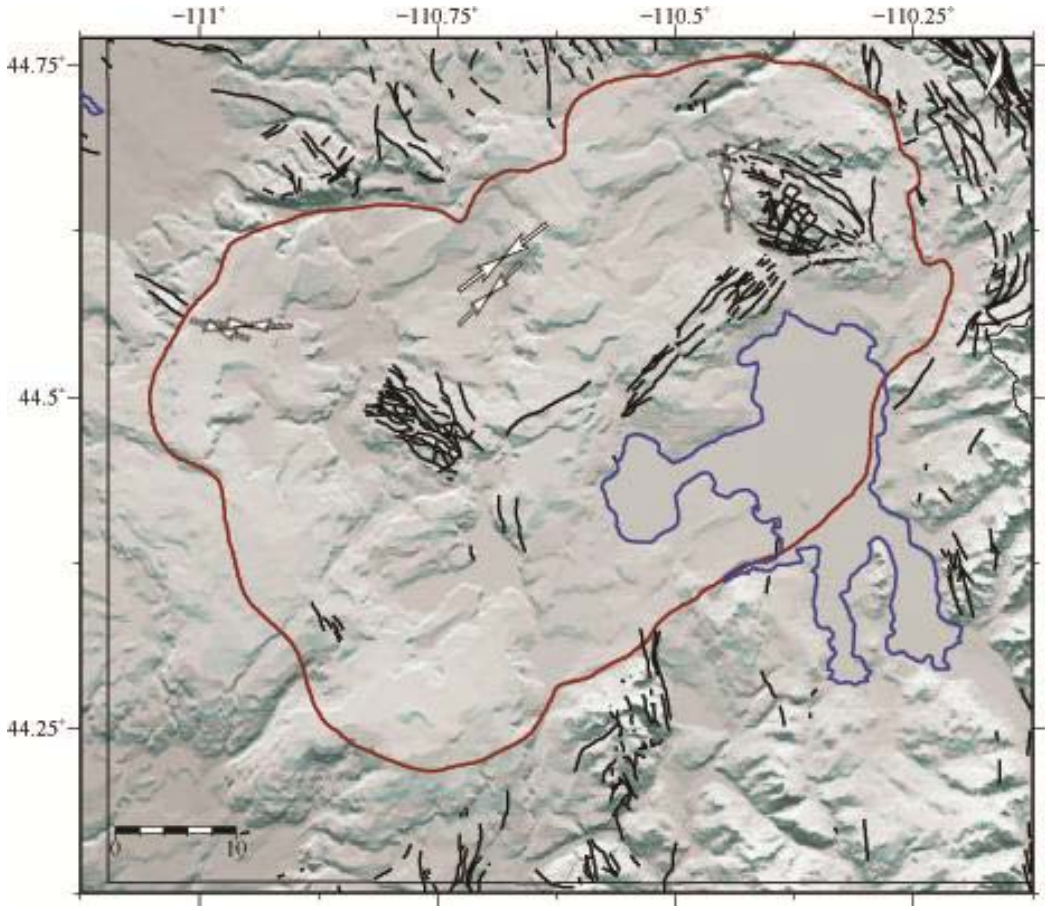

Figure B.3: Mapped orientation of P axes of focal mechanism solutions in the 0.64 Ma Yellowstone caldera, in the time window between 1995 and 2000 (uplift stage), shown as white arrows. The length of the arrows represents the inclination of the axes. The 0.64 Ma Yellowstone caldera is shown as a red line, Quaternary faults are shown as black lines. The topographic data is provided by the USGS National Elevation Dataset.

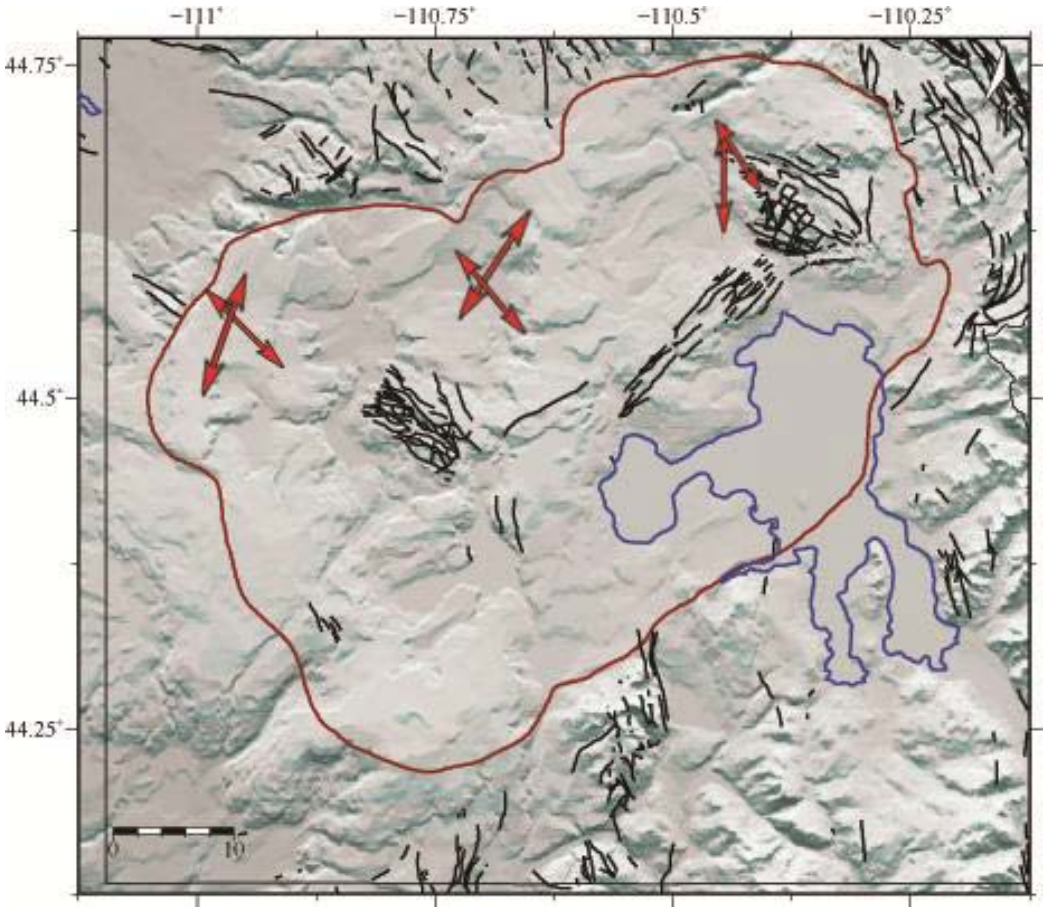

Figure B.4: Mapped orientation of T axes of focal mechanism solutions in the 0.64 Ma Yellowstone caldera, in the time window between 1995 and 2000 (uplift stage), shown as red arrows. The length of the arrows represents the inclination of the axes. The 0.64 Ma Yellowstone caldera is shown as a red line, Quaternary faults are shown as black lines. The topographic data is provided by the USGS National Elevation Dataset.

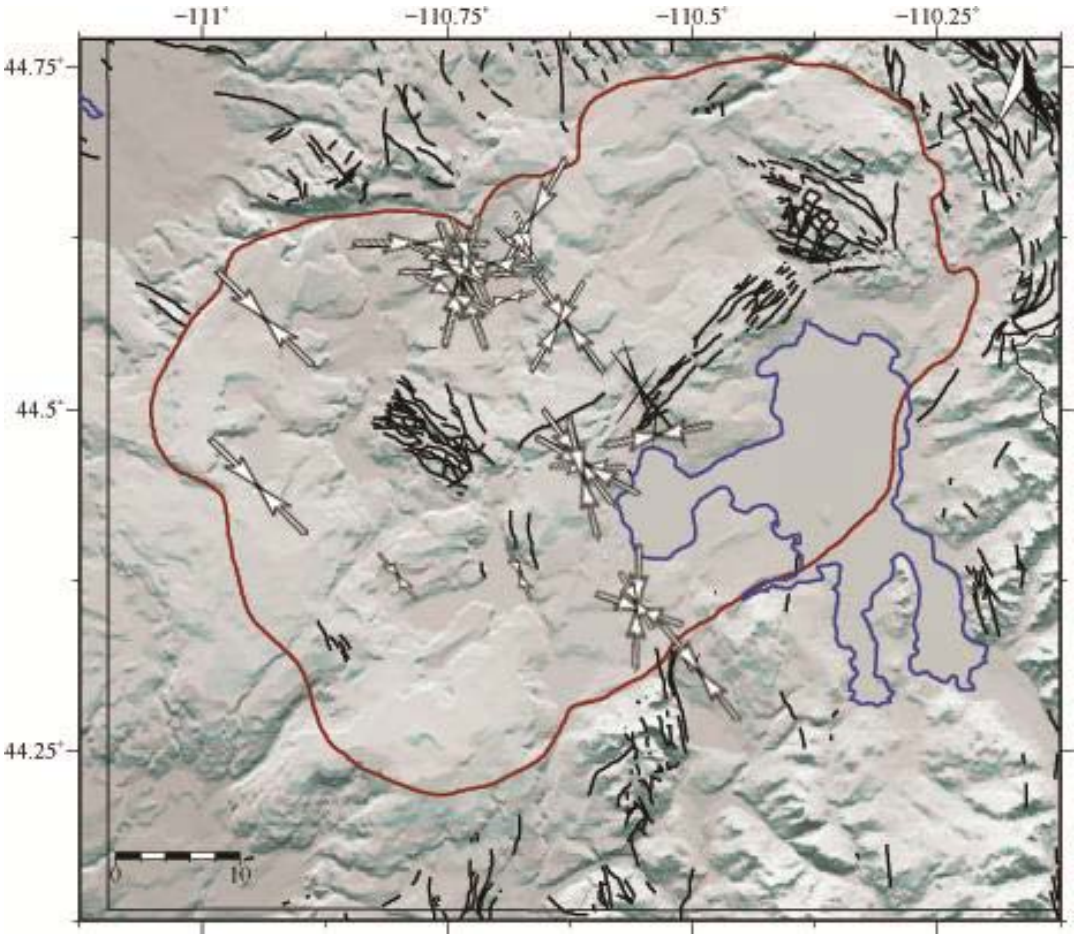

Figure B.5: Mapped orientation of P axes of focal mechanism solutions in the 0.64 Ma Yellowstone caldera, in the time window between 2000 and 2004 (subsidence stage), shown as white arrows. The length of the arrows represents the inclination of the axes. The 0.64 Ma Yellowstone caldera is shown as a red line, Quaternary faults are shown as black lines. The topographic data is provided by the USGS National Elevation Dataset.

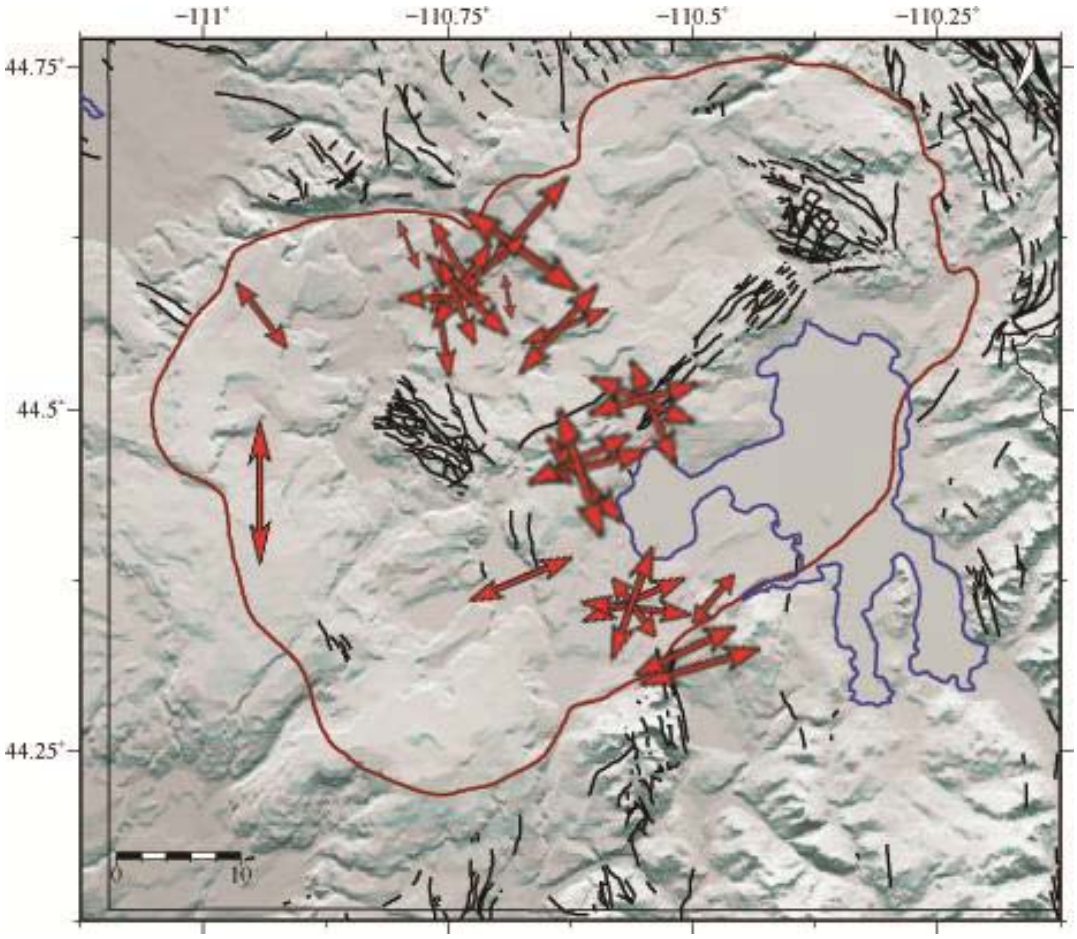

Figure B.6: Mapped orientation of T axes of focal mechanism solutions in the 0.64 Ma Yellowstone caldera, in the time window between 2000 and 2004 (subsidence stage), shown as red arrows. The length of the arrows represents the inclination of the axes. The 0.64 Ma Yellowstone caldera is shown as a red line, Quaternary faults are shown as black lines. The topographic data is provided by the USGS National Elevation Dataset.

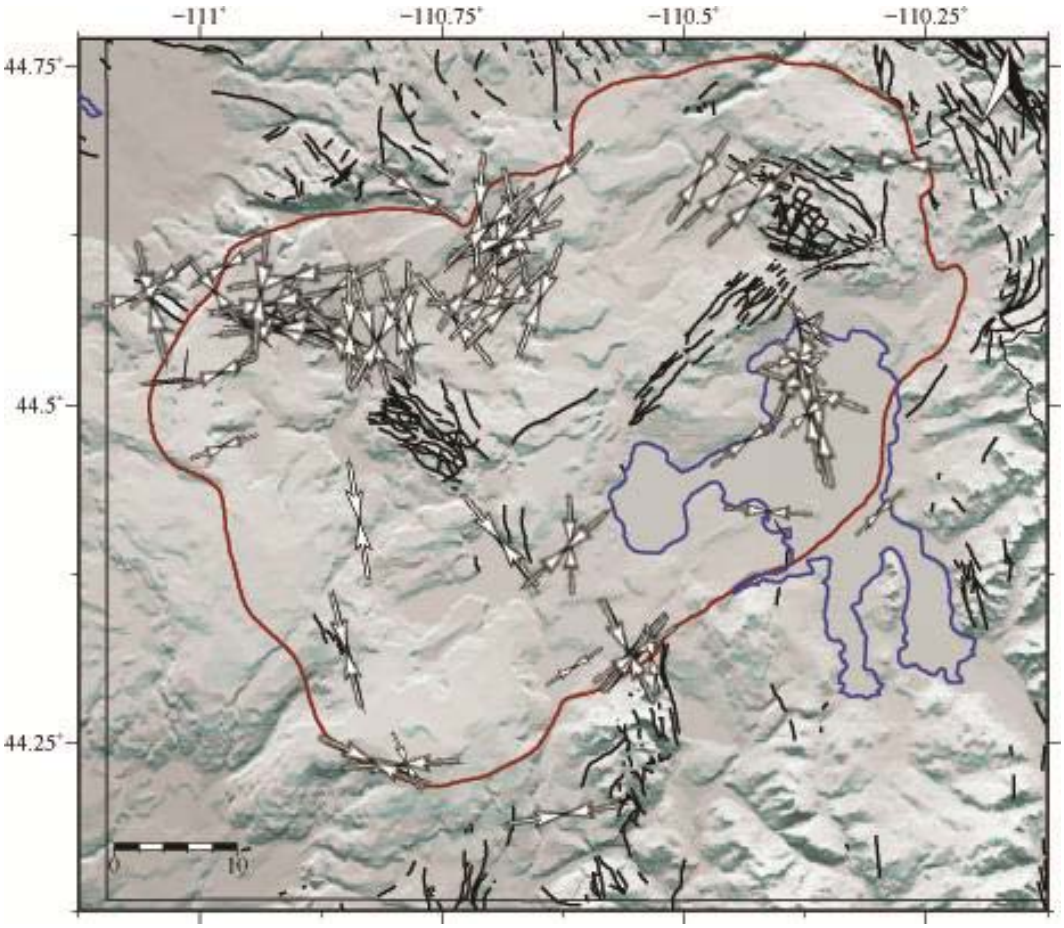

Figure B.7: Mapped orientation of P axes of focal mechanism solutions in the 0.64 Ma Yellowstone caldera, in the time window between 2004 and 2010 (uplift stage), shown as white arrows. The length of the arrows represents the inclination of the axes. The 0.64 Ma Yellowstone caldera is shown as a red line, Quaternary faults are shown as black lines. The topographic data is provided by the USGS National Elevation Dataset.

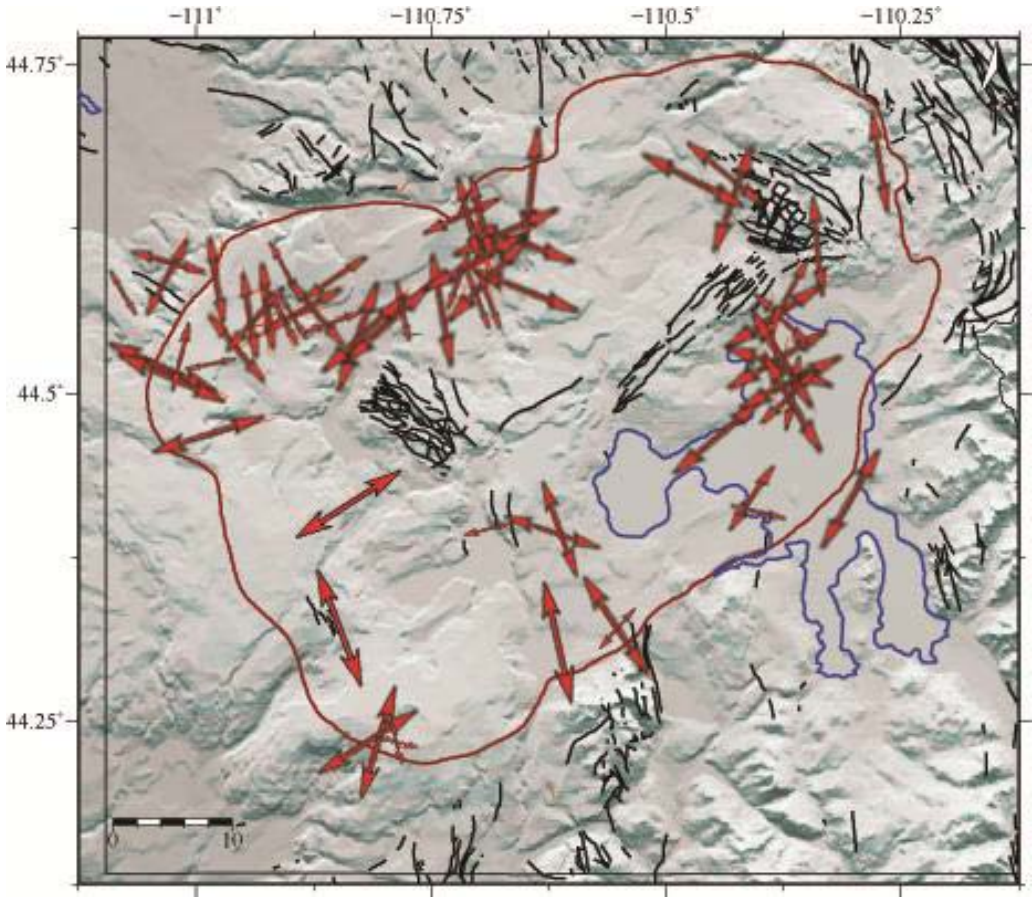

Figure B.8: Mapped orientation of T axes of focal mechanism solutions in the 0.64 Ma Yellowstone caldera, in the time window between 2004 and 2010 (uplift stage), shown as red arrows. The length of the arrows represents the inclination of the axes. The 0.64 Ma Yellowstone caldera is shown as a red line, Quaternary faults are shown as black lines. The topographic data is provided by the USGS National Elevation Dataset.

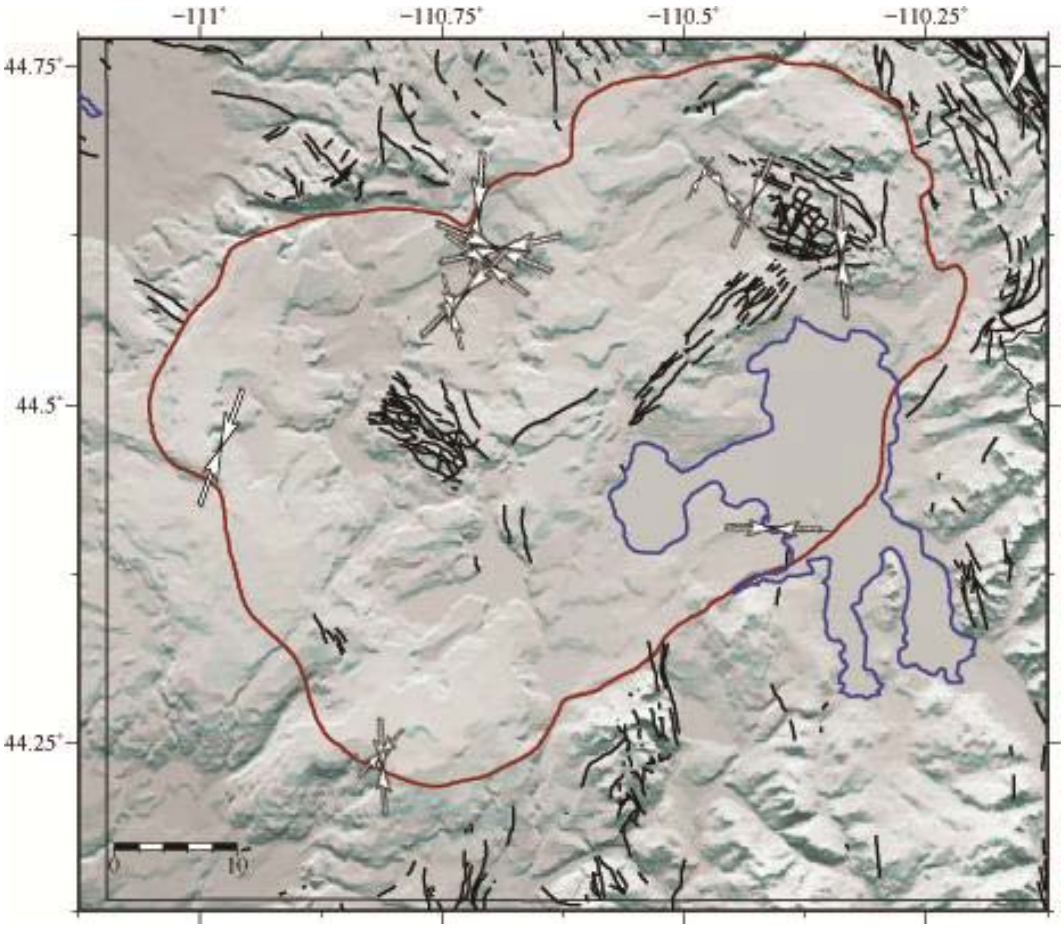

Figure B.9: Mapped orientation of P axes of focal mechanism solutions in the 0.64 Ma Yellowstone caldera, in the time window between 2004 and 2010 (uplift stage), in the depth window between 0 and 7 km, above the sill proposed by Chang et al. (2007), shown as white arrows. The length of the arrows represents the inclination of the axes. The 0.64 Ma Yellowstone caldera is shown as a red line, Quaternary faults are shown as black lines. The topographic data is provided by the USGS National Elevation Dataset.

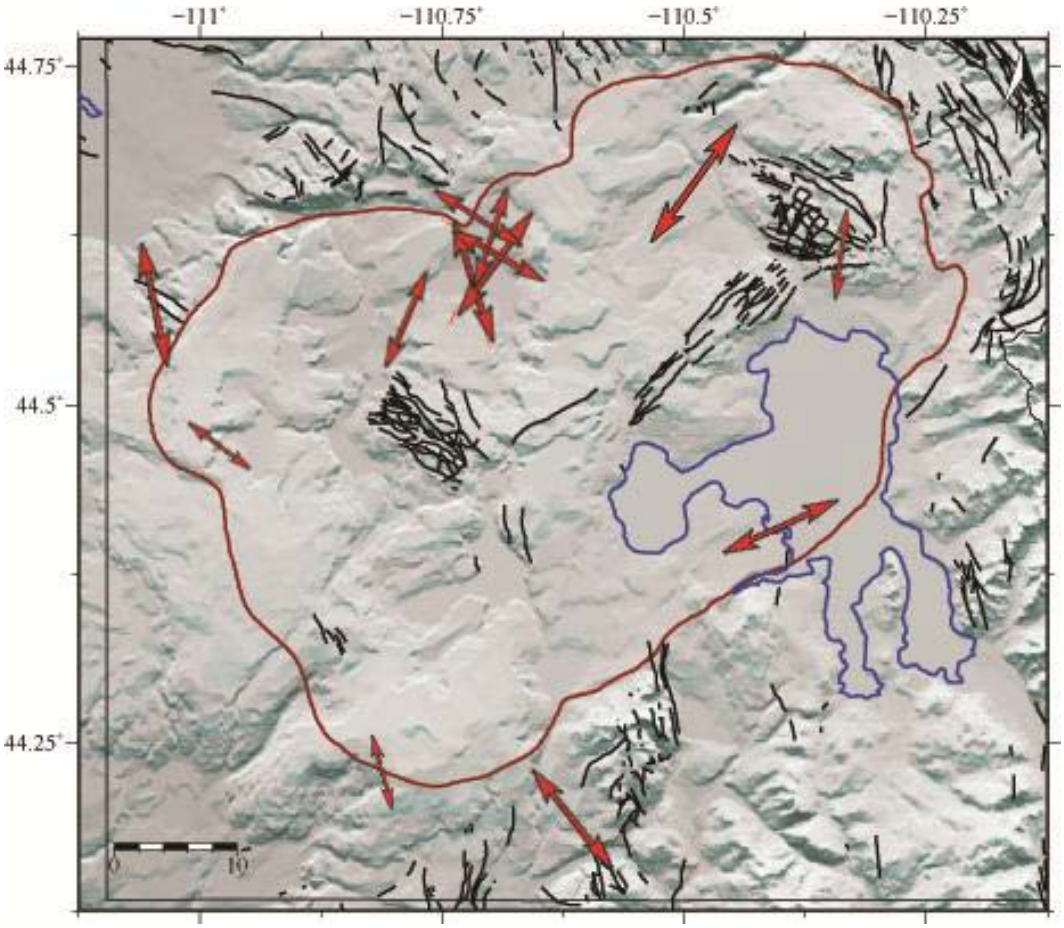

Figure B.10: Mapped orientation of T axes of focal mechanism solutions in the 0.64 Ma Yellowstone caldera, in the time window between 2004 and 2010 (uplift stage), in the depth window between 0 and 7 km, above the sill proposed by Chang et al. (2007), shown as red arrows. The length of the arrows represents the inclination of the axes. The 0.64 Ma Yellowstone caldera is shown as a red line, Quaternary faults are shown as black lines. The topographic data is provided by the USGS National Elevation Dataset.

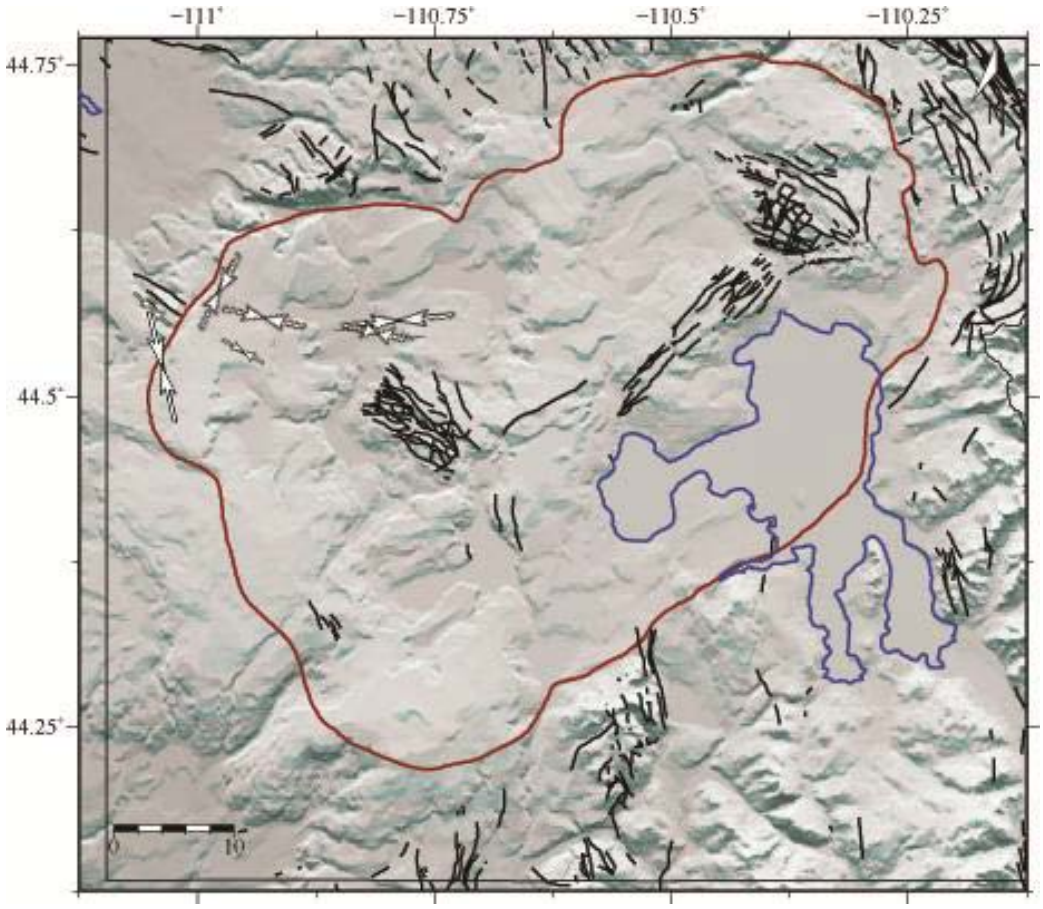

Figure B.11: Mapped orientation of P axes of focal mechanism solutions in the 0.64 Ma Yellowstone caldera, in the time window between 2004 and 2010 (uplift stage), in the depth window between 7 and 11 km, where the sill proposed by Chang et al. (2007) is located, shown as white arrows. The length of the arrows represents the inclination of the axes. The 0.64 Ma Yellowstone caldera is shown as a red line, Quaternary faults are shown as black lines. The topographic data is provided by the USGS National Elevation Dataset.

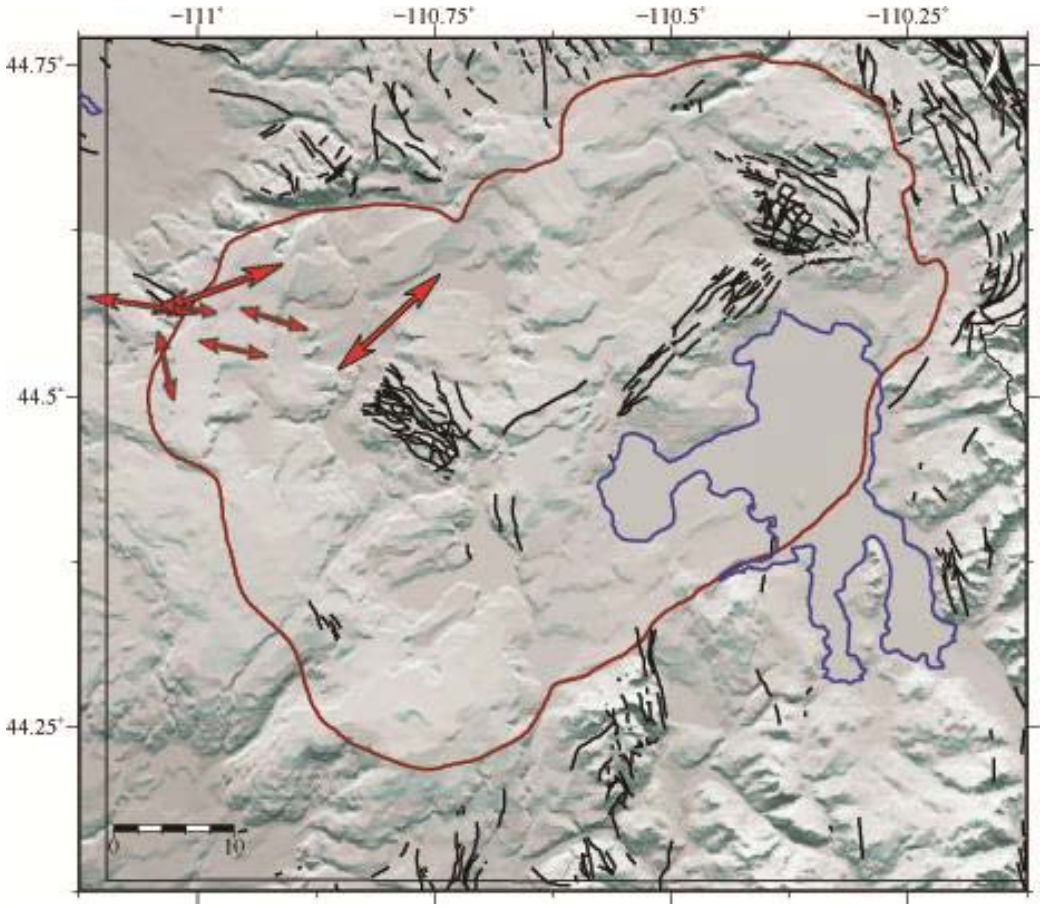

Figure B.12: Mapped orientation of minimum compressive stress (T) of focal mechanism solutions in the 0.64 Ma Yellowstone caldera, in the time window between 2004 and 2010 (uplift stage), in the depth window between 7 and 11 km, where the sill proposed by Chang et al. (2007) is located, shown as red arrows. The length of the arrows represents the inclination of the axes. The 0.64 Ma Yellowstone caldera is shown as a red line, Quaternary faults are shown as black lines. The topographic data is provided by the USGS National Elevation Dataset.

APPENDIX C

FOCAL MECHANISM SOLUTIONS WITH POLARITIES

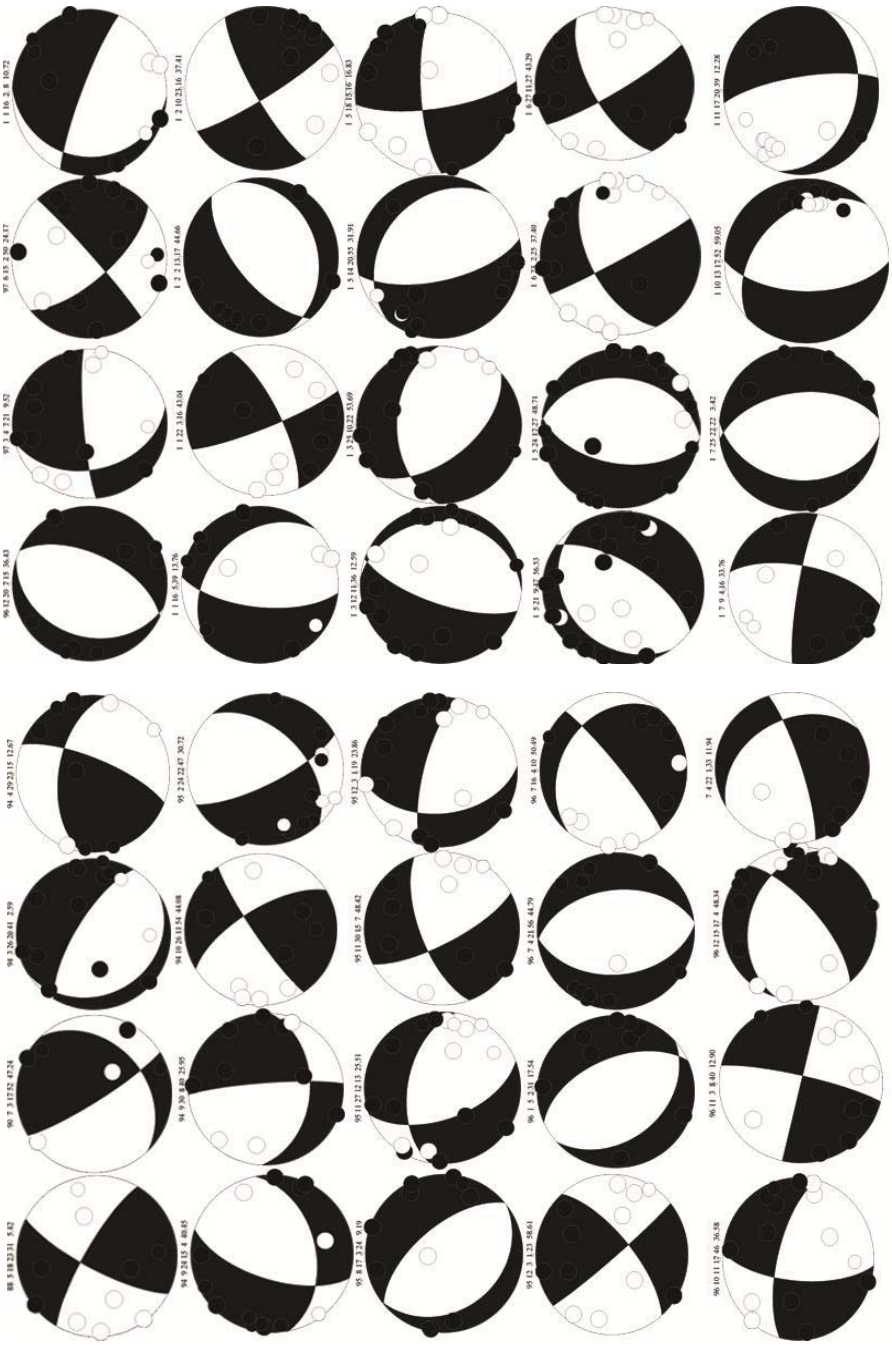

Figure C.1: Focal mechanism solutions, plotted with polarities.

Figure C.2: Focal mechanism solutions, plotted with polarities.

Figure C.3: Focal mechanism solutions, plotted with polarities.

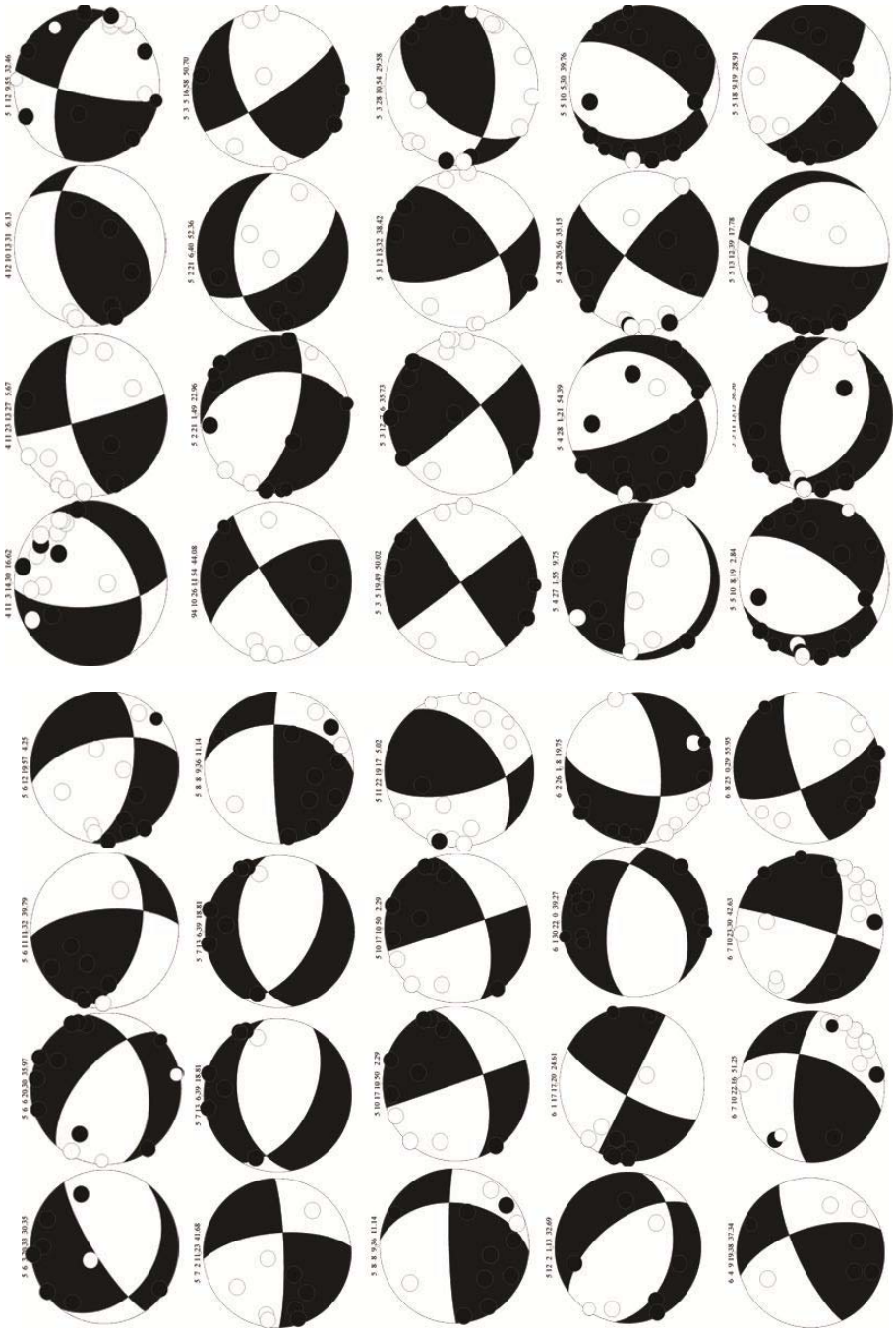

Figure C.4: Focal mechanism solutions, plotted with polarities.

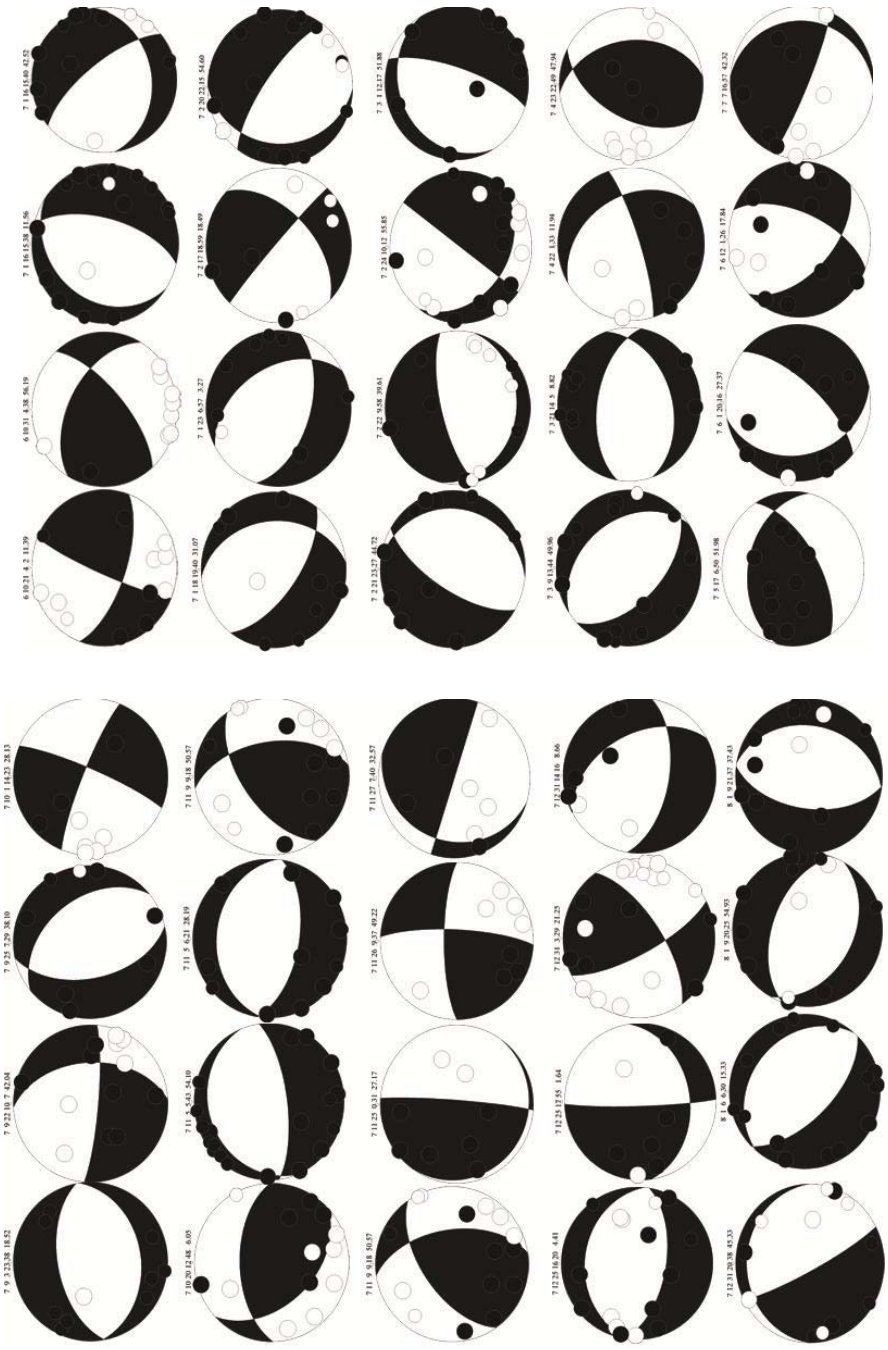

Figure C.5: Focal mechanism solutions, plotted with polarities.

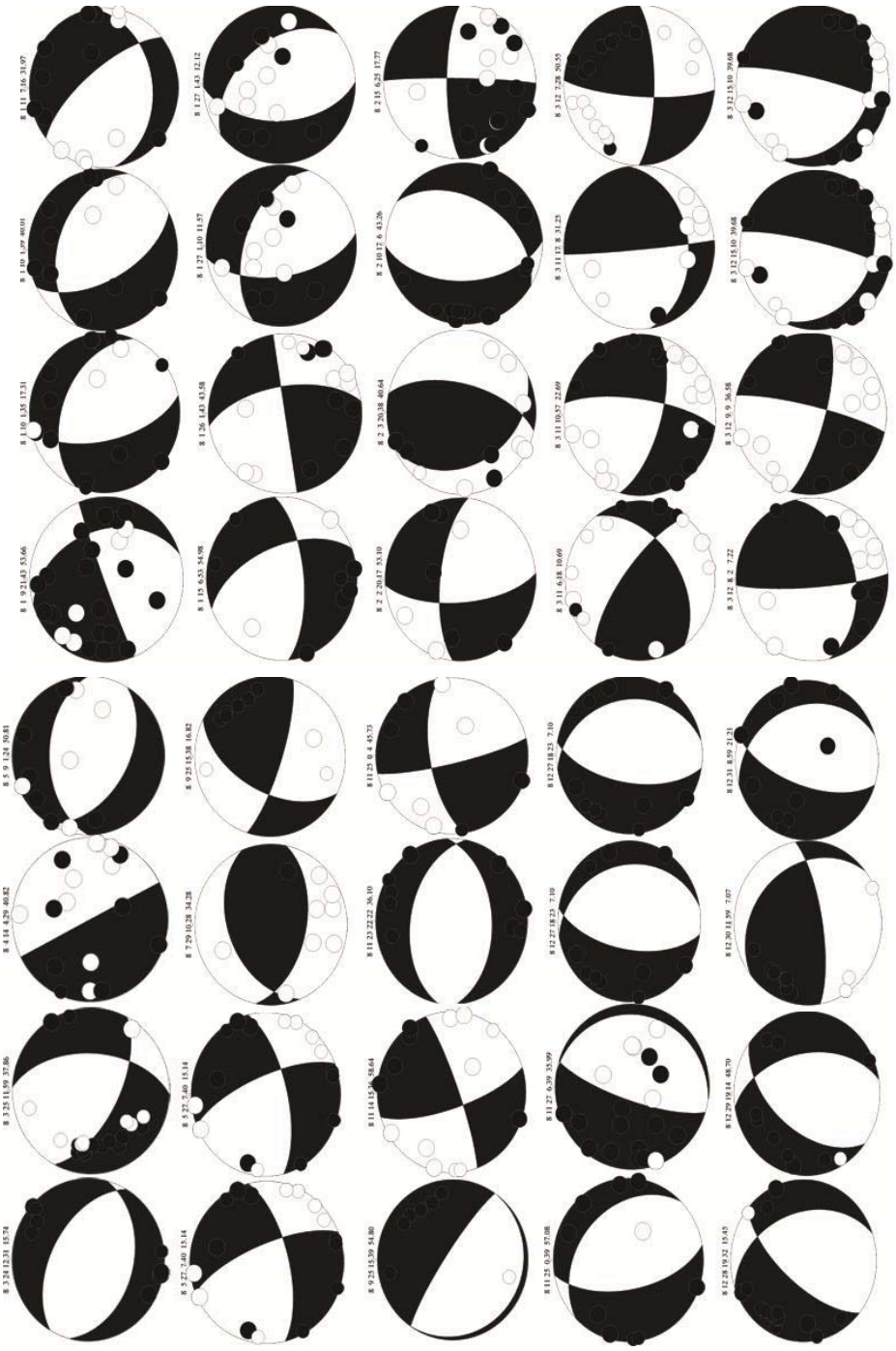

Figure C.6: Focal mechanism solutions, plotted with polarities.

Figure C.7: Focal mechanism solutions, plotted with polarities.

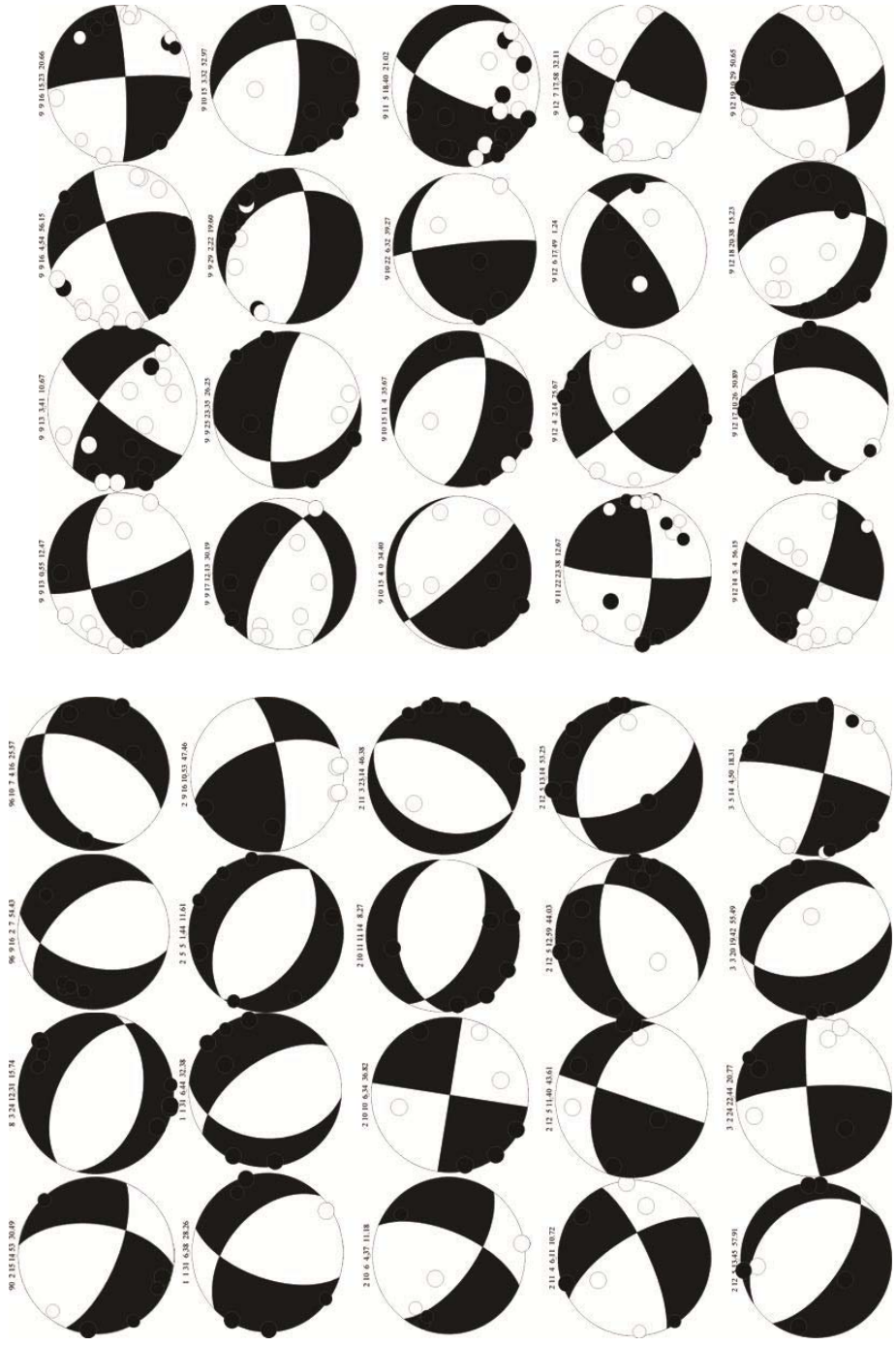

Figure C.8: Focal mechanism solutions, plotted with polarities.

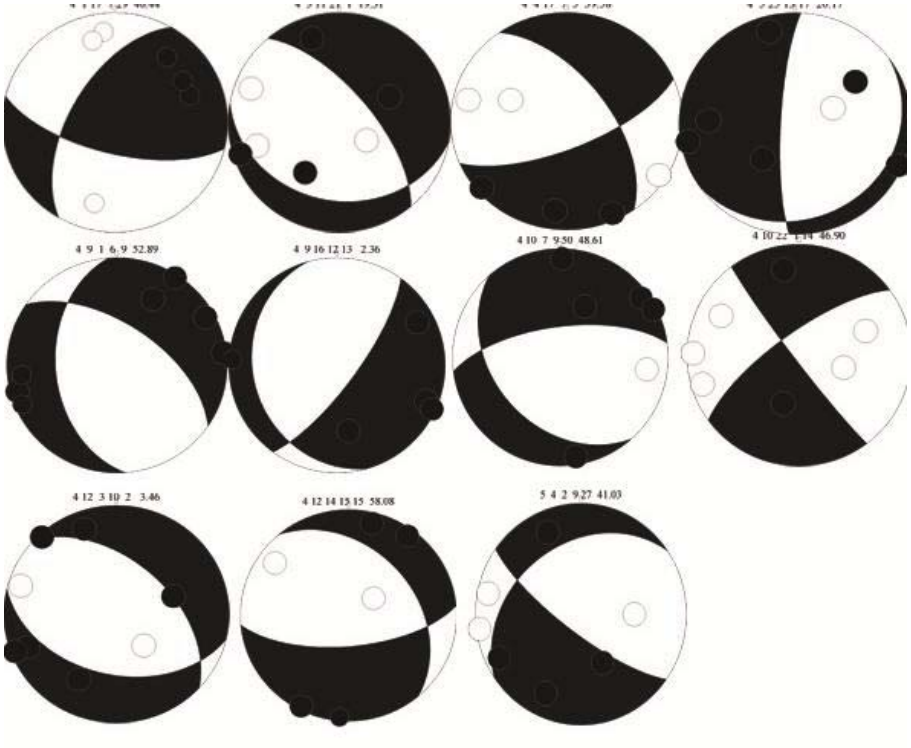

Figure C.9: Focal mechanism solutions, plotted with polarities, represented as black and white circles. Above each focal mechanism, the date, hour, minute and seconds of the event are indicated.

APPENDIX D

MODEL STRESS-FIELD SOLUTIONS

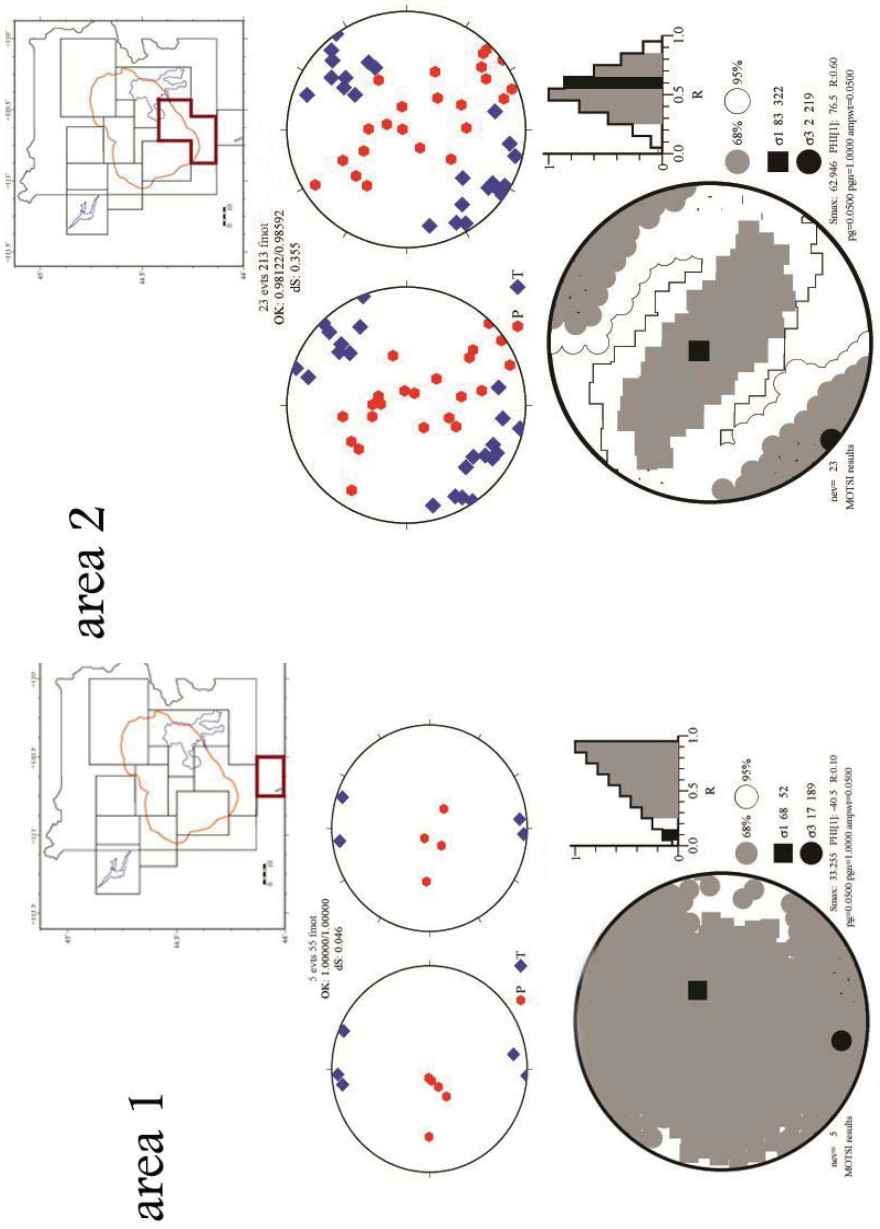

Figure D.1: Model stress-field solutions for areas 1 and 2, outlined in red in the map.

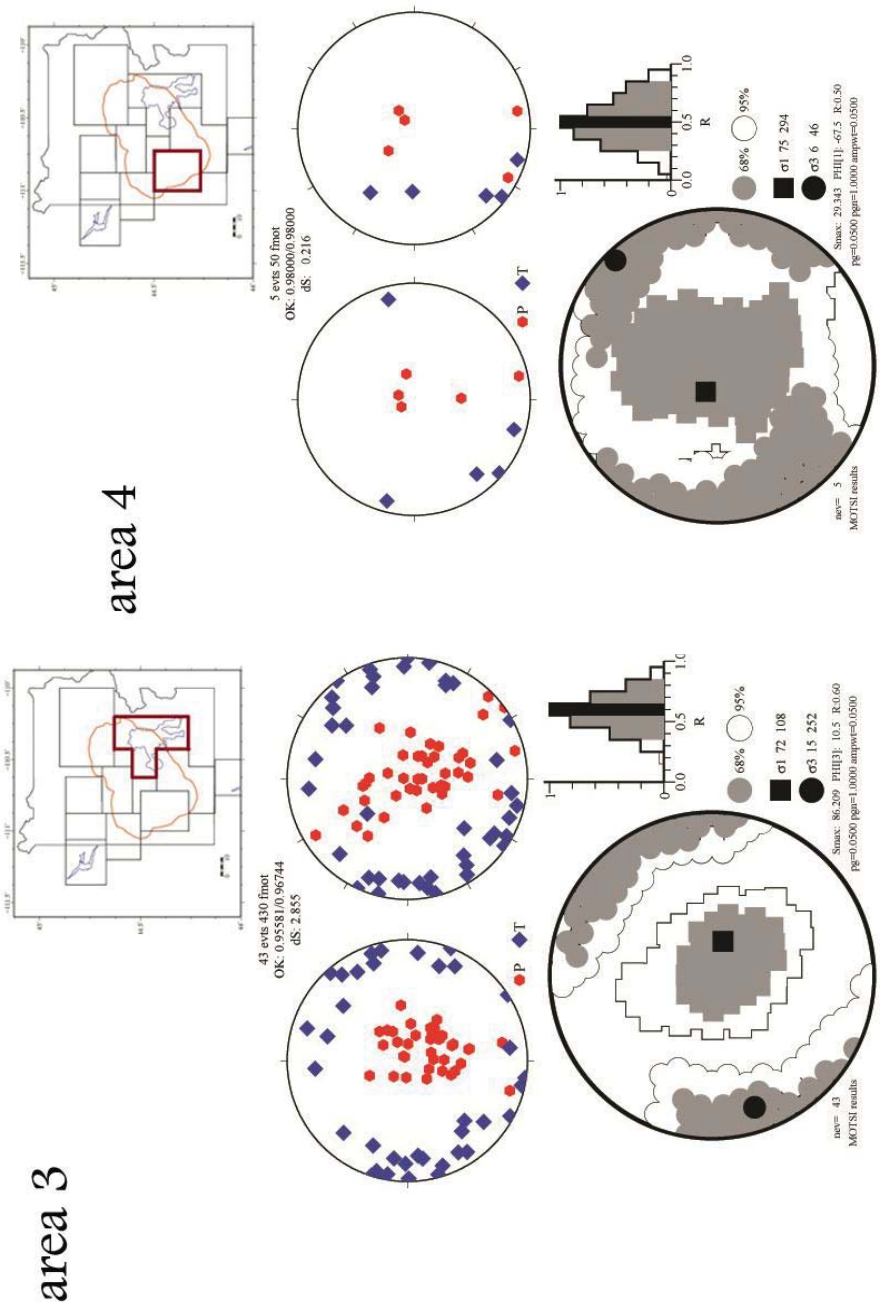

Figure D.2: Model stress-field solutions for areas 3 and 4, outlined in red in the map.

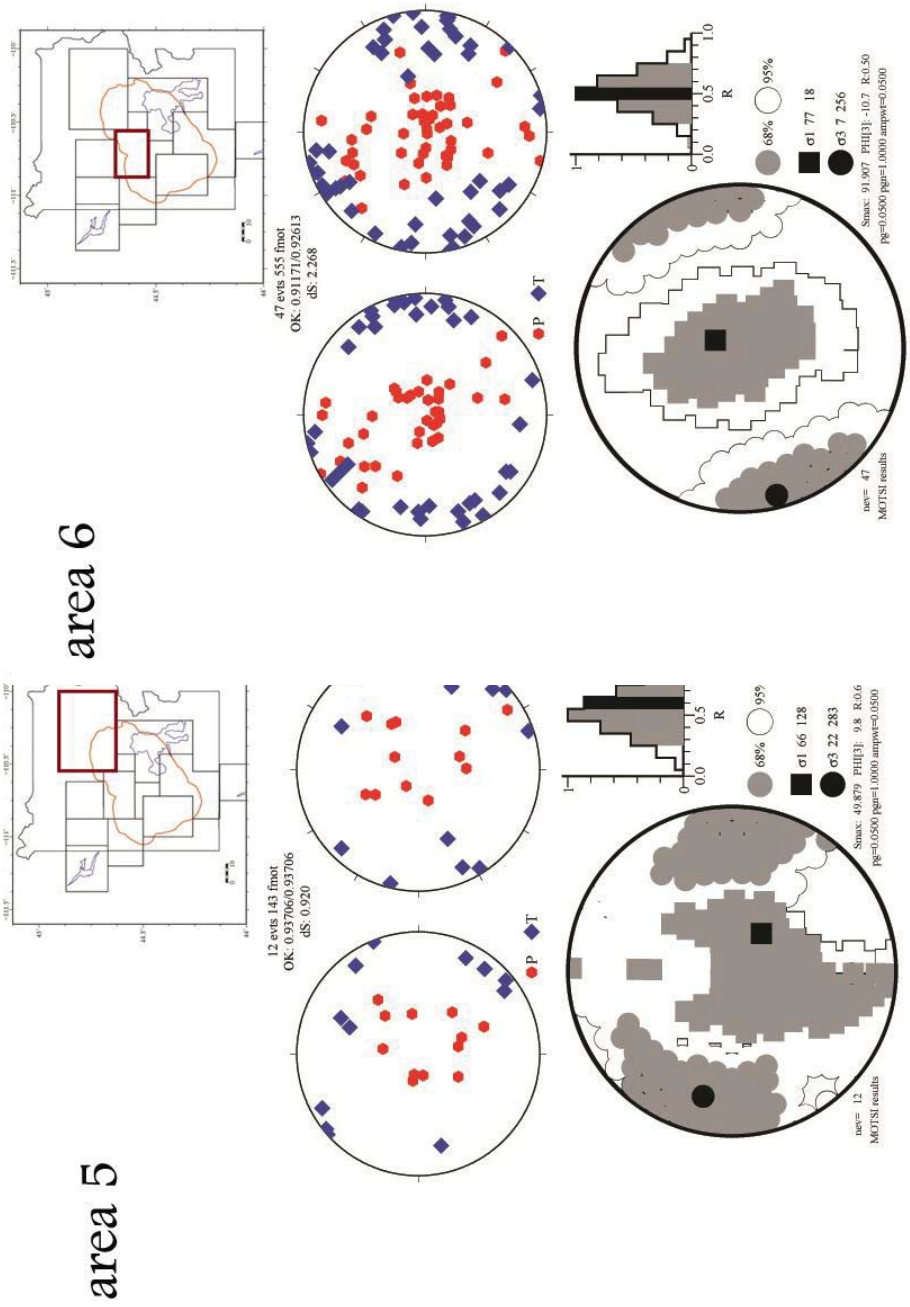

Figure D.3: Model stress-field solutions for areas 5 and 6, outlined in red in the map.

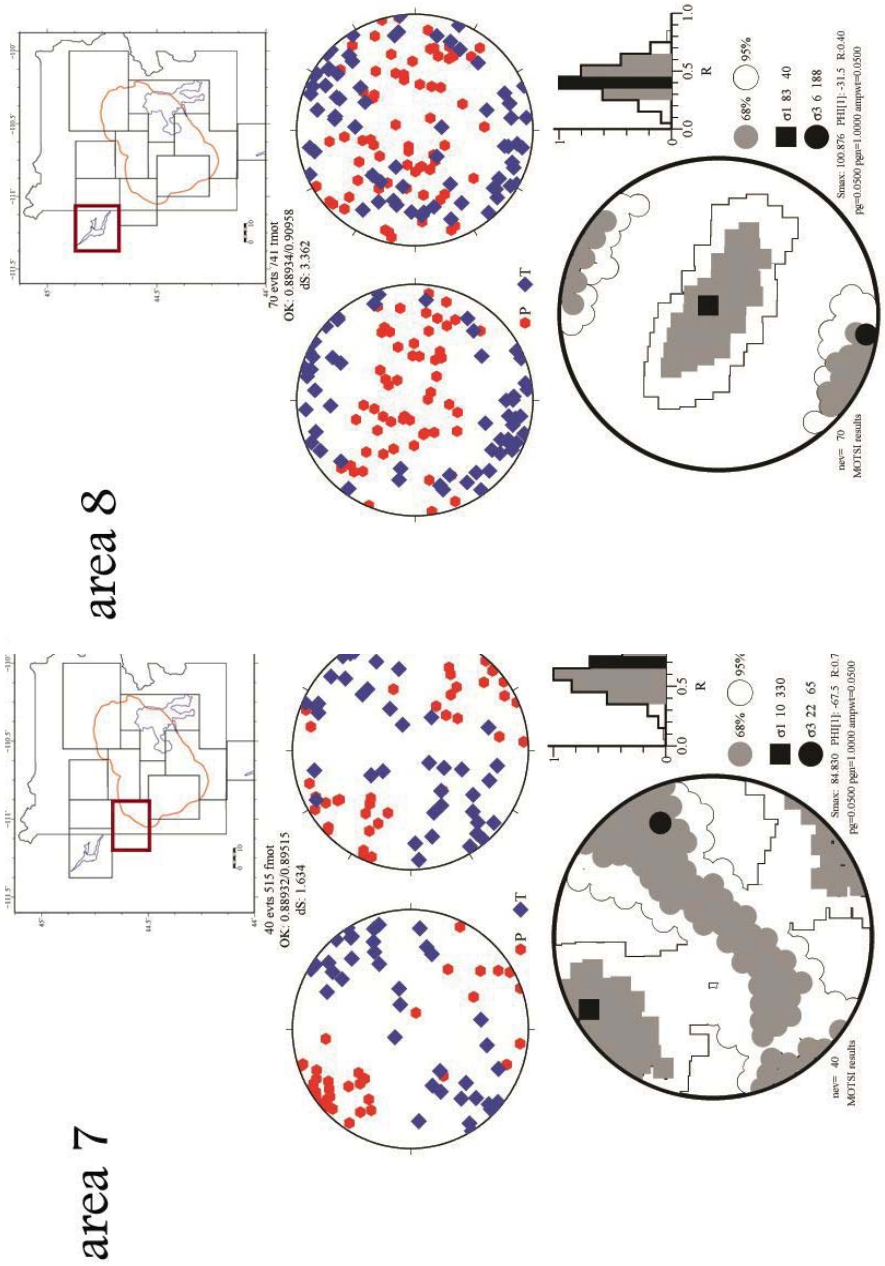

Figure D.4: Model stress-field solutions for areas 7 and 8, outlined in red in the map.

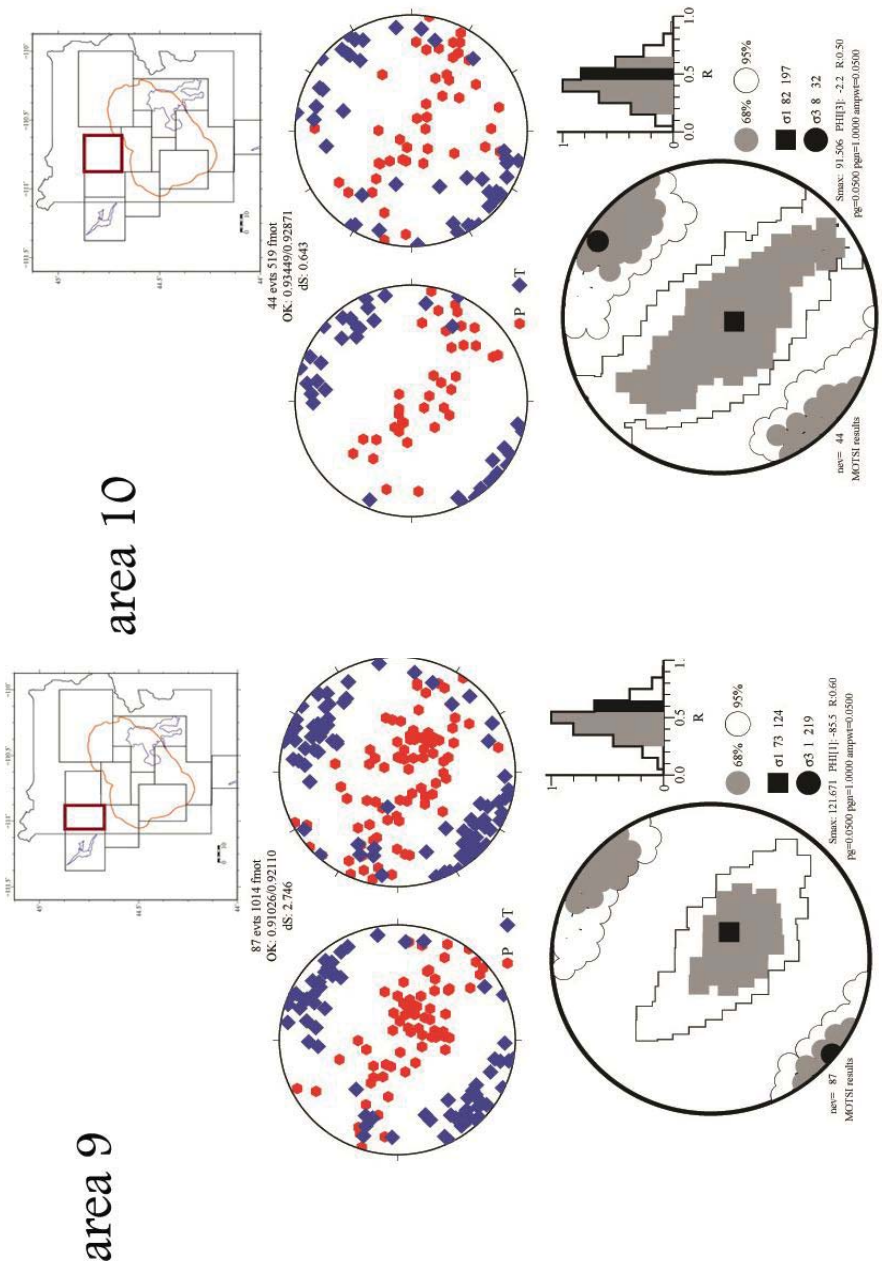

Figure D.5: Model stress-field solutions for areas 9 and 10, outlined in red in the map.

BIBLIOGRAPHY

Abers, G.A. and Gephart, J.W., Direct inversion of earthquake first motions for both the stress tensor and focal mechanisms and application to southern California, *J. Geophys. Res*., 106, 2001.

Anders, M.H., D.W. Rodgers, S.R. Hemming, J. Saltzman, V.J. DiVinere, J.T. Hagstrum, G.F. Embree, and R.C. Walter, A fixed sub-lithospheric source for the late Neogene track of the Yellowstone hotspot: Implications of the Heise and Picabo Volcanic Fields, *J. Geophys. Res.*, in press, 2014.

Angelier, J*.,* Tectonic analysis of fault slip data sets*, J. Geophys. Res., 89(*B7*),* 5835–5848, 1984

Armstrong, R.L., W.P. Leeman, and H.E. Malde, K-Ar dating, Quaternaty and Neogene volcanic rocks of the Snake River Plain, Idaho, *Am. J. Sc.*, 275, 225-251, 1975.

Battaglia, M., C. Troise , F. Obrizzo, F. Pingue, and G. De Natale, Evidence for fluid migration as the source of deformation at Campi Flegrei caldera (Italy), *Geophys. Res. Lett*., 33, L01307, 2006.

Bennett, R.A., J.L. Davis, J.E. Normandeau, and B.P. Wernicke, Space geodetic measurements of plate boundary deformation in the western U.S. Cordillera, in Plate Boundary Zones, *Geodyn. Ser.*, vol. 30, 2001.

Benz, H.M., and R.B. Smith, Simultaneous inversion for lateral velocity variations and hypocenters in the Yellowstone region using earthquake and refraction data, *J. Geophys. Res.*, 89, 1208-1220, 1984.

Chang, W.L., Smith, R.B., Wicks, C. Farrell, J. M., Puskas, C.M., Accelerated uplift and magmatic intrusion of the Yellowstone caldera, 2004 to 2006, *Science*, 318, 952, 2007.

Chang, W.L., Smith, R.B., Farrell, J., Puskas, C.M., An extraordinary episode of Yellowstone caldera uplift, 2004-2010, from GPS and InSAR observations, *Geophysical Research Letters*, vol. 37, 2010.

Christiansen, R.L., and H.R. Blank Jr., Volcanic stratigraphy of the Quaternary Rhyolite Plateau in Yellowstone National Park, *U.S. Geol. Surv. Prof. Pap.*, 729-B, 18 pp, 1972.

Christiansen, R.L., Yellowstone magmatic evolution: its bearing on understanding large volume explosive volcanism, in *Explosive Volcanism: Inception, Evolution and Hazards*, pp. 84-95, National Academy Press, Washington, D.C., 1984.

Christiansen, R. L., The Quaternary and Pliocene Yellowstone plateau volcanic field of Wyoming, Idaho and Montana, *U.S. Geol. Surv. Profess. Pap.*, 729-G, 145, 2001.

Christiansen, R.L., J.B. Lowenstern, R.B. Smith, H.Heasler, L.A. Morgan, M. Nathenson, L. G. Mastin, L.J.P. Muffler, and J. E. Robinson, Preliminary assessment of volcanic and hydrothermal hazards in Yellowstone National Park and Vicinity, *U.S. Geological Survey, Open-file Report 2007-1071*, 94 pp, 2007.

DeNosaquo, K., R.B. Smith, and A.R. Lowry, Density and lithospheric strength models of the Yellowstone-Snake River Plain volcanic system from gravity and heat flow data, *J. Volcanol. Geotherm. Res.*, 188, 108-127, 2009.

Doser, D.I., Source parameters and faulting processes of the 1959 Hebgen Lake, Montana, earthquake sequence, *J. Geophys. Res.*, 90 (B6), 4537-4555, 1985.

Dzurisin, D., J.C. Savage, and R.O. Fournier, Recent crustal subsidence at Yellowstone Caldera, Wyoming, *Bull. Volcanol.*, 52, 247-270, 1990.

Dzurisin, D., K.M. Yamashita, and J.W. Kleinman, Mechanisms of crustal uplift and subsidence at the Yellowstone caldera, Wyoming, *Bull. Volcanol.*, 56, 261-270, 1994.

Eddington, P.K., R.B. Smith, and C. Renggli, Kinematics of Basin and Range intraplate extension, in *Continental Extensional Tectonics*, edited by M.P. Coward, J.F. Dewey, and P.L. Hancock, pp. 371-392, Blackwell Sci., Malden, Mass, 1987.

Farrell, J., S. Husen, and R.B. Smith, Earthquake swarm and b-value characterization of the Yellowstone volcano-tectonic system, *J. Volcanol. Geotherm. Res.*, 188, 260-276, 2009.

Farrell, J., R. B. Smith, T. Taira, W. L. Chang, and C.M. Puskas, Dynamics and rapid migration of the energetic 2008-2009 Yellowstone Lake earthquake swarm, *Geophys. Res. Lett*., 37, 2010.

Farrell, J., Smith, R.B., Husen, S., Diehl, T., Tomography from twenty-six years of seismicity reveals the spatial extent of the Yellowstone crustal magma reservoir extends well beyond the Yellowstone caldera, University of Utah Dept. of Geology and Geophysics, Salt Lake City, 2014.

Fournier, R.O., D.E. White, and A.H. Truesdell, Convective heat flow in Yellowstone National Park, in *Second United Nations Symposium on Development and Use of Geothermal Resources*, pp. 731-739, U.S. Govt. Print. Off., Washington D.C., 1976.

Fournier, R. O., Geochemistry and dynamics of the Yellowstone National Park hydrothermal system, *Annu. Rev. Eart Planet. Sci.*, 17, 13-53, 1989.

Gephart, J. W.*, and* D. W. Forsyth*,* An improved method for determining the regional stress tensor using earthquake focal mechanism data: Application to the San Fernando Earthquake Sequence*, J. Geophys. Res*.*,* 89*(*B11*),* 9305–9320*, 1984.*

Hardebeck, J.L. Homogeneity of small-scale earthquake faulting, stress, and fault strength, *Bull. Seismol. Soc. Am*., vol. 96 no.5, 1675-1688, 2006.

Hardebeck, J.L., and P.M. Shearer, A new method for determining first-motion focal mechanisms, *Bull. Seismol. Soc. Am.*, 92, 2264-2276, 2002.

Hardebeck, J.L., and P.M. Shearer, Using S/P amplitude ratios to constrain the focal mechanisms of small earthquakes, *Bull. Seismol. Soc. Am.,* vol. 93 no.6, 2434-2444, 2003.

Husen, S., R.B. Smith, and G. P. Waite, Evidence for gas and magmatic sources beneath the Yellowstone volcanic field from seismic tomographic imaging, *J. Volcan. Geotherm. Res.*, 131, 397-410, 2004.

Larson, R.J. and M.L. Marx, An introduction to mathematical statistics and its applications, 536 pp., Prentice-Hall, Englewood Cliffs, N.J., 1981.

Lynch, D., R.B. Smith and H.B. Benz, Three-dimensional tomographic inversion of crust and upper mantle structure of the eastern Basin Range-Rocky Mountain transition from earthquake and regional refraction data, Abstracts from the 9th Annual IRIS Workshop, the IRIS Consortium, Breckenridge, Colorado, 1997.

Lomax, A., J. Virieux, P. Volant, and C. Thierry-Berge, Probabilistic earthquake location in 3D and layered models, in *Advances in Seismic Event Location*, C.H. Thurber and N. Rabinowitz (Editors), Kluwer Academic Publishers, Dordrecht/Boston/London, 101-134, 2000.

Lomax, A., and A. Curtis, Fast, probabilistic earthquake location in 3D models using Oct-Tree Importance sampling, *Geophys. Res. Abstr.*, 3, 2001.

Massin, F., J. Farrell, and R.B. Smith, Repeating earthquakes in the Yellowstone volcanic field: Implications for rupture dynamics, ground deformation, and migration in earthquake swarms, *J. Volcanol. Geotherm. Res.*, 257, 159-173, 2013.

Mavko, G., and Mukerji, T., Seismic pore space compressibility and Gassmann's relation, *Geophysics*, 60, 1743-1749, 1995.

Miller, D. S., and R.B. Smith, P and S velocity structure of the Yellowstone volcanic field from local earthquake and controlled source tomography, *J. Geophys. Res*., 104, 1999.

Michael, A. J., Use of focal mechanisms to determine stress: A control study, *J. Geophys. Res.,* 92(B1), 357–368, 1987.

Nabelek, J., and G. Xia, Moment-tensor analysis using regional data; application to the March 25, 1993, Scotts Mills, Oregon, earthquake, *Geophys. Res. Lett.*, 22 (1), 13-16, 1995.

Nishimura, T., *and* W. Thatcher, Rheology of the lithosphere inferred from postseismic uplift following the 1959 Hebgen Lake earthquake, *J. Geophys. Res.,* 108, *2389, 2003.*

Pelton, J.R., and R.B. Smith, Contemporary vertical surface displacements in Yellowstone National Park, *J. Geophys. Res.*, 87, 2745-2761, 1982.

Peyton, S.L., Seismotectonics of the Yellowstone-Hebgen Lake region from earthquake focal mechanisms and stress field inversions, M.S. thesis, University of Utah, Salt Lake City, Utah, 1991.

Pierce, K.L., and L.A. Morgan, The track of the Yellowstone hotstpot: volcanism, faulting and uplift, in *Regional Geology of Eastern Idaho and Western Wyoming*, edited by P.K. Link, M.A. Kuntz, and L.B. Platt, pp. 1-53, Geological Society of America, Boulder, Colorado, 1992.

Puskas, C.M., R.B. Smith, and C.M. Meertens, GPS-derived models of intraplate deformation of the Yellowstone Hotspot, *EOS Trans.* AGU, 84, 2002.

Puskas, C.M., R.B. Smith, C.M. Meertens and W.L. Chang, Crustal deformation of the Yellowstone Snake River Plain volcano-tectonic system: Campaign and continuous GPS observations, 1987-2004, *J. Geophys. Res.*, 112, 2007.

Reber, J.E., Schmalholz, S.M., and Burg, J.-P., Stress orientation and fracturing during three-dimensional buckling: numerical simulation and application to chocolate-tablet structures in folded turbidites, SW Portugal, *Tectonophysics*, vol. 493, issues 1-2, 2010.

Rivera, L., and Cisternas, A., Stress tensor and fault plane solutions for a population of earthquakes, *Bulletin of Seismological Society of America*, vol. 80 no.3, 600-614, 1990.

Robinson, R.*, and* P. J. McGinty*,* The enigma of the Arthur's Pass, New Zealand, earthquake: 2. The aftershock distribution and its relation to regional and induced stress fields*, J. Geophys. Res.,* 105*(*B7*),* 16139–16150*, 2000.*

Ruppel, E.T., Geology of pre-Tertiary rocks in the northern part of Yellowstone National Park, Wyoming, in *Geology of Yellowstone National Park*, *U.S. Geol. Surv. Prof. Pap.*, P 0729-A, A1-A66, 1972.

Savage, J.C., M. Lisowski, W.H. Prescott, and A.M. Pitt, Deformation from 1973 to 1987 in the epicentral area of the 1959 Hebgen Lake, Montana, earthquake (M_s=7.5), *J. Geophys. Res.*, 98, 2145-2153, 1993.

Schilly, M.M., Smith, R.B., Braile, L.W. and Ansorge, J., 1978 Yellowstone-eastern Snake River Plain seismic profiling experiment: Data and upper crustal structure of the Yellowstone region, *J. Geophys. Res.*, 87, 1982.

Schwartz, S., Tricart, P., Lardeaux, J., Guillot, S., and Vidal, O., Late tectonic and metamorphic evolution of the Piedmont accretionary wedge (Queyras Schistes lustres, western Alps): evidences for tilting during Alpine collision, *Geological Society of America*, v. 121 n. 3-4, p. 502-518, 2009.

Shelly, D.R., D. Hill, F. Massin, J. Farrell, R.B. Smith, and T. Taira, A fluid-driven earthquake swarm on the margin of the Yellowstone caldera, *J. Geophys. Res.,* 118, 1-15, 2013.

Smith, R.B., Braile, L.W., Schilly M, Ansorge, J., Prodehl, C., Baker, M., Healey, M., Mueller, H.S., and Greensfelder, R., The Yellowstone-eastern Snake River Plain seismic profiling experiment: Crustal structure of Yellowstone, *J. Geophys. Res.*, 84, 2583-2, 1982.

Smith, R. B., and W.J. Arabasz, Seismicity of the Intermountain Seismic Belt, in *Neotectonics of North America*, edited by D:B. Slemmons, E.R. Engdahl,

M.D. Zoback, and D.D. Blackwell, *Geological Society of America*, Boulder, Colorado, 1991.

Smith, R.B. and L.W. Braile, The Yellowstone hotspot, *J. Volcanol. Geotherm. Res.*, 61, 121-187, 1994.

Smith, R.B., et al., Geodynamics of the Yellowstone hotspot and mantle plume: Seismic and GPS imaging, kinematics, and mantle flow, *J. Volcanol. Geotherm. Res.*, 188, 26-56, 2009.

Taira, T., R.B. Smith, and W.L. Chang, Seismic evidence for dilatational deformation accompanying the 2004-2008 Yellowstone accelerated uplift episode, *J. Geophys. Res.*, 115, B02301, 2010.

Tarantola, A., and B. Valette, Inverse problems=quest for information, *J. Geophys. Res.*, 50, 159-170, 1982.

Vasco, D.W., C.M. Puskas, R.B. Smith, and C.M. Meertens, Crustal deformation and source models of the Yellowstone volcanic field from geodetic data, *J. Geophys. Res.*, 112, 2007.

Waite, G.P., and R.B. Smith, Seismic evidence for fluid migration accompanying subsidence of the Yellowstone caldera, *J. Geophys. Res.*, 107, 2177, 2002.

Waite, G.P., and R.B. Smith, Seismotectonics and stress field of the Yellowstone volcanic plateau from earthquake first-motions and other indicators, *J. Geophys. Res.*, 109, 2004.

Werner, C., Hurwitz, S., Evans, W.C., Lowenstern, J.B., Bergfeld, D., Heasler, H., Jaworowski, C., Hunt, A., Volatile emissions and gas geochemistry of Hot Spring Basin, Yellowstone National Park, USA, *J. Geophys. Res*., 178, 751-762, 2008.

Wicks Jr., C., W.Thatcher, and D. Dzurisin, Migration of fluids beneath Yellowstone caldera inferred from Satellite radar interferometry, *Science*, 282, 458-462, 1998.

Wicks, C., Thatcher, W., and Dzurisin, D., Uplift, thermal unrest and magma intrusion at Yellowstone Caldera, *Nature*, 440, 72-75, 2006.

Zoback, M.L., First and second-order patterns of stress in the lithosphere: The World Stress Map Project, *J. Geophys. Res.*, 97(B8), 11,703-11,728, 1992.

ACKNOWLEDGMENTS

Foremost, I would like to express my sincere gratitude to my advisor dr. Gregory P. Waite for his patience, enthusiasm, motivation and immense knowledge. He helped me in all the research and writing of this thesis, both in the times that I spent at the Michigan Technological University and in Italy, when keeping in touch by email was the only chance to continue the research activity together. I will always admire his unique ability to generate enthusiasm among his students.

Besides my advisor, I would like to express my gratitude to my co-advisor, prof. Alessandro Tibaldi for his suggestions, comments, and stimulating discussions. He provided me with directions and technical support everytime I needed.

A special thanks also goes to Dr Jamie Farrell and Dr Frederick Massin, from University of Utah, for giving me the possibility to use their database and knowledge to complete my research. Without their help, this thesis would not have been possible.

I thank Dr Wu-Lung Chang, Dr Robert Christiansen, Dr Robert B. Smith, Dr. Christine Puskas and Dr Chuck Wicks for permitting me to use some of the results from their research works in order to improve my thesis.

I am grateful to my university and to the exchange program INVOGE, because it gave me the opportunity to live the most rewarding and rich

experience of my life. Studying in a different environment improved my self-trusting and my independence.

I thank my family, especially my parents, for the support they provided me through my entire life and their encouragement. They always gave me the strength and wisdom necessary to face the difficulties.

Last but not least, I thank my friends for all the good talks and all the fun we have had in the last years; I thank my boyfriend, for being always there cheering me up and standing by me through the good times and bad. Also I thank my international friends, the wonderful people I had the chance to meet during the nine months I spent abroad in the opposite side of the world.